MICROCANTILEVERS: CALIBRATION OF THEIR SPRING CONSTANTS AND USE AS ULTRASENSITIVE PROBES OF ADSORBED MASS

John D. Parkin

A Thesis Submitted for the Degree of PhD
at the
University of St Andrews

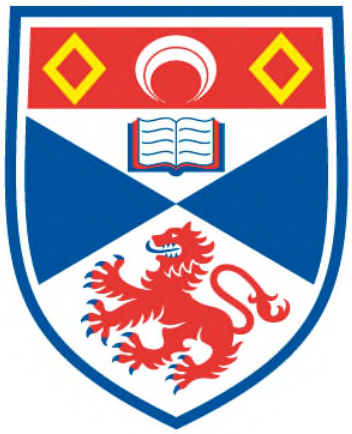

2013

Microcantilevers: Calibration of their spring constants and use as ultrasensitive probes of adsorbed mass

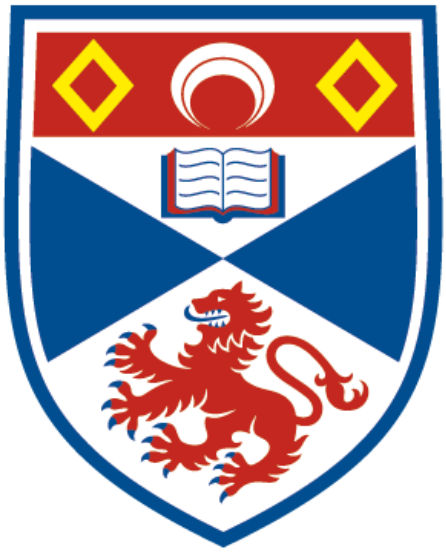

University of
St Andrews

This thesis is submitted in partial fulfilment for the degree of

PhD at the University of St Andrews

Date of Submission: 1/3/2013

Author:

John D. Parkin

Supervisor:

Dr. Georg Hähner

Declarations

Candidate's declarations:

I, John Parkin, hereby certify that this thesis, which is approximately 44,000 words in length, has been written by me, that it is the record of work carried out by me and that it has not been submitted in any previous application for a higher degree.

I was admitted as a research student in September 2009 and as a candidate for the degree of Doctor of Philosophy in September 2010; the higher study for which this is a record was carried out in the University of St Andrews between 2009 and 2013.

Date ..... Signature of candidate .....

Supervisor's declaration:

I hereby certify that the candidate has fulfilled the conditions of the Resolution and Regulations appropriate for the degree of Doctor of Philosophy in the University of St Andrews and that the candidate is qualified to submit this thesis in application for that degree.

Date ..... Signature of supervisor .....

Permission for electronic publication:

In submitting this thesis to the University of St Andrews I understand that I am giving permission for it to be made available for use in accordance with the regulations of the University Library for the time being in force, subject to any copyright vested in the work not being affected thereby. I also understand that the title and the abstract will be published, and that a copy of the work may be made and supplied to any bona fide library or research worker, that my thesis will be electronically accessible for personal or research use unless exempt by award of an embargo as requested below, and that the library has the right to migrate my thesis into new electronic forms as required to ensure continued access to the thesis. I have obtained any third-party copyright permissions that may be required in order to allow such access and migration, or have requested the appropriate embargo below.

The following is an agreed request by candidate and supervisor regarding the electronic publication of this thesis:

Embargo on both all of printed copy and electronic copy for the same fixed period of two years on the following grounds:

1. publication would be commercially damaging to the researcher, or to the supervisor, or the University;

2. publication would preclude future publication;

Date ..... Signature of candidate .....

Date ..... Signature of supervisor .....

Abstract

The dynamic properties of several rectangular and V-shaped microcantilevers were investigated. Particular attention was paid to the higher flexural eigenmodes of oscillation. The potential of the higher flexural modes was demonstrated through the use of cantilevers as standalone sensors for adsorbed mass. The mass adsorbed on the surface of a cantilever was in the form of a homogeneous water layer measured as a function of relative humidity. The minimum detectable water layer thicknesses were 13.7 Å, 3.2 Å, 1.1 Å, and 0.7 Å for the first four modes of a rectangular cantilever, clearly demonstrating enhanced accuracy for the higher eigenmodes of oscillation. These thicknesses correspond to minimum detectable masses of 33.5 pg, 7.8 pg, 2.7 pg and 1.7 pg for the first four modes.

For quantitative applications the spring constants of each cantilever must be determined. Many methods exist but only a small number can calibrate the higher flexural eigenmodes. A method was developed to simultaneously calibrate all flexural modes of microcantilever sensors. The method was demonstrated for the first four eigenmodes of several rectangular and V-shaped cantilevers with nominal fundamental spring constants in the range of 0.03 to 1.75 N/m. The spring constants were determined with accuracies of 5-10 %. Spring constants of the fundamental mode were generally in agreement with those determined using the Sader method. The method is compatible with existing AFM systems. It relies on a flow of gas from a microchannel and as such poses no risk of damage to the cantilever beam, its tip, or any coating.

A related method was developed for the torsional modes of oscillation.

Preliminary results are shown for the fundamental mode of a rectangular cantilever. The method can be easily extended to the higher torsional modes, V-shaped cantilevers, and potentially, the flapping modes of the legs of V-shaped microcantilevers.

Acknowledgements

The work contained in any thesis would not be possible without the support of the students supervisor. In this case I have been tremendously fortunate to land on my feet and work with a supervisor, Dr Georg Hähner, who has fulfilled the role admirably. I would also like to thank George Anthony for his patience in interpreting and manufacture of the various small items of equipment which were required during this study. Dr Herbert Fruchtl is also recognised for running some of the more computationally expensive simulations on his machine and on the computational cluster here in St Andrews.

I have been fortunate enough to meet various individuals in St Andrews who deserve credit for their companionship and humor, particularly members of the real ale society. Furthermore my long suffering house mate, and fellow PhD student, David Brown deserves recognition for tolerating me for many years. Genes and upbringing are also important so the author would like to thank his parents for that and their support over the last quarter of a decade.

Funding for this project was supplied by the University of St Andrews, which the author gratefully acknowledges.

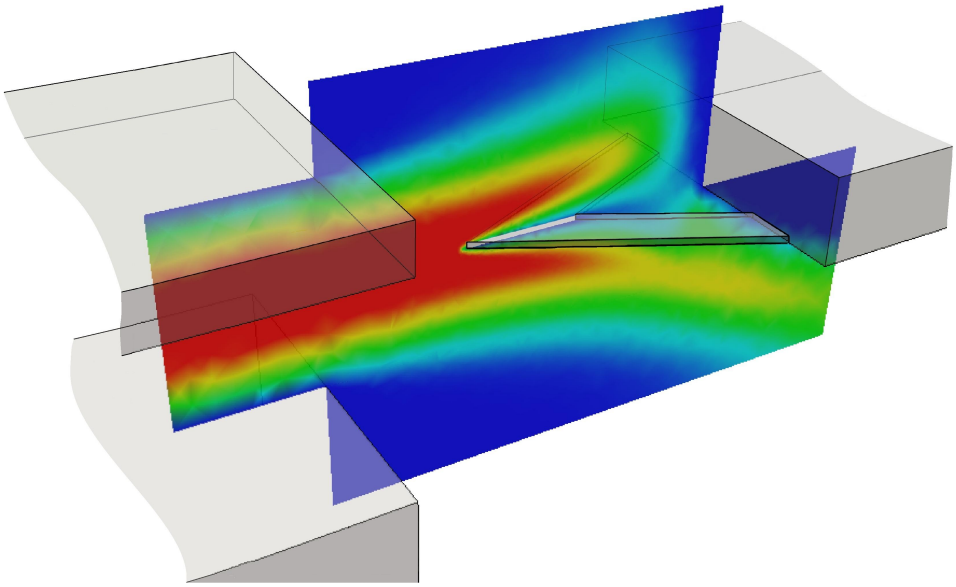

Contents

List of Figures

List of Tables

List of Abbreviations and Notation

Symbol	Explanation
AFM	Atomic force microscopy
CFD	Computational fluid dynamics
FEA	Finite element analysis
FFM	Friction force microscopy
MEMS	Microelectromechanical systems
PFF	Parallel fluid flow
SAM	Self-assembled monolayer

Table 0.1: *Abbreviations used throughout the document are outlined here for the user's reference.*

Symbol	Explanation
δ_{nm}	Dirac delta
$\phi(x)$	Torsional angle of cantilever deflection
μ	Viscosity of nitrogen gas
ρ	Density of nitrogen gas
ρ_c	Density of the cantilever
ρ_w	Density of water
ν	Kinematic viscosity of nitrogen ($=\mu/\rho$)
ω_n	Angular resonance frequency of mode n
ω_{n0}	Initial angular resonance frequency of mode n
$\Delta(\omega_n^2)$	Angular resonance frequency shift ($=\omega_n^2 - \omega_{n0}^2$)
$\Xi(x)$	Profile of the static deflection along the cantilever
$\psi(x)$	Distribution of positions at which the spring constant should be calculated
$\zeta_x(x)$	Distributed force per unit length in the x-direction along the cantilever

Table 0.2: *Greek symbols used throughout the document are outlined here for the user's reference.*

Symbol	Explanation
d	Distance of free end of the cantilever from microchannel exit
E	Young's modulus of the cantilever
f_n	Resonance frequency of mode n
f_{n0}	Initial resonance frequency of mode n
$\Delta(f_n^2)$	Resonance frequency shift ($=f_n^2 - f_{n0}^2$)
F_{end}	Fluidic force on the free end of the cantilever
G	Shear modulus of the cantilever
h	Microchannel height
h'	Altitude of cantilever in flexural calibration scheme, for h=h' the cantilever is level with the top of the channel
H	Tip height
I	Area moment of inertia of the cantilever, for rectangular $I = wt^3/12$
I_p	Polar moment of inertia of the cantilever, for rectangular $I_p = (wt^3 + w^3t)/12$
K	Geometrical function of cantilever cross section, for rectangular $K = wt^3/3$
k_n	Spring constant of mode n
k_s	Static spring constant for cantilever deflection
l	Cantilever length
L	Microchannel length
m_c	Mass of the cantilever
m_w	Mass of an adsorbed water layer
M_n	Internal bending moment relating to mode n
ΔM_n	Additional bending moment of mode n
n	Mode number, torsional mode if followed by a 't'
Q	Quality factor (Q-factor) of an oscillator
Re	Reynolds number
t	Cantilever thickness
u_n	Mode shape of the n^{th} eigenmode
w	Cantilever width, for V-shaped cantilevers this is defined as being parallel to the end of the chip
x	Direction of the cantilever long axis
X	Fractional position along cantilever length, X=0 corresponds to the fixed end, X=1 the free end
y	Direction perpendicular to cantilever plan view area
z	Direction across the cantilever width
z_n	Eigenvalue of the n^{th} eigenmode

Table 0.3: *Latin symbols used throughout the document are outlined here for the user's reference.*

1 Introduction

Due to their small dimensions and therefore also mass and low rigidity, microcantilevers show great sensitivity to very small forces. The forces in question might be due to an interaction between a sharp tip attached to the cantilever and a surface in atomic force microscopy (AFM), or they might be related to the adsorption of molecules onto the surface of the cantilever. Such adsorption processes could affect the properties of the cantilever by effects relating to a change of the effective mass of the cantilever or a change of the effective spring constant due to stresses and strains induced upon the surfaces.

The number of publications including the keyword 'microcantilever' increased quickly through the early years of the new millennium, before reaching a plateau during the last five years, as depicted in figure 1.1. Nonetheless, the general field of microcantilevers is still an active area of

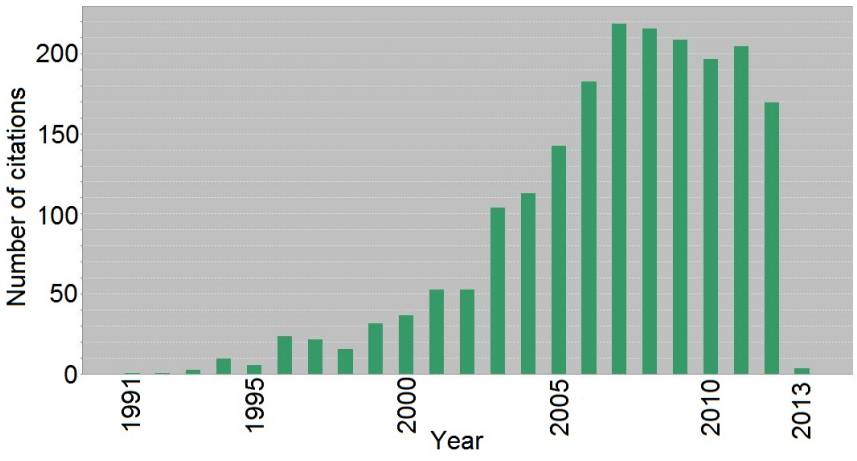

Figure 1.1: *The number of citations in each year for the keyword 'microcantilever'. Data from the ISI Web Of Knowledge collected on 27/12/12.*

interest. Furthermore, the number of articles using the term 'AFM' now

stands at over 82,000.*

1.1 Microcantilevers in Atomic Force Microscopy

Atomic force microscopy (AFM) is the application in which microcantilevers are most often applied. AFM is used to obtain topographic images of surfaces.[2] The best AFM images of very clean surfaces attain atomic resolution[3,4] and can compete with scanning tunneling microscopy in this respect, without the requirement of a conducting sample.[5] This point is an important one and has led to the widespread use of AFM in biological applications. Indeed, AFM has been used in all of the sciences: physics, biology, chemistry, medicine and engineering. It has even been used in the analysis of collagen (from skin) from the 5300 year old Tyrolean Iceman where AFM was used to determine Young's modulus of fibrils. The Young modulus was found to be similar to modern samples indicating good preservation.[6]

The AFM was invented at IBM's research laboratories by Binnig, Quate, and Gerber in 1986.[7] The citations of this article, see figure 1.2, show the uptake of the method as commercial AFM systems became available to research laboratories around the world. The main components of an AFM are sketched in figure 1.3. The microcantilever is fixed at one end where it connects to a support chip which is held by the AFM system. The other end of the cantilever beam has a sharp tip attached to it. The tip is brought close to a surface of interest such that the forces between tip and surface are sufficient to bend, or affect the resonance frequencies of, the cantilever. The movement of the cantilever can be detected by a

*According to the ISI Web Of Knowledge, 27/12/12

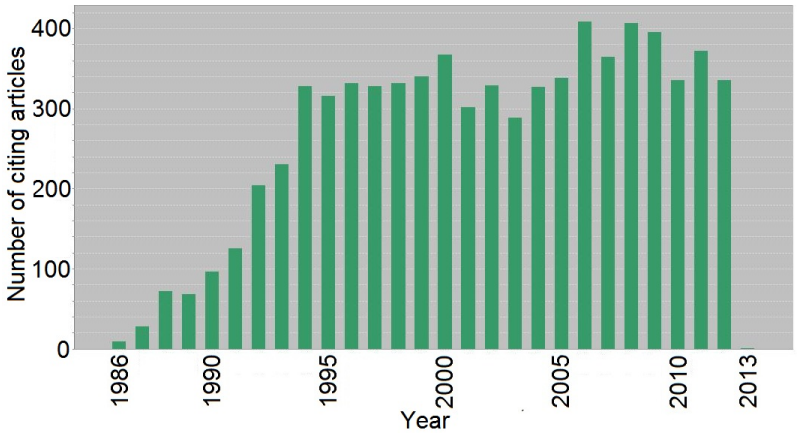

Figure 1.2: *The number of citations in each year of ref.[7] since its publication in 1986. Data from the ISI Web Of Knowledge obtained on 27/12/12.*

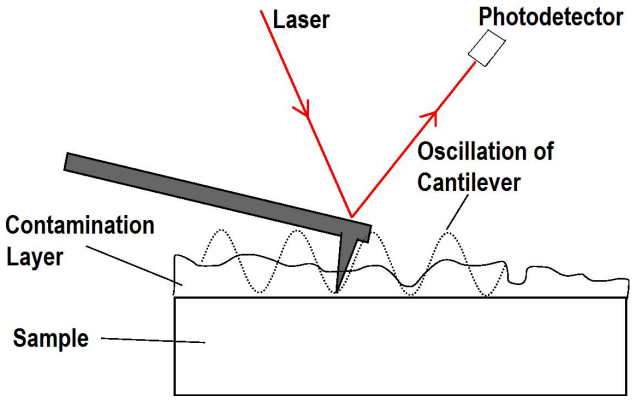

Figure 1.3: *Side view image of the main components of an AFM. The tip movement is illustrated by the sinusoidal curve to represent a tapping mode.*

laser reflected off the cantilever (as in the figure), by use of piezoelectric cantilevers, or by interferometry. If the tip/cantilever is scanned over the surface and the cantilever response monitored then a topographic image of the surface can be obtained. The image is essentially a contour of constant tip-sample force, in a similar manner to scanning tunneling microscopy which can plot a constant electrical potential (or current). However, the AFM image is usually much more closely related to the surface topography whereas heights in an STM image depend critically

upon bias voltages and atom types.

There are several different operational schemes in AFM; static, tapping, and dynamic. In static measurements the feedback system of the instrument keeps a set force between tip and surface by monitoring the cantilevers static bending and moving the cantilever up or down to maintain a constant set force. Essentially the tip is dragged across the surface and the image is a contour of constant force. However, if the set force is too large then the tip is likely to be damaged and become blunt, decreasing resolution as scanning proceeds. Parts of the sample surface may also be damaged or even destroyed if the applied force is too large.

In tapping mode the cantilever is driven to oscillate such that the tip travels up and down, contacting the surface then retracting.[3] The movement of the tip in this mode of operation is indicated by the sinusoidal curve in figure 1.3.

In the frequency modulated mode of operation the cantilever resonance frequency is monitored as the tip is scanned across the surface a small distance above it. The tip samples a force gradient which can modify the resonance frequency slightly, which can be used to reconstruct the surface topography.[3] In this mode there is often no hard contact between tip and surface and damage is much less likely. It is often with this method that the highest resolution images are achieved.[8]

One disadvantage of AFM is that it can only scan surfaces, which must be reasonably flat, and therefore bulk properties must be inferred if they are of interest. Therefore AFM is often combined with other instrumentation, for example with TEM to obtain 3-D information.[9]

AFM of biological samples and soft matter is one of the more exten-

sive areas of its application.[10–12] It has been used as a tool to observe crystallisation for some time[13] and with recent developments in high speed AFM the actual crystallisation process of polymers has been monitored.[11, 14] The ability to "watch" processes in AFM as they are happening is an exciting area of development.[11,14–17] High speed methods sacrifice some resolution, and increase the likelihood of damage to tip or sample.

Other variations include collection of images in a liquid, for example biological cells in vivo.[18] However, scanning in liquid introduces additional damping that in dynamic AFM reduces or even completely masks the resonance peak. Stiffer cantilevers often have to be used. An alternative is to use an oscillation mode other than the fundamental flexural resonance. A torsional eigenmode could be used.[19] Its lower amplitude of oscillation means that a reduced amount of the surrounding fluid has to be moved by the cantilever, resulting in less damping and therefore less of a reduction of the amplitude of the resonance peak.

The cantilever itself has had relatively little development since the first use of AFM over 25 years ago. A recent development is the use of hammerhead or T-shaped cantilevers. The tip is displaced from the centreline of the cantilever's long axis to one side of the 'T'. The cantilever is designed to have a low flexural spring constant which helps to prevent damage while the fundamental torsional mode is monitored to build the image. A combination of fundamental flexural and torsional modes must be analysed and results in a 'torsional tapping' motion of the tip.[20]

An implementation which can be realised to extract additional information from AFM imaging and increase sensitivity through higher

Q-factors is the use of higher eigenmodes than the fundamental.[8,21,22] Ref.[22] describes a Si(111)-(7×7) surface scanned in non-contact mode using both the first and second eigenmodes. The image collected using the second eigenmode had an enhanced signal-to-noise ratio over the fundamental mode. Images of Si(111)-(7×7) surfaces have also been made using the second[23] and third[24] flexural modes. The advantage of using the higher modes here is the small oscillation amplitude and high sensitivity enabling detection of force gradients relatively far away from the surface.

One can imagine an AFM instrument operated dynamically where one mode (e.g. the first flexural) is used to determine the topography of a surface while another mode (e.g. the second flexural) is used to produce a plot of the local Young's modulus over the surface, similar to that described in ref.[25]. Such a measurement could go some way to counteracting one of the main problems with AFM, that in its basic form it has no chemical contrast. It is also possible to distinguish between different surface chemistries in AFM using functionalised tips, phase imaging, or friction force microscopy, amongst others.[26]

1.2 Microcantilevers in the Measurement of Viscoelastic Properties of Surfaces

Essentially a subset of AFM imaging is the use of the instrumentation to measure the viscoelasticity of a single point on a sample. A measurement akin to a force curve is conducted where the probe (tip) is pressed into the surface at a known force, the cantilever deflection is measured and the

compression of the sample surface can be inferred. The effective radius of the probe must be known and so a colloidal probe is often attached to the cantilever in place of the tip.[10] The first colloidal probes were made of silica[27] and these are the most popular. They might also be made of glass.[28] The colloidal probe itself is ideally spherical with a diameter of 1 to 30 μm and low surface roughness: a rms roughness of a nanometre or less over an area of 1 μm^2. The probe provides a smoother, more predictable contact area than a tip. The larger contact area also reduces the possibility of damage to soft samples such as cells.[10]

Biological cells are the main area of application for the measurement of viscoelastic properties.[29] It has been reported that elasticity measurements of cells can distinguish between those which are cancerous and those which are healthy. Cancerous cells have been observed to be around 70% softer than those which are non cancerous.[18, 30]

The viscoelastic properties of human platelets have been measured using AFM, a map of the elastic modulus with horizontal resolution of 100 nm was achievable as long ago as 1996.[31] At the same time as collecting the modulus map, a topographical resolution of less than 20 nm was obtained. A study of the viscoelasticity of the lamellipodium, the edge of a cell, was completed in ref.[32]. The viscoelastic constants: elastic storage modulus, viscous loss modulus, and the Poisson ratio were determined.[32]

Since AFM and AFM based measurements must be executed on relatively flat samples, any biological cell has to be immobilised on a substrate. Care has to be taken to ensure that the immobilisation does not significantly affect the properties of interest. This is a complicating fac-

tor, and different models must be used for areas of cells which are well adhered and poorly adhered.[32]

1.3 Microcantilevers as Sensors

Microcantilevers can be used as stand-alone sensors, usually by monitoring effects due to the adsorption of molecules onto their surface. The field emerged in the mid 1990s[33] and now applications include explosives detection,[34] drug discovery[35] and material characterisation.[36, 37]

There are two possible effects of adsorption which may lead to a measurable change; an increase of the effective mass of the cantilever or an induced surface stress which can be described as a change in the effective spring constant of the cantilever. Static deflection of the cantilever or monitoring of the resonance frequency can be used as the method of detection. The dynamic detection route is now more often used as it is less sensitive to drift effects whilst offering greater sensitivity.

Coatings may be introduced to provide some chemical specificity while arrays of multiple cantilevers can be manufactured to provide small, handheld sensors which can detect a multiplicity of different vapours. One example of such an 'artificial nose' is described in ref.[38] with eight differently coated rectangular cantilevers. The static deflection of the cantilever was monitored. The coatings were all polymer based and through monitoring the response of all cantilevers simultaneously various organic vapours were identifiable, including a range of alcohols, toluene, hexane, acetone, dichloromethane. The use of microcantilevers as sensors is a highly promising one if specificity can be achieved alongside the small dimensions inherent in such systems. In conjunction with sili-

con microchip derived manufacturing processes such commercial devices should be generally affordable too.

Dynamic microcantilever sensors, where the resonance frequency of the cantilever is monitored, offers improvements in sensitivity over static deflection based measurements.[39] Fitting of the resonance frequency curve of the fundamental flexural resonance has been used to determine the viscosity and density of fluids.[40–42] The cantilever is placed in the fluid of interest and the frequency response is altered by the physical properties of the fluid. Volumes on the order of microlitres are required. The bending and/or frequency response of microcantilevers to a flow of fluid could be used to determine the velocity and relative pressure of a fluid.[43]

Use of the higher modes of oscillation has been suggested as one alternative to using smaller cantilevers as a pathway to increased sensitivity.[39] Smaller cantilevers have lower masses and tend to have higher spring constants meaning that any adsorption event is a greater proportional addition of mass and the Q-factor of the oscillation is enhanced over a larger cantilever. Use of the higher flexural modes has a similar effect. The higher modes can have lower effective oscillating masses[44] leading to greater sensitivity.

Ref.[45] found a similar sensitivity to added mass when using the higher modes of a soft cantilever to the sensitivity obtained by using smaller cantilevers with similar spring constants to those of the higher modes. The added mass was introduced by coating the cantilevers with polyacrylamide through dipping in a solution. The study found that the Q-factors of the higher modes were reduced by the additional mass to a

greater extent than those of the short cantilevers and therefore concluded that shorter cantilevers should be used in environments, such as liquids, where high Q-factors are required. The coating process would probably have been difficult to control and ensuring a homogeneous coating of the cantilever non-trivial. Unfortunately, ref.[45] does not describe this process in more detail, nor if the homogeneity of the coating was checked.

Collating various applications of microcantilevers onto a single, small, reliable and cheap device is the goal of lab-on-a-chip technology.[34,38,46]

1.4 The Need for Calibration of Microcantilevers

Microcantilevers have many applications, more numerous than their initial application as a component of the AFM. However, for quantitative analysis in most of these cases their stiffness, or spring constant, is required. For measurements involving static deflection the spring constant describes the cantilevers resistance to bending, i.e. Hookes Law.

Microcantilevers are widely available from a range of companies, but due to uncertainties in the manufacturing process the actual fundamental spring constant is expected to vary from the manufacturers nominal spring constant by as much as -60% to +250%. For example, a 350 μm long, 35 μm wide, 1 μm thick silicon rectangular cantilever from Mikromasch (CSC12,[47] known as R-E in this document) has a nominal spring constant of 0.03 N/m but minimum and maximum of 0.01 N/m and 0.08 N/m respectively. The major source of error is in the thickness where a small deviation can have a large effect because the spring constant of a cantilever scales with the third power of thickness.

In any quantitative analysis it is important to use the spring constant

of the particular cantilever in question. Each cantilever must be calibrated and therefore swift, easy, reliable and accurate calibration schemes which do not pose risk of damage to cantilever (or its tip) are required. A short review of existing calibration methods for the fundamental flexural mode is given in section 4.2 (see also refs.[48–50]) and the corresponding section for the torsional and lateral modes in section 5.2 (see also[51]). Less than a handful of the existing calibration methods have been extended to higher flexural modes. Most of the methods to calibrate the torsional (or lateral) spring constant are either inaccurate or place the cantilever or tip quality in jeopardy. Any method that can be reasonably accurate and eliminate potential for tip or cantilever damage in the calibration is expected to be of interest.

1.5 Outline of the Remainder of the Document

The next chapter provides a grounding in the mathematics and theoretical background required to understand the remainder of the document. It is envisaged that the reader who is already familiar with microcantilevers and the description of their various modes of oscillation may skip the majority of the section, though particular attention should be paid to the normalisation of the eigenmodes in section 2.5. The process of eigenmode normalisation is essentially the one which the methods developed for spring constant calibration, in chapters 4 (flexural) and 5 (torsional), aim to do for real cantilevers. Preceding these chapters is one (chapter 3) which highlights the use of the higher modes of microcantilevers as sensors. The experimental execution is one of a humidity sensor in the detection of adsorbed water layers of thicknesses on the

scale of Ångströms.

2 Theoretical Overview of Microcantilevers

At this point a short review of microcantilevers, their oscillation properties, and their theoretical description is given as a grounding to the work contained within this document.

2.1 The Microcantilever

A cantilever is a long thin beam which is supported or fixed at one of its ends. All the cantilever beams described in this document are fixed at one end, as depicted in figure 2.1. At the fixed end of the cantilever its displacement and the slope of the deflection curve must be zero. A microcantilever is a cantilever whose dimensions are all measured in micrometres, the smallest dimension being its thickness of around one micrometre and the largest being its length up to a few hundred micrometres. Microcantilevers are generally manufactured using silicon, silicon nitride or a variety of polymers.

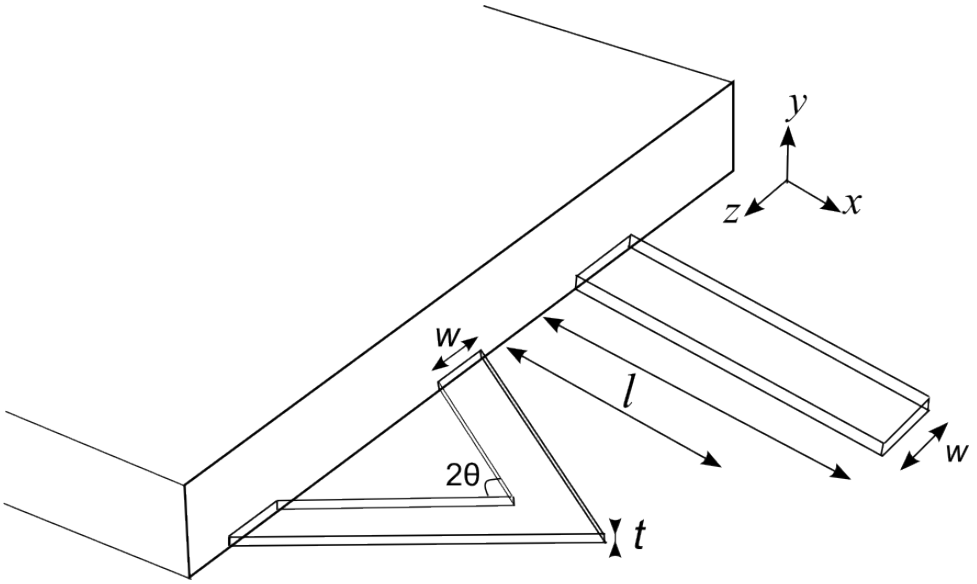

Figure 2.1: *Schematic of a rectangular and a V-shaped cantilever attached to a chip.*

2.2 Cantilever Oscillations

All structures oscillate at a characteristic frequency due to the energy they possess by being at a finite temperature, that is they are driven by thermal noise. The natural frequencies, ω_n, of a structure are defined by its material properties, shape, and its boundary conditions. A cantilever may be described as a simple harmonic oscillator, and hence

$$\omega_n^2 = \frac{k_n}{m_n} \tag{2.1}$$

holds, where k_n is its spring constant and m_n is its effective oscillating mass.[44] The cantilever may oscillate in a variety of different flexural modes described by the mode number, n. Each mode has its own spring constant. The reciprocal sum of the dynamic spring constants equals the reciprocal of the spring constant for static deflection, k_s,[44]

$$\frac{1}{k_s} = \sum_n \frac{1}{k_n}, \tag{2.2}$$

for a point mass model where k_s is to be obtained at the same position (e.g. at the tip) as the force of interest is applied. The resonance frequency of a cantilever is easy to obtain experimentally and any change, $\Delta(\omega_n^2) = \omega_n^2 - \omega_{n0}^2$ where ω_{n0} is the initial resonance frequency, can be expressed via a change of mass, Δm_n, or a change of spring constant, Δk_n,

$$\frac{\Delta(\omega_n^2)}{\omega_n^2} = \frac{\Delta k_n}{k_n} - \frac{\Delta m_n}{m_n}. \tag{2.3}$$

A change in mass could be due to the adsorption or desorption of molecules from the surface, as in chapter 3, while an effective change of the spring constant could be due to an external force (chapters 4 and 5), force gradient, or surface stress (section 3.5). If a cantilever is driven only by

thermal noise then the equipartition theorem,

$$\frac{1}{2}k_BT = \frac{1}{2}k_n \left\langle A_n^2 \right\rangle, \tag{2.4}$$

holds where k_B is the Boltzmann constant, T is the temperature and A_n is the amplitude of oscillation of the n^{th} mode. Equation (2.4) provides a useful way to calculate the spring constant from the oscillation amplitude of a mode or vice versa.

Oscillations may be assigned an associated quality factor which is proportional to the ratio of the energy stored in an oscillator to the energy dissipated per cycle. It can be expressed by relating the resonant frequency and damping, β, as[52]

$$Q = \frac{\omega}{2\beta}. \tag{2.5}$$

Essentially, it is the frequency at the centre of the peak divided by the full width at half maximum. Larger Q-factors represent sharper, taller resonant peaks, for Q=0 there is no peak at all. The effect of changing Q is demonstrated in figure 2.2.

2.3 Eigenmodes of Rectangular Cantilevers

A cantilever may oscillate in a number of different modes; flexural, torsional, lateral and extensional. Each of the cantilever modes can be described by an eigenmode, or modeshape, $u_n(x)$. The flexural (and torsional) deflection of cantilever plates normal to their plan view area depends in general on both coordinates spanning the plane of the area. However, under the operating conditions in AFM and other techniques employing microcantilevers as sensors the true deflection is often well ap-

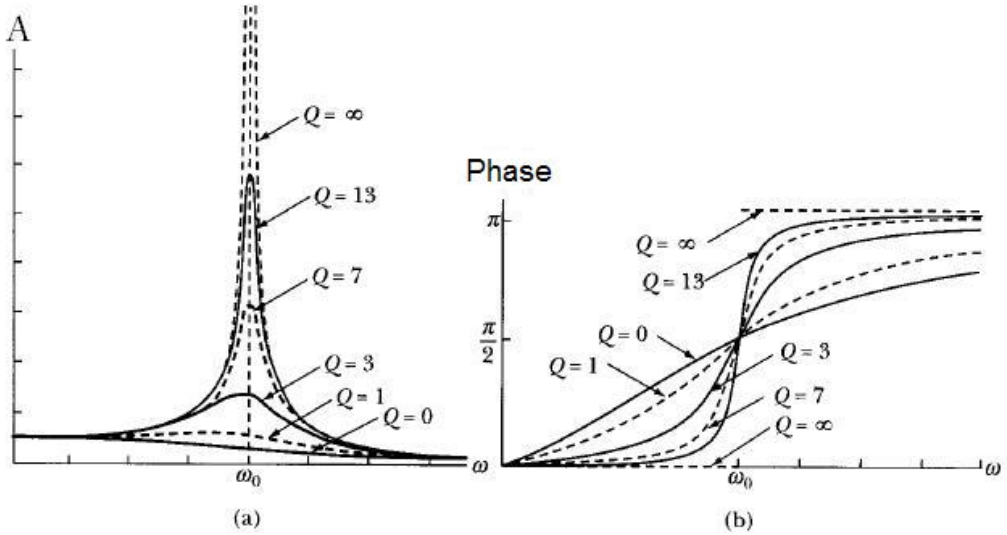

Figure 2.2: *The effect of changing the Q-factor on (a) the amplitude and (b) the phase around the resonance peak. Figure adapted with permission from ref.[52].*

proximated by a function that only depends on the coordinate, x, along the cantilever length.[53, 54]

2.3.1 Flexural Eigenmodes

The flexural eigenmodes of a cantilever describe its oscillation perpendicular to its plan view area, in the y-direction of figure 2.1. The fundamental flexural mode tends to have the lowest spring constant and resonance frequency of all modes. The flexural eigenmodes and eigenvalues are readily available for rectangular cantilevers[1] and can be derived as follows.

With reference to figure 2.3 the differential equation of the flexural deflection curve of a free prismatical beam can be expressed as[1]

$$EI\frac{d^2y}{dx^2} = -M \tag{2.6}$$

where M is bending moment at any cross section, E is Young's modulus and I is the moment of inertia. Twice differentiating equation (2.6) with

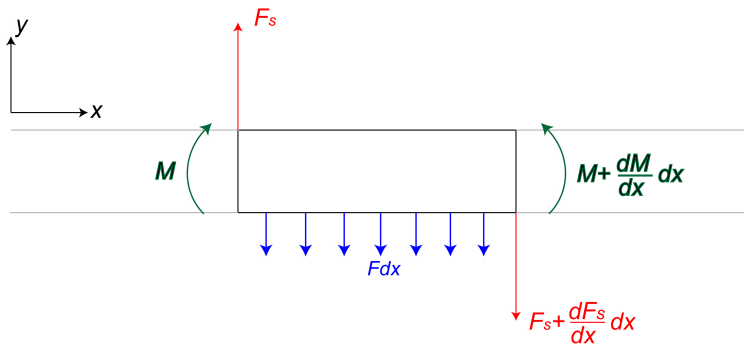

Figure 2.3: *Schematic of the loads (F), shearing forces (F_s) and moments (M) associated with a small section, dx, of a vibrating beam.*

respect to x yields

$$EI\frac{d^4y}{dx^4} = F \tag{2.7}$$

where F is a continuous load and EI is assumed to be constant along the length (x-direction) for a rectangular beam. Assuming that the only force acting on the beam is due to its inertia implies that the load, F may be expressed as $-\frac{\rho_c wt}{g}\frac{\partial^2 y}{\partial t^2}$ where g is the acceleration due to gravity, ρ_c is the density of the cantilever, w is the cantilever width, and t is the cantilever thickness. Equation (2.7) then becomes

$$EI\frac{\partial^4 y}{\partial x^4} = -\frac{\rho_c wt}{g}\frac{\partial^2 y}{\partial t^2}. \tag{2.8}$$

This equation describes the vibrations of a prismatical beam. If the beam oscillates in one of its eigenmodes then each point of the beam vibrates harmonically with time and equation (2.8) can be solved by a solution of the form $y(x,t) = X(x)T(t) = u_n(x)\exp^{-i\omega_n t}$. Substitution of the form of $y(x,t)$ into equation (2.8) leaves

$$\frac{1}{u_n(x)}\frac{d^4u_n(x)}{dx^4} = \frac{\rho_c wt}{EIg}\omega_n^2, \tag{2.9}$$

the solution to which is a combination of trigonometric functions, $u_n(x) = A\sin(z_n x/l) + B\cos(z_n x/l) + C\sinh(z_n x/l) + D\cosh(z_n x/l)$.[1] z_n are the eigen-

values of each mode of oscillation, and along with the constants $A - D$, are determined from boundary conditions imposed upon the beam's motion. For a cantilevered beam the fixed end (at $x = 0$) should have zero displacement ($u_n(0) = 0$) and zero slope to the deflection ($du_n(0)/dx = 0$). The conditions on the free end ($x = l$) are that the bending moment and shear force vanish, $d^2u_n(l)/dx^2 = 0$ and $d^3u_n(l)/dx^3 = 0$ respectively. The conditions at the fixed end mean that $A = C = 0$ and the conditions at the free end give the eigenvalue equation

$$\cos(z_n)\cosh(z_n) = -1 \tag{2.10}$$

which may be solved graphically to give the flexural eigenvalues of a rectangular cantilever beam as displayed in table 2.1.

n	z_n
1	1.875
2	4.694
3	7.855
4	10.996
5	14.137
6	17.279

Table 2.1: *Eigenvalues relating to the first six flexural eigenmodes of cantilevered beams. Values taken from[1].*

Two different eigenmodes must be orthogonal[†], mathematically expressed as

$$\int_0^l u_n(x)u_m(x)dx = \delta_{nm} \tag{2.11}$$

[†]see p326-7 of [1] for the derivation of the orthogonality condition

where δ_{nm} is the Dirac delta function, $\delta_{nm} = 0$ if $n \neq m$ and $\delta_{nm} = 1$ if $n = m$. The first three flexural modeshapes of a rectangular cantilever are shown in figure 2.4.

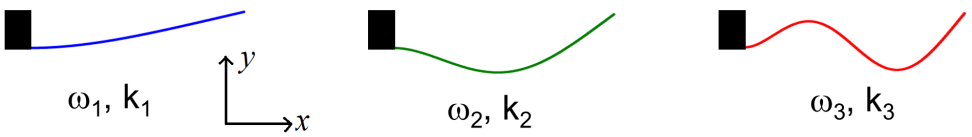

Figure 2.4: *Modeshapes of the first three flexural modes of a rectangular cantilever. The shape represents a flexural deflection of arbitrary unit.*

The frequency of each mode may be calculated using

$$\omega_n = \frac{z_n^2}{l^2}\sqrt{\frac{EI}{\mu}}, \tag{2.12}$$

where the moment of inertia is $I = wt^3/12$ and $\mu = \rho_c wt$ is the mass per unit length of the beam.

For most microcantilever beams the fundamental flexural mode has the smallest spring constant and hence the amplitude of the mode is the largest for a given energy. For a rectangular cantilever of spring constant 0.03 N/m (such as cantilever R-E used throughout this work), the amplitude of oscillation of the first flexural mode can be calculated using equation (2.4) to be around 4 Å at T=300 K. The amplitudes of the higher modes may also be calculated and are observed to decrease with mode number. The amplitude scales with mode number as $z_n^2/z_{n'}^2$, with $n' > n$, so that in the example above the amplitude of the fourth flexural mode is only around 0.1 Å at room temperature.

The eigenmodes may also be visualised by finite element analysis (FEA) simulations, executed in this work by utilising the multiphysics software Elmer.[55] The meshes used were created by Gmsh.[56] The dis-

placements of the first few modes are displayed in figure 2.5, where the cantilever is shown in the plan elevation and the fixed end of the cantilever is to the left side of each subfigure. The colour scale represents a flexural deflection of arbitrary unit and replicates the theoretical shape of figure 2.4. Recently, ref.[57] reported that experimental modeshapes could be accurately reproduced by FEA simulations.

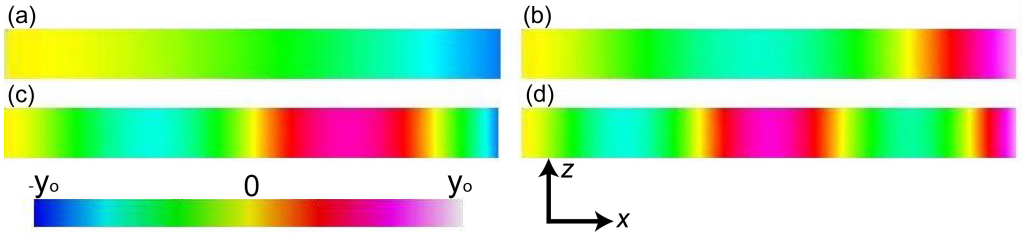

Figure 2.5: *Figure showing the displacements (out of the page, given by the colour scale) representing the modeshapes of the first four flexural modes of a rectangular cantilever as determined by a FEA simulation. (a): fundamental (first) flexural mode, (b): second flexural mode, (c): third flexural mode, (d): fourth flexural mode.*

2.3.2 Torsional Eigenmodes

A cantilever may also exhibit torsional oscillations about its long axis. Again modeshapes, $u_{nt}(x)$, describing the angular displacement along the cantilever can be derived for rectangular cantilevers and are represented in figure 2.6. The torsional eigenmode shapes can be derived as follows.

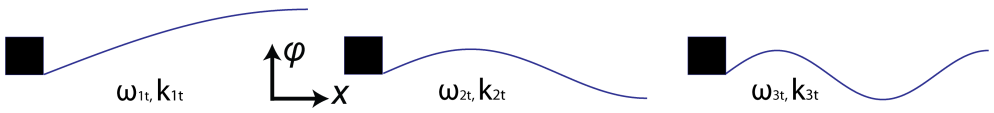

Figure 2.6: *Theoretical modeshapes of the first three torsional modes of a rectangular cantilever. The shape represents the angle of torsion about the cantilevers long axis.*

The equation of motion for torsional oscillations, where $\Phi(x,t)$ is the torsional angle of deflection along the cantilever long axis, is[1]

$$\frac{\partial}{\partial x}\left(GK\frac{\partial\Phi(x,t)}{\partial x}\right)-\rho_c I_p\frac{\partial^2\Phi(x,t)}{\partial t^2}=M(x,t), \tag{2.13}$$

where $M(x,t)$ is an externally applied torque per unit length in the x-direction, G is the shear modulus of the cantilever and K and I_p are geometric functions of the cantilever given by $K=wt^3/3$ and $I_p=(w^3t+wt^3)/12$, or $I_p\approx w^3t/12$ for thin rectangular cantilevers. The values of w and t may depend upon x and therefore the geometric functions likewise.

Solutions of the form $\Phi(x,t)=\phi(x)T(t)=u_{nt}(x)\exp^{-i\omega_{nt}t}$ can be used in equation (2.13) which gives

$$\frac{1}{u_{nt}(x)}\frac{\partial^2 u_{nt}(x)}{\partial x^2}=-\frac{\rho_c I_p\omega_{nt}^2}{GK}. \tag{2.14}$$

The solutions to equation (2.14) are the torsional eigenmodes

$$u_{nt}(x)=A\cos(z_{nt}x/l)+B\sin(z_{nt}x/l), \tag{2.15}$$

where z_{nt} are the torsional eigenvalues and the constants A and B are determined by the boundary conditions. For a cantilever fixed at one end the constant A, is zero and the modeshapes are simply sine functions scaled by a factor B.

The frequency of each of the torsional modes may be calculated using[58]

$$\omega_{nt}=\frac{z_{nt}}{l}\sqrt{\frac{GK}{\rho_c I_p}}. \tag{2.16}$$

The torsional eigenvalues can be calculated using $z_{nt}=\frac{\pi}{2}(2n-1)$.[58]

For a typical rectangular cantilever (such as cantilever R-E) the first torsional spring constant is around 2×10^{-9} Nm. The maximum angle

of oscillation of the first torsional mode can be calculated using equation (2.4) to be around 1.4×10^{-6} radians or 8.4×10^{-5} degrees at 300 K. This remarkably small angle corresponds to a maximum vertical deflection of only 0.25 Å occurring at the edge of the cantilever at its free end for the cantilever R-E as described in section 2.3.1.

The torsional eigenmodes can also be captured by the simulation and are displayed in figure 2.7 where the cantilever is shown in the plan elevation and the fixed end of the cantilever is to the left side of each subfigure. The colour scale represents the out of plane deflection which is associated with the torsional angle and replicates the theoretical angular deflection of figure 2.6.

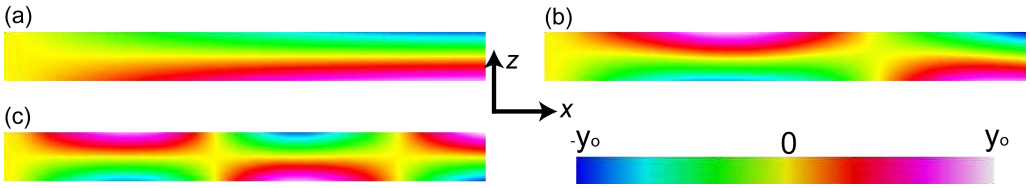

Figure 2.7: *Figure showing the displacements (out of the page, given by the colour scale) representing the modeshapes of the first three torsional modes of a rectangular cantilever as determined by a FEA simulation. (a): fundamental (first) torsional mode, (b): second torsional mode, (c): third torsional mode.*

2.3.3 Other Eigenmodes

Rectangular cantilevers not only oscillate in the flexural and torsional modes but in others too. The lateral mode is a bending of the cantilever which is parallel to the cantilever's plan view area, i.e. the bending is in the z-direction of figure 2.1. This mode has much higher spring constants (and therefore resonance frequencies) than the flexural modes as the can-

tilever has to bend against its width which is typically much greater than its thickness. A cantilever also exhibits extensional vibrations related to the expansion and contraction of its length. Both of these modes are difficult to observe in many experimental setups as they do not cause any vertical movement of the cantilever.

2.3.4 Order of the Eigenmodes

The various different eigenmodes of the rectangular cantilever described above are ordered in frequency space as displayed in table 2.2. In general

Mode	f_n	Frequency (kHz)	Ratio
1^{st} flexural	f_1	11.763	f_1
2^{nd} flexural	f_2	74.667	$6.3f_1$
3^{rd} flexural	f_3	212.641	$18.1f_1$
1^{st} torsional	f_{1t}	234.543	$19.9f_1$
lateral	-	403.629	$34.3f_1$
4^{th} flexural	f_4	428.155	$36.4f_1$
5^{th} flexural	f_5	714.412	$60.7f_1$
2^{nd} torsional	f_{2t}	720.563	$61.3f_1$
6^{th} flexural	f_6	1109.541	$94.3f_1$
3^{rd} torsional	f_{3t}	1288.943	$109.6f_1$

Table 2.2: *Simulated resonance frequencies of an ideal rectangular cantilever, based on the cantilever known as R-E later in the document.* ρ_c*=2330 kg/m*^{3}*,* E*=180 GPa, and* σ*=0.3 have been used as the density, Young's modulus, and Poisson ratio of silicon.[59]*

this ordering of the modes should be seen as a guide for the relative

positions of the resonance frequencies for this, and similar, cantilevers. The dimensions of the simulated cantilever were l=350 μm, w=35 μm and t=1 μm, the materials properties were those of silicon.

2.4 Eigenmodes of Non-Rectangular Cantilevers

The solution of the equations of motion governing non-rectangular cantilevers is, in general, more difficult than for rectangular cantilevers. It is common for the eigenmodes of non-rectangular cantilevers to be built up by a superposition of the solutions of rectangular cantilevers in the Ritz method[1,60] under the assumption that anticlastic curvature can be ignored.[44] In this section a V-shaped cantilever is used as an example of a non-rectangular cantilever.

2.4.1 Flexural Eigenmodes of V-shaped Cantilevers

The flexural eigenmodes of an ideal V-shaped cantilever are shown in figure 2.8. This particular V-shaped cantilever shall be known as V-D throughout this document. The deflection of each leg in each of the flexural modes is similar in profile to the deflection of a rectangular cantilever in each mode. The parallel beam approximation considers the V-shaped cantilever and replaces its two legs with an equivalent rectangular cantilever.[61] Along with use of the Ritz method, the flexural properties of V-shaped cantilevers can be described adequately.

2.4.2 Torsional Eigenmodes of V-shaped Cantilevers

Currently, there exists no satisfactory analogue (or extension) of the Ritz method to calculate the torsional mode shapes of V-shaped cantilevers.

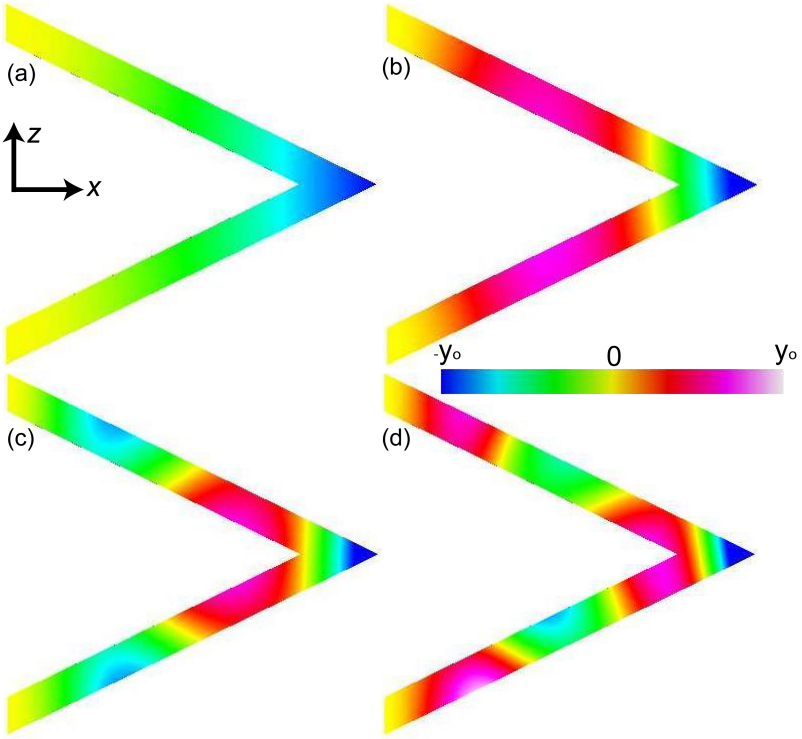

Figure 2.8: *Depiction of the modeshapes of the first four flexural modes of a V-shaped cantilever as determined by a FEA simulation. The cantilever is shown in the plan elevation and the fixed end of the cantilever is to the left side of each subfigure. The colour scale represents a flexural deflection of arbitrary unit. (a): fundamental (first) flexural mode, (b): second flexural mode, (c): third flexural mode, (d): fourth flexural mode.*

The parallel beam approximation has been used but has been shown to underestimate the spring constant of such cantilevers through mistreatment of the effect of the joining of the two legs.[61] In this study the torsional modeshapes of V-shaped cantilevers are determined via finite element simulations with Elmer,[55] the results of which are depicted in figure 2.9.

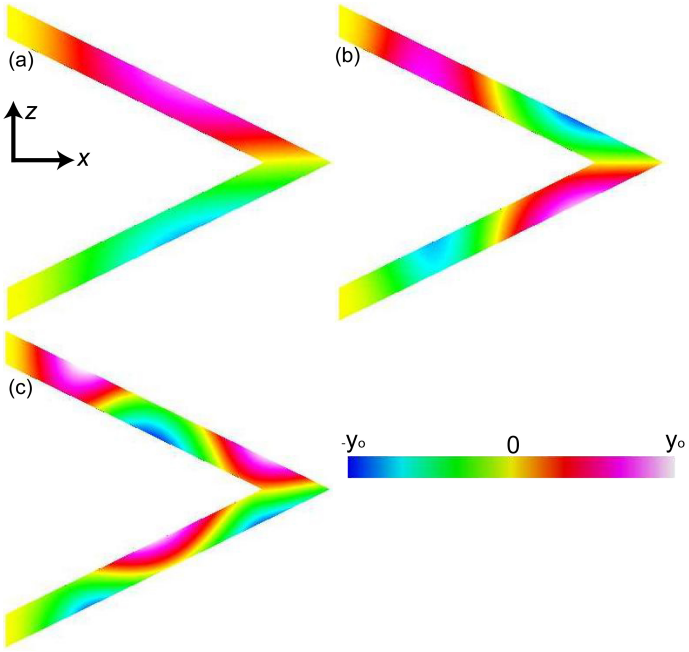

Figure 2.9: *Figure showing the displacements (out of the page, given by the colour scale) representing the modeshapes of the first three torsional modes of a V-shaped cantilever as determined by a FEA simulation. The cantilever is shown in the plan elevation and the fixed end of the cantilever is to the left side of each subfigure. The colour scale represents the out of plane deflection which is associated with the torsional angle. (a): fundamental (first) torsional mode, (b): second torsional mode, (c): third torsional mode.*

2.4.3 Other Eigenmodes of V-shaped Cantilevers

In addition to the lateral and extensional type of eigenmodes, described in section 2.3.3, V-shaped cantilevers exhibit further modes due to their two-legged geometry. One particular mode is where the two legs exhibit their own torsional motions. These flapping motions are either in sync where both legs have the same angle at a given time (figure 2.10(b)) or out of sync where the legs have angles of the same magnitude but different sign (figure 2.10(a)). These modes have not been extensively studied in the literature as their contribution to the movement of a tip

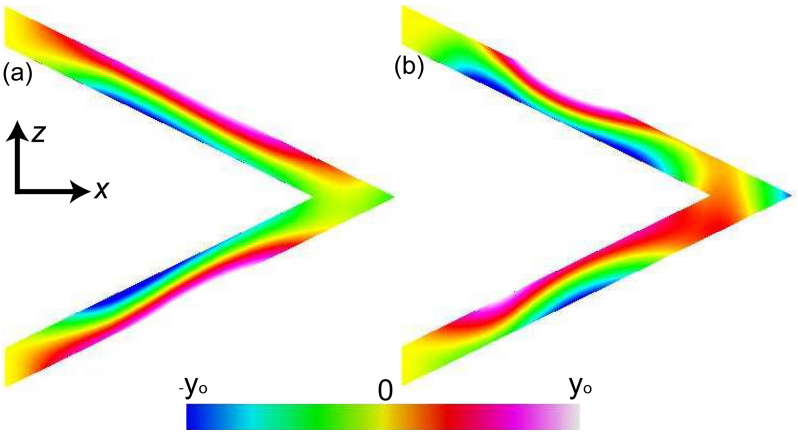

Figure 2.10: *Figure showing the displacements (out of the page, given by the colour scale) representing the modeshapes of two flapping modes of a V-shaped cantilever as determined by a FEA simulation. The cantilever is shown in the plan elevation and the fixed end of the cantilever is to the left side of each subfigure. The colour scale represents the out of plane deflection. (a): out of sync mode, (b): in sync mode.*

is minimal so they are ignored in AFM applications.

2.4.4 Order of the Eigenmodes

The various different eigenmodes of the V-shaped cantilever described above are ordered as in table 2.3. In general this ordering of the modes should be seen as a guide for the relative positions of the resonance frequencies for this, and similar, cantilevers. The dimensions of the simulated cantilever were l=196 μm, w=20 μm, t=0.6 μm and 2θ=52°, the materials properties were those of silicon nitride.

2.5 Normalisation of the Eigenmodes

Throughout this work the following normalisation of the modeshapes is made[44]

$$\int_0^l \rho_c S(x) u_n(x) u_m(x) dx = \delta_{nm} \tag{2.17}$$

Mode	f_n	Frequency (kHz)	Ratio
1^{st} flexural	f_1	28.938	f_1
1^{st} torsional	f_{1t}	148.962	$5.2f_1$
2^{nd} flexural	f_2	172.088	$5.9f_1$
2^{nd} torsional	f_{2t}	479.360	$15.6f_1$
3^{rd} flexural	f_3	504.209	$17.4f_1$
3^{rd} torsional	f_{3t}	943.674	$32.6f_1$
4^{th} flexural	f_4	1062.830	$36.7f_1$
symmetric flapping	-	1418.524	$49.0f_1$
anti-symmetric flapping	-	1621.130	$56.0f_1$

Table 2.3: *Simulated resonance frequencies of an ideal V-shaped cantilever, based on the cantilever known as V-D later in the document.* ρ_c*=3340 kg/m*^{3}*,* E*=310 GPa, and* σ*=0.3 have been used as the density, Young's modulus, and Poisson ratio of silicon nitride.[59]*

where δ_{nm} is the Dirac delta and $S(x) = w(x)t(x)$ is the cross section of the cantilever. The normalisation gives $u_n(x)$ the dimension of [mass]$^{-0.5}$. The maximum kinetic energy of each mode, T_{max}, can then be expressed as follows[44]

$$T_{max} = \frac{1}{2}\omega_n^2 \int_0^l \rho_c S(x) u_n^2(x) dx = \frac{1}{2}\omega_n^2. \tag{2.18}$$

The frequency of each mode can be calculated from its normalised mode-shape. Each mode has an intrinsic bending moment, M_n, associated with the second spatial derivative of the modeshape, $u_n(x)''$:[62]

$$M_n(x) = EI(x)u_n(x)''. \tag{2.19}$$

The resonance frequency of each mode can then be calculated using[44]

$$\omega_n^2 = \int \frac{M_n(x)^2}{EI(x)} dx. \tag{2.20}$$

The effective oscillating mass and dynamic spring constant of each eigenmode of the cantilever are also easily calculable:[44]

$$m_{c,n} = \frac{\int_0^l w(x)t(x)dx}{\int_0^l w(x)t(x)u_n^2(x)dx}, \tag{2.21}$$

and

$$k_n = \omega_n^2 \frac{\int_0^l w(x)t(x)\psi(x)dx}{\int_0^l w(x)t(x)\psi(x)u_n^2(x)dx}. \tag{2.22}$$

In equation (2.22) the function $\psi(x)$ describes the distribution of positions at which the spring constant should be calculated.

3 Microcantilevers as Ultrasensitive Probes of Adsorbed Mass

This chapter is based upon the publication in ref.[21]. In particular sections 3.1, 3.2, 3.3 and parts of section 3.6 appear almost exactly as in the reference.

3.1 Introduction

Micro- and nanocantilever sensors are attracting an increasing amount of attention due to their wide availability and outstanding sensing capabilities.[40, 41, 63, 64] One area that is currently of significant interest is mass sensing,[65] and one goal is to achieve highest mass sensitivity with micro- and nanomechanical devices.[66] It has been demonstrated that such devices are capable of detecting single cells,[67] bacteria,[68] and even single biological molecules.[69]

In the context of mass sensing the determination of masses that are non-homogeneously distributed or that are only attached in specific areas along the cantilever is of pivotal importance since cantilevers can be modified as such.[64] Mass sensing based on the frequency changes of the flexural modes that are due to one or two discretely attached masses[70, 71] as well as a homogeneous mass distribution along the full length of the cantilever in connection with the first flexural mode have been reported in the literature, e.g. ref.[72].

However, there is no general description relating the frequency changes of the higher flexural modes to an attached mass that is homogeneously or non-homogeneously distributed along the cantilever. Even the dis-

crete attachment of small spheres to microcantilevers[70,71] does strictly speaking create a mass distribution localised around the positions of the spheres. The size and weight of the attached masses determine whether a point mass model is still valid. In the case of single objects which cannot be described by a point mass[73] or if the mass is distributed over a certain region of the plan view area of the cantilever, a proper mass model has to be used to correctly describe the oscillation behaviour and the resulting frequency change of the cantilever. Knowledge of the effective oscillating cantilever mass related to the flexural modes is therefore crucial for a quantification of the adsorbed mass.

In this chapter general expressions for the effective oscillating cantilever mass and of the frequency shifts that are caused by an arbitrary distribution of mass attached along a cantilever are derived for all flexural modes. The cantilever can be of any shape as long as its true flexural deflection can be approximated by a function that only depends on the coordinate along the cantilever length. This is the case for the most common types of microcantilevers, namely rectangular, picket, and V-shaped.[44] The results are expressed in terms of the modal shapes of the free cantilevers and their oscillating frequencies. The formulas allow for the determination of the total attached mass under any mass distribution. To test the theoretical findings they are compared with experimental data.

The added mass in this study is due to the adsorption of water molecules upon the cantilever's surface as the relative humidity surrounding the cantilever is varied. The relative humidity is a measure of how much water vapour is present in a given volume relative to the maximum possible

amount. The maximum capacity of water in a gas varies with temperature. This study provides an opportunity to investigate the formation of thin layers of water on surfaces, a topic of particular interest in microelectromechanical systems (MEMS) where capillary forces between adsorbed water layers can have significant influence on performance.[74, 75] Initially, cantilevers that were used as received are discussed in section 3.3. The study is then extended to cantilevers coated with self-assembled monolayers (SAMs) to increase the sensitivity to mass and to investigate the possible effects of adsorption induced surface stress (section 3.5).

3.2 Theoretical Background

If a small external mass is attached to a cantilever its dynamic properties will change according to the additional effective mass. In the following it is assumed that the total external mass is small compared to the total mass of the cantilever and that the external mass per unit area is constant over the dimension of the cantilever width. The external mass per unit length, $\Delta m_{ext}(x)$, is determined by the density of the external mass, $\rho_{m,ext}(x)$, the width of the beam, $w(x)$, and the thickness of the layer, $t_{ext}(x)$:

$$\Delta m_{ext}(x) = \rho_{m,ext}(x) S_{m,ext}(x) \tag{3.1}$$

with $S_{m,ext}(x) = w(x)t_{ext}(x)$. This equation can be rewritten as $\Delta m_{ext}(x) = \Delta m_{ext,0}\varphi(x)w(x)$ where $\Delta m_{ext,0}$ is the maximum value of the mass per unit area and $\varphi(x)$ describes the variation of the mass along the cantilever length. The total external mass acting on the cantilever is $\Delta M_{ext} = \int_0^l \Delta m_{ext}(x)dx$ where l is the cantilever length. The external mass causes a shift $\Delta(\omega_n^2) = \omega_n^2 - \omega_{n0}^2$ in the eigenfrequency of the n^{th} flexural mode, where

ω_n^2 is the resonant frequency with external mass, and ω_{n0}^2 the unperturbed resonant frequency without additional mass. The relation between the unperturbed resonant frequency ω_n, the total external mass, $\Delta M_{ext}(x)$, and the resulting shift in the resonant frequency of the n^{th} mode, $\Delta(\omega_n^2)$, of the cantilever is

$$\Delta(\omega_n^2) = -\omega_{n0}^2 \frac{\Delta M_{ext}}{m_{c,n}}, \tag{3.2}$$

if the frequency shift is entirely due to additional mass, i.e. there are no stress effects. $m_{c,n}$ is the effective oscillating mass of the cantilever in the n^{th} mode under the mass distribution $\varphi(x)$. If the total external mass is small compared to the cantilever mass such that the eigenmodes of the cantilever are not significantly affected then the total energy of the cantilever beam before and after adsorption is

$$\frac{1}{2}\omega_{n0}^2 \int_0^l \rho_c S(x) u_n^2(x) dx \approx \frac{1}{2}\omega_n^2 \int_0^l \rho_c S(x) u_n^2(x) dx + \frac{1}{2}\omega_n^2 \int_0^l \rho_{ext} S_{ext}(x) u_n^2(x) dx. \tag{3.3}$$

Because of the normalisation (equation (2.17)) the relative frequency shifts $\Delta(\omega_n^2)/\omega_n^2$ are

$$\frac{\Delta(\omega_n^2)}{\omega_n^2} = \int_0^l \rho_{ext} S_{ext}(x) u_n^2(x) dx = -\Delta m_{ext,0} \int_0^l \varphi(x) w(x) u_n^2(x) dx. \tag{3.4}$$

Of practical interest is the total external mass,

$$\Delta M_{ext} = \Delta m_{ext,0} \int_0^l \varphi(x) w(x) dx, \tag{3.5}$$

which can be obtained in combination with equation (3.4)

$$\Delta M_{ext} = -\frac{\Delta(\omega_n^2)}{\omega_n^2} \frac{\int_0^l \varphi(x) w(x) dx}{\int_0^l \varphi(x) w(x) u_n^2(x) dx}. \tag{3.6}$$

The effective mass of the cantilever, $m_{c,n}$, in the n^{th} flexural mode is therefore

$$m_{c,n} = \frac{\int_0^l \varphi(x) w(x) dx}{\int_0^l \varphi(x) w(x) u_n^2(x) dx}. \tag{3.7}$$

Note that the effective mass of the cantilever can be lower as well as higher than the actual mass of the cantilever, $m_c = \int_0^l \rho(x)S(x)dx$, depending on the external mass distribution $\varphi(x)$. Equations (3.6) and (3.7) are applicable to all kinds of cantilevers and any external mass distribution. The eigenfrequencies, ω_n, the frequency shifts, $\Delta(\omega_n^2)$, and the cantilever width, $w(x)$, can be determined experimentally. The mass distribution $\varphi(x)$ along the cantilever is also often specified by the experimental conditions.

3.3 Unmodified Cantilevers

3.3.1 Experimental Section

To test the theoretical results a commercially available rectangular silicon cantilever (350 μm long, 0.03 N/m , R-E, Mikromasch[47]) and a V-shaped silicon nitride cantilever (196 μm long, 0.06 N/m, V-D, Veeco[76]) were exposed to relative humidity values in the range of ≈2% to ≈25% at 22 °C, similar to the experiments described in ref.[77]. Cantilevers were used as received. They can homogeneously adsorb small amounts of water at those humidity values. Experiments were performed with an AFM Explorer system (ThermoMicroscopes, Sunnyvale, CA, USA). Power spectral densities of thermal noise spectra were recorded with an external interface (National Instruments, USB-6251) as a function of humidity. Figures 3.1 and 3.2 display the experimentally obtained power spectral densities of the resonance peaks for both the rectangular and the V-shaped cantilever together with their resonance frequency values at low humidity and the Q-factors. Resonant frequency values, Q-factors, and

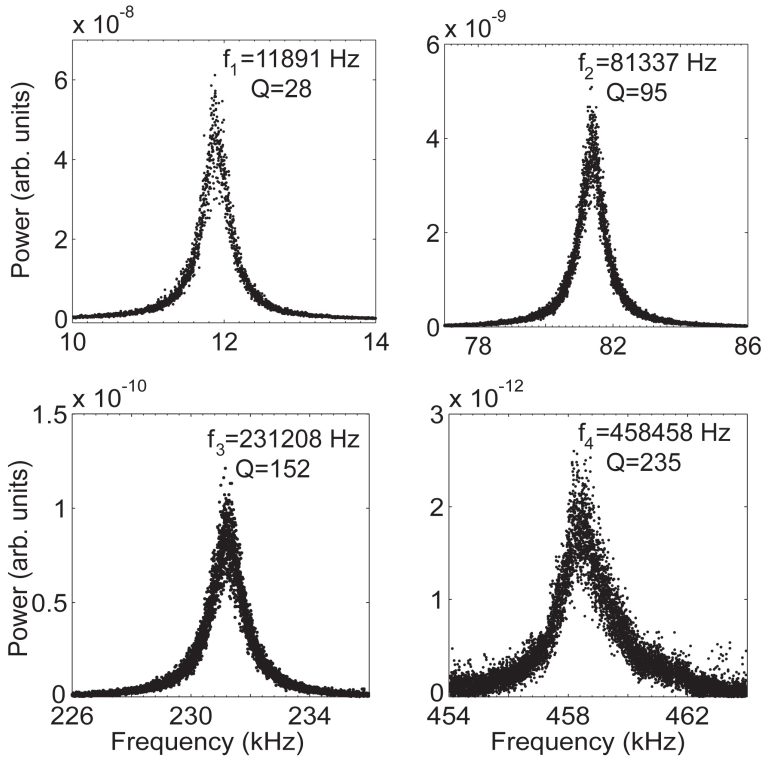

Figure 3.1: *Thermal noise power spectral densities of the first four flexural modes obtained for the rectangular cantilever. While the Q-factor increases with the mode number the signal-to-noise ratio decreases.*

peak areas for each mode were determined during measurement with a homewritten LabVIEW^{TM} routine by fitting Lorentzians to the resonance peaks similar to the procedure described in ref.[78].

The resonant frequency values are based on the average of 50 individual spectra. The Q-factors showed fluctuations below 3% for all resonance peaks with no clear trend towards lower or higher values with increasing humidity. Q-factors can therefore be considered as constant and independent of humidity in our experiments. The mass sensitivity or minimum detectable mass δM of the system is given by $\delta M = -\frac{\delta(\omega_n^2)}{\omega_{n0}^2} m_{c,n} \approx -2m_{c,n}\frac{\delta\omega_n}{\omega_{n0}}$,[79] where $\delta\omega_n$ is the minimum measurable frequency shift of mode n. Note that the mass sensitivity depends on the effective os-

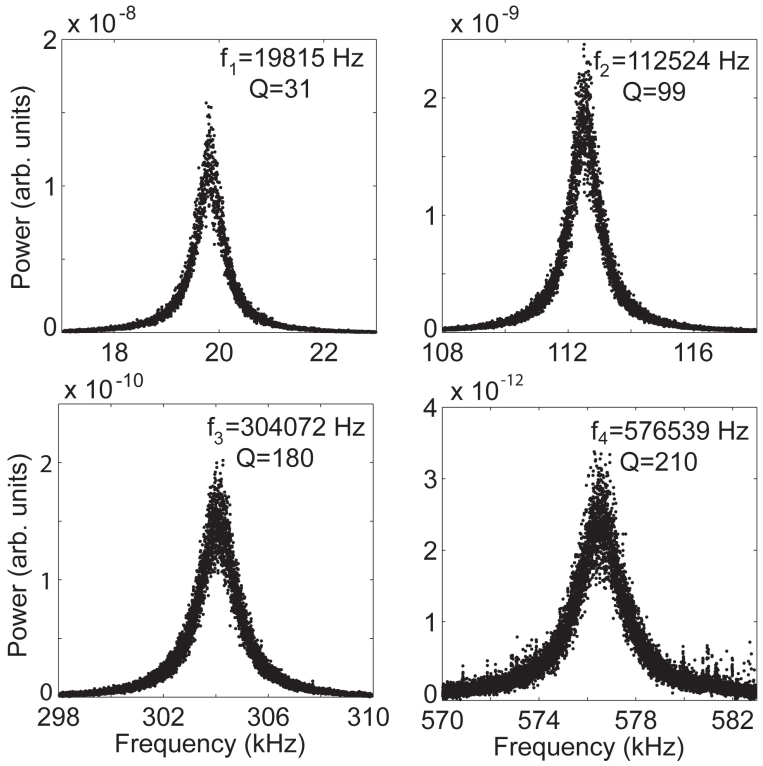

Figure 3.2: *Thermal noise power spectral densities of the first four flexural modes obtained for the V-shaped cantilever. While the Q-factor increases with the mode number the signal-to-noise ratio decreases.*

cillating mass of the cantilever and hence the mass distribution of the externally accreted mass. In general, the mass sensitivity increases with increasing Q-factor. Thermal fluctuations, fluctuations in humidity, as well as the signal-to-noise ratio, which decreases with increasing mode number in our experiment, all have an influence on the resulting sensitivity.[79] In order to determine the sensitivity in our experiments with thermally driven cantilevers the standard deviation, δf_n, of the measured resonant frequency values, f_n, at constant humidity was taken as the minimum detectable frequency shift for each mode. The standard deviation values were determined from the fluctuations of 15 recordings of the resonant frequency values of the four modes at a fixed humidity. The values

obtained were 4.3 Hz, 7.4 Hz, 7.5 Hz, and 8.7 Hz for modes one to four of the rectangular cantilever, respectively. The corresponding values for the V-shaped cantilever were: 3.9 Hz, 7.6 Hz, 10.7 Hz, and 37.2 Hz. Error bars of the relative frequency shifts $\Delta(\omega_n^2)/\omega_{n0}^2$ and hence sensitivities in our experiment are based on these standard deviations δf_n and are given by $\delta\left(\frac{\Delta(\omega_n^2)}{\omega_{n0}^2}\right) \approx -2\sqrt{2}\frac{\delta f_n}{f_n}$.

3.3.2 Results and Discussion

If a single point-mass is attached to a cantilever at position $x = l_{M_{ext}}$ then $\varphi(x) = \delta(x - l_{M_{ext}})$ and the relative frequency shift $\Delta(\omega_n^2)/\omega_{n0}^2$ is proportional to $u_n^2(l_{M_{ext}})$, which is the same as the result reported in ref.[80]. This finding can be easily extended to the case of several discretely attached masses[71] with equation (3.6). If an area between $x = l_1$ and $x = l_2$ along a cantilever is modified such that a certain analyte can only adsorb in this region then $\varphi(x) = 1$ for $l_1 \leq x \leq l_2$ and $\varphi = 0$ elsewhere (see figure 3.3).

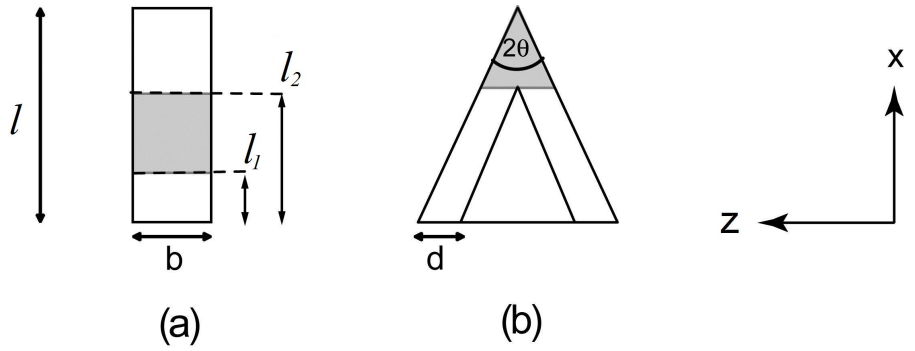

Figure 3.3: *Schematic top view of (a) rectangular and (b) V-shaped cantilevers. The shaded areas indicate external mass adsorption in these areas only, i.e. $\varphi(x) = 1$ for all x-coordinates corresponding to the shaded area and $\varphi(x) = 0$ elsewhere.*

Equation (3.6) is particularly simple for rectangular cantilevers where w is constant. The total adsorbed mass can then be obtained from

$\Delta M_{ext} = -\Delta(\omega_n^2)/\omega_{n0}^2 \cdot \Delta l / \int_{l_1}^{l_2} u_n^2(x)dx$ **with** $\Delta l = l_2 - l_1$**. If the entire length of the plan view area can adsorb mass, i.e.** $\Delta l = l$**, then** $m_{c,n}$ **corresponds to the total mass of the cantilever for all modes, and equation (3.2) can be used to determine the adsorbed mass simply based on the measured frequency shift and the total mass of the cantilever. If** Δl **does not correspond to the full length, the** $m_{c,n}$ **values will in general be different from the total cantilever mass and also be different for different modes. Figure 3.4 summarizes the results for the relative frequency shifts**

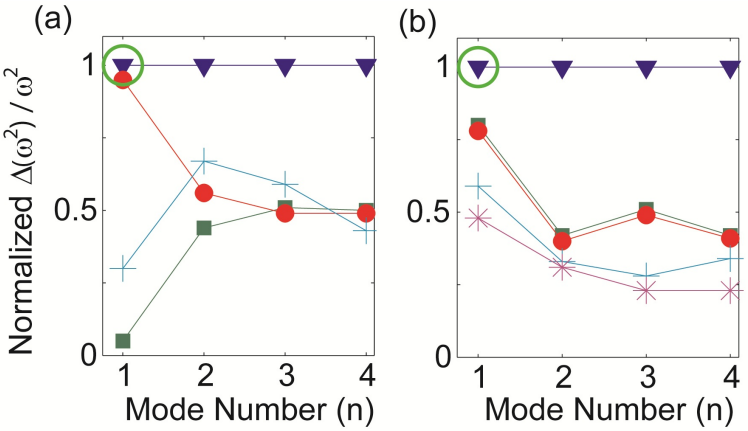

Figure 3.4: $\Delta(\omega_n^2)/\omega_{n0}^2$ *values for the first four flexural modes of (a) rectangular and (b) V-shaped cantilevers and several mass distributions* $\varphi(x)$*.* $\Delta(\omega_n^2)/\omega_{n0}^2$ *in each figure is normalized to the encircled* $\Delta(\omega_1^2)/\omega_{10}^2$ *value. Mass distributions on rectangular cantilevers are for* $l_1 = 0$*,* $l_2 = l$ *(▼),* $l_1 = 0$*,* $l_2 = l/2$ *(■),* $l_1 = l/2$*,* $l_2 = l$ *(●), and* $l_1 = l/4$*,* $l_2 = 3l/4$ *(+). Mass distributions on V-shaped cantilevers (2θ=51.2°) are for adsorption over the full length (▼), and for adsorption on the triangular part only (see figure 3.3): V-A (■) l=115, d=25; V-B (●) l=196, d=41; V-C (+) l=115, d=17; V-D (*) *l=196, d=23. All dimensions are in micrometres.*

$\Delta(\omega_n^2)/\omega_{n0}^2$ **of the first four flexural modes of rectangular and V-shaped cantilevers, and for different adsorbed mass distributions (see figure 3.3). For V-shaped cantilevers the modal shapes** $u_n(x)$ **were obtained as de-**

scribed in ref.[44]. The resulting relative shifts were normalized to the $\Delta(\omega_1^2)/\omega_{10}^2$ value for full-length adsorption (encircled in figure 3.4). Note that the results for rectangular and V-shaped cantilevers are independent from their specific dimensions if the entire cantilever can adsorb mass.

Figure 3.5 shows the experimentally obtained $\Delta(\omega_n^2)/\omega_{n0}^2$ values for a relative humidity of up to ≈25% and the first four flexural modes of both the rectangular and the V-shaped cantilever.

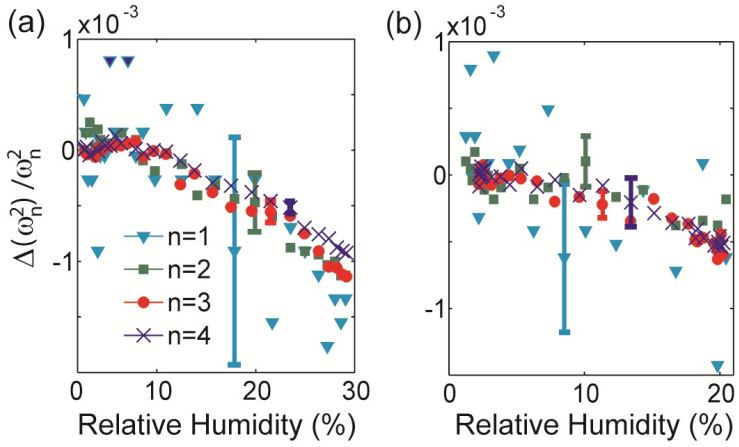

Figure 3.5: *Experimentally determined $\Delta(\omega_n^2)/\omega_{n0}^2$ values for (a) a rectangular and (b) a V-shaped cantilever and the first four flexural modes at different relative humidity values. The cantilevers can adsorb water over their full length. Error bars are based on the experimentally determined fluctuations in the resonant frequency values (standard deviation) at constant humidity. Only one error bar for each mode is shown for clarity.*

All modes show the same trend of $\Delta(\omega_n^2)/\omega_{n0}^2$ over the humidity range studied for both the rectangular and the V-shaped cantilever, confirming the theoretical results for cantilevers that can adsorb mass over their full length. While the error bar is quite large for the first mode it is significantly smaller for the higher modes indicating a relatively low mass sensitivity for the first mode and higher sensitivities for the higher modes. The minimum detectable mass values that are based on the fluctuations

in the resonant frequencies at constant humidity can be converted to water film thickness, which is the parameter of interest here. The resulting minimum detectable film thicknesses are: 13.7 Å, 3.2 Å, 1.1 Å, and 0.7 Å based on the first four modes of the rectangular cantilever, respectively. These thicknesses correspond to minimum detectable masses of 33.5 pg, 7.8 pg, 2.7 pg and 1.7 pg for the first four modes. The corresponding values for the minimum detectable thicknesses using the V-shaped cantilever are 8.6 Å, 3.0 Å, 1.5 Å, and 2.8 Å, which relate to mass sensitivities of 6.0 pg, 2.1 pg, 1.1 pg and 2.0 pg for the first four flexural eigenmodes. The decrease in the sensitivity of the fourth mode in the case of the V-shaped cantilever is due to the relatively large fluctuations in the resonant frequency of the cantilever used.

The sensitivity values obtained underline that the accreted mass and the thickness of the film adsorbed onto a cantilever surface can be determined with high accuracy when using higher flexural modes. The reason is that the absolute frequency shifts $\Delta(\omega_n^2)$ are higher for the higher modes granting them a higher accuracy for low masses in general. The water film thickness can be obtained with equation (3.6) and amounts to around 7 Å at 25% relative humidity. This result is in good agreement with values reported in the literature.[81] For the rectangular cantilever a thickness of water of 7 Å corresponds to a mass of around 17 pg adsorbed around the cantilever surface.

Note that stress induced by the adsorbed mass would be reflected by different $\Delta(\omega_n^2)/\omega_{n0}^2$ values for different modes at constant humidity. The simultaneous measurement of $\Delta(\omega_n^2)/\omega_{n0}^2$ values for several flexural modes in combination with equation (3.6) could therefore be exploited

to separate frequency changes that are due to mass from those that are due to stress (see also section 3.5).

3.4 Higher Humidities

The trend shown in the experimental results of section 3.3.2 should continue throughout the whole range of possible relative humidities. To achieve humidities above that of the external atmosphere nitrogen gas was bubbled through deionised water before being pumped into the humidity cell. Otherwise, the experimental setup used was as described in section 3.3.1.

Figure 3.6 shows the amount of water adsorbed on a V-shaped cantilever through a large humidity range. The amount of water adsorbed is

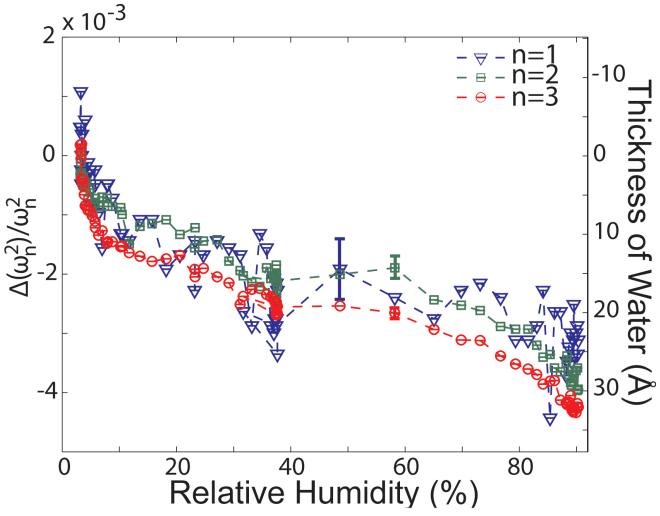

Figure 3.6: *Experimentally determined water layer thickness values for a V-shaped cantilever and the first three flexural modes at different relative humidity values. The cantilever can adsorb water over its full length. Only one error bar for each mode is shown for clarity.*

broadly in agreement with that in the previous section. Similar results

for rectangular silicon cantilevers were also collected.

It is clear from figure 3.6 that the thickness of the adsorbed water layer does not increase linearly with humidity, rather it has a more complicated dependence. At low humidities the layer thickness increases relatively swiftly, followed by a period of slow growth in the mid range of humidities. Once above ≈80% relative humidity the layer thickness again grows more swiftly with increasing humidity.

This behaviour has been observed previously[81, 82] and can be explained by considering how the structure of the adsorbed water layer develops as the humidity and hence layer thickness increases, as depicted in figure 3.7. In the lower humidity range ($\lesssim 30\%$) an 'ice like' struc-

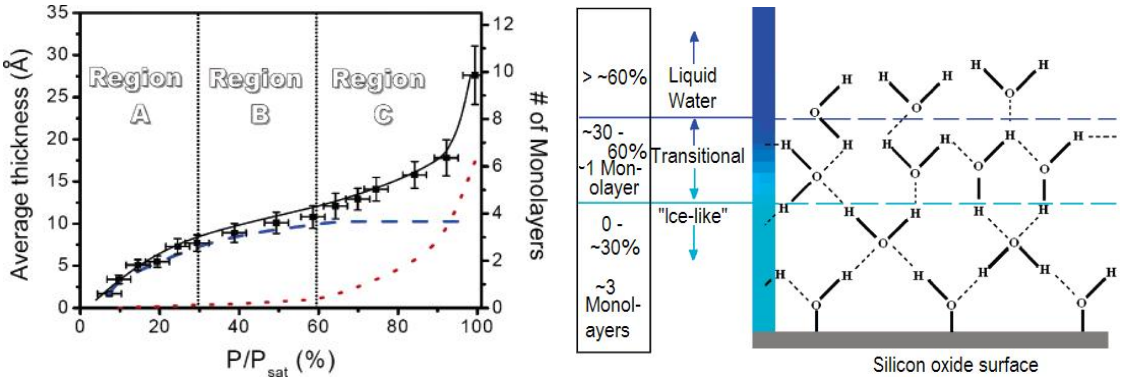

(a) *Adsorption isotherm of water on a silicon oxide surface*

(b) *Molecular arrangement of water on a surface*

Figure 3.7: *Evolution of an adsorbed water layer on a silicon oxide surface. Figure adapted with permission from ref.[81].*

ture forms where water molecules hydrogen bond to the oxidised silicon surface in a regular order. Water molecules readily attach and so the film grows swiftly. For most solvents only one monolayer of the ice-like structure is observed but due to water's propensity for hydrogen bond formation the structure can grow to two or three monolayers deep. Be-

tween $\approx 30\%$ and $\approx 60-80\%$ relative humidity the adsorbed layer grows slowly as the structure of new water molecules on the surface becomes less ordered. From upwards of around $60-80\%$ newly adsorbed molecules take up a much more random orientation similar to that of a liquid. The film grows exponentially with increasing relative humidity.

The results displayed in figure 3.6 indicate that the liquid like regime begins at a higher humidity than reported in some studies.[81] In our experiments it is possible that the humidity sensor could read a different humidity than that felt by the cantilever, though certainly no more than around 5-10%. The cantilever and humidity sensor are positioned as close as possible in an attempt to negate such effects. The fact that cantilevers in this study were used without any cleaning means that there will be some contamination with organic molecules from the atmosphere which is likely to make the surface mildly hydrophobic.

3.5 Cantilever Modification

Cantilevers may be modified to increase their sensitivity. The result of increasing their sensitivity could be that the static bending or frequency shift due to a given amount of adsorbate is enhanced. Coatings may be applied to impart some specificity to a certain adsorbate molecule.[33,34, 38] This has been studied before for the fundamental mode,[33] and the higher modes of oscillation should be similarly enhanced by modification, which is tested in this section.

A self-assembled monolayer (SAM) was formed on the surface of a cantilever to modify its properties. SAMs are surfaces formed by the adsorption and regular organisation of organic molecules onto a surface.

A SAM system is depicted in figure 3.8. A SAM molecule consists of

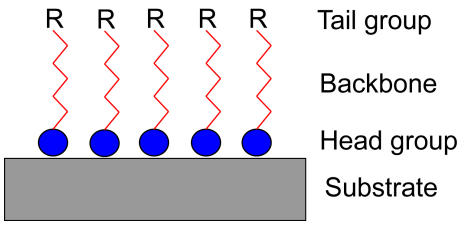

Figure 3.8: *Side-on view of the key components of a SAM.*

three parts; a head group for bonding with a substrate, a hydrocarbon backbone, and a tail group which is chosen to give the resulting SAM its required properties. The tail group might already posses the required functionality, e.g. some chemical specificity, or it may be a reasonably reactive group to allow further functionalisation after the coating stage. To demonstrate the potential of coated cantilevers a rectangular cantilever was coated with a hydrophobic silane SAM and exposed to a range of humidities.

3.5.1 Surface Modification Process

A silicon cantilever (of type R-E) was modified with an octadecyltrichlorosilane SAM, figure 3.9. A piece of a silicon wafer was treated in the same

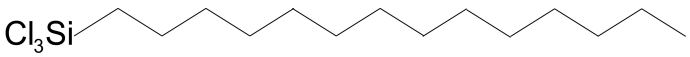

Figure 3.9: *Structure of octadecyltrichlorosilane.*

manner as the cantilever to act as a control. The surfaces were first cleaned to remove any adsorbed organic matter and then oxidised to form a native silicon oxide layer in the following process:[‡]

[‡]The cleaning and modification process was carried out by A. Parkes under the direction of M. Adamkiewicz.

- **Ozonolysis for 30 minutes to break down some organic species into gases or water soluble compounds**
- **Rinsed in distilled water, dried in a stream of nitrogen gas**
- **Washed in a concentrated H_2SO_4/H_2O_2 mixture (2:1, 30% w/w) at $70\,^{\circ}\mathrm{C}$ for 15 minutes to oxidise organic matter**
- **Rinsed in distilled water, dried in a stream of nitrogen gas**
- **Washed in a concentrated $NH_4OH/H_2O/H_2O_2$ mixture (1:5:1, 30% w/w) at $70\,^{\circ}\mathrm{C}$ for 15 minutes to remove any remaining organic species and inorganic contaminants**
- **Rinsed in distilled water, dried in a stream of nitrogen gas**
- **Washed in a concentrated $HCl/H_2O/H_2O_2$ mixture (1:5:1, 30% w/w) at $70\,^{\circ}\mathrm{C}$ for 15 minutes to form a native oxide layer and to precipitate out charged alkali species**
- **Rinsed in distilled water, dried in a stream of nitrogen gas**

The SAM was applied from the solution phase in the following process

- **The solution was prepared by stirring toluene (70 ml) for 15 minutes under a nitrogen atmosphere**
- **Octadecyltrichlorosilane (95%, 0.18μl) was then added and the solution stirred for a further 90 minutes**
- **The surface for modification was left in the stirred solution in a sealed container overnight to allow for SAM formation**
- **Sample removed and sonicated in toluene for 15 minutes**

- **Rinsed in distilled water**
- **Sonicated for 15 minutes in dichloromethane**
- **Rinsed in distilled water, dried in a stream of nitrogen gas**

3.5.2 Results and Discussion

Contact Angle **The water contact angle is the angle between a surface and a water droplet upon it. The contact angle may be used as an identifier of the properties of a surface through its interaction with the droplet. A droplet on a hydrophobic surface will tend to sit proud of the surface and hence have a large contact angle as depicted in figure 3.10(b). In contrast water on a hydrophilic surface will form large flat areas with**

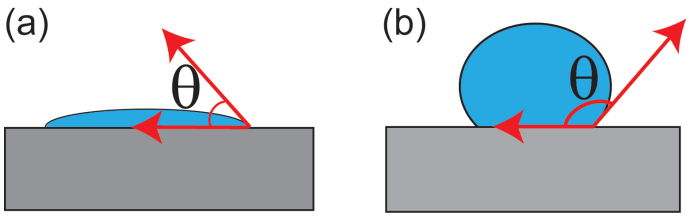

Figure 3.10: *Definition of the contact angle, θ, of a liquid on a surface. (a) shows a small contact angle, for example water on a hydrophilic surface. (b) shows a much larger contact angle, for example water on a hydrophobic surface.*

small contact angles, figure 3.10(a). The contact angles were measured on a piece of a silicon wafer which was treated alongside the cantilever.[§] The initial contact angle was $55\,^{\circ}$, post ozonolysis the contact angle was $37\,^{\circ}$, the decrease due to the removal of hydrophobic organic material. After modification of the surface with octadecytrichlorosilane a contact angle of $109\,^{\circ}$ was obtained, in agreement with the literature.[83] Several areas

[§]All of the contact angles were measured by A. Parkes.

of the wafer were tested and all showed the same contact angle, meaning it is reasonably certain that a homogeneous layer had formed. Further measurements, perhaps by X-ray photoelectron spectroscopy (XPS) or ellipsometry, would be desirable to confirm the film quality.

Frequency Shifts The modified cantilever was assumed to have the same properties as the modified wafer. The cantilever was exposed to a range of humidities and the frequency shifts of all modes were monitored.[¶] The shifts shown in figure 3.11 are much larger than those for unmodified cantilevers. There was no significant change in the static

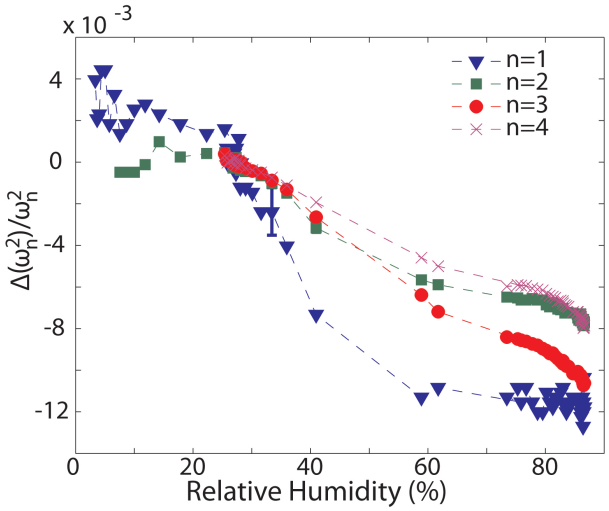

Figure 3.11: *Experimentally determined frequency shifts for a modified rectangular cantilever showing the first four flexural modes at different relative humidity values. Only one error bar for each mode is shown for clarity.*

bending of the cantilever throughout the humidity range. The experiment was repeated on several occasions and similar results were obtained. The maximum shift in the first mode is equivalent to a water thickness of around 170 Å. Since the SAM is hydrophobic it is implausible that the shift is due to the mass of an adsorbed water layer. One explanation

[¶]All experimental data were collected by A. Parkes

could be that the interaction of a small amount of adsorbed water with the SAM induces some stress in the layer, changing the effective spring constant of the cantilever. This can be described using equation (2.3). Under the assumption that the SAM is homogeneous, such that the water may adsorb evenly over the whole cantilever, the quantity $\Delta m_n/m_n$ is the same for all modes and a set of simultaneous equations based upon equation (2.3) can be obtained. Taking two of the modes, say $n = 1$ and $n = 2$, a value for Δk may be calculated. However each combination of modes resulted in a different value of Δk, ruling out this approach. It is probable that the SAM was not entirely homogeneous, a conclusion that is not surprising given a closer inspection of figure 3.11. If an induced stress were distributed over the whole cantilever then it would be expected that it would affect all the modes in a similar manner and the relative shift, $\frac{\Delta(\omega_n^2)}{\omega_n^2}$, should show some consistent trend with mode number. That is to say, for example, $\frac{\Delta(\omega_1^2)}{\omega_1^2} \geq \frac{\Delta(\omega_2^2)}{\omega_2^2} \geq \frac{\Delta(\omega_3^2)}{\omega_3^2} \geq \frac{\Delta(\omega_4^2)}{\omega_4^2}$ at a given humidity, in contrast to the behaviour shown in figure 3.11.

Notice also that there are no frequency shift values for some modes at low humidities and therefore the frequency shifts have been set to zero at the lowest humidity for which data is available for all modes. The resonance peak of the fourth mode was lost at the highest humidity (at ≈25%), followed by the third (at ≈24 %) and second (at ≈8 %) as the humidity was decreased. The mechanism behind this behaviour is unknown.

The most likely explanation of the divergence of the different modes shown in figure 3.11 is that the SAM was not uniform. If water molecules were able to penetrate the volume between the strands of the SAM in

areas of low SAM density then this could relieve stress in the film. The resonance frequencies would then be altered due to the stress change on the surface of the cantilever. Any adsorbed water could also be removed by lowering the humidity, with insignificant hysteresis in the behaviour of the frequency shifts.

3.6 Conclusions and Further Work

Expressions that allow for the determination of the total attached mass on cantilever sensors under any mass distribution and for all flexural modes were derived. The applicability of the equations for the first four flexural modes in the case that mass can adsorb over the full length of a cantilever, and for two different types of cantilevers was demonstrated. Small amounts of mass can be determined accurately and precisely for thermally driven cantilevers, in particular when using higher flexural modes since they show a higher sensitivity towards an accreted mass than the first flexural mode.

The predictions from the theoretical treatment, summarised in figure 3.4, account for the frequency shifts relating to any distribution of added mass. Experimental treatments were restricted to the case where mass can adsorb over the whole cantilever only. A worthwhile extension would be to modify a range of cantilevers such that mass may only adsorb over specific areas to further test the theoretical predictions.

The simultaneous measurement of $\Delta(\omega_n^2)/\omega_{n0}^2$ for several modes opens up interesting possibilities to determine both the adsorbed mass and the stress caused by it. Therefore it might provide a technique to gain information about the interactions inside thin films and between thin

films and substrates.

It has been shown that it is possible to change the response of microcantilever sensors by introducing a coating. A coating may be tailored to the detection of a target molecule depending upon the application, for example the detection of an explosive substance. The higher modes show a smaller experimental error and hence are more relevant to applications where accuracy is of paramount importance. In other applications it may be the case that use of the fundamental resonance is sufficient if the cantilever has been coated successfully to accentuate the frequency shift.

It is to be expected that the torsional modes of microcantilever sensors will show the same behaviour as the flexural modes, and would be an interesting extension of the work in this chapter.

4 Calibration of the Flexural Spring Constants of Microcantilevers through their Interaction with a Flow of Fluid

This chapter is based upon the publication in ref.[84]. In particular sections 4.1, 4.4, 4.5, 4.6, 4.11 and parts of sections 4.7 and 4.8.2 appear almost exactly as in the reference.

4.1 Introduction

Microcantilevers are widely employed as probes in AFM to image surface properties,[2] but also as independent sensors for mass,[21] surface stress,[33] chemical identification,[33] viscosity and density of liquids,[40, 41] or for measuring viscoelastic properties of cells.[29] Small changes in the oscillation properties of the flexural modes of the cantilevers can be exploited to quantify various physical properties provided the spring constants of the flexural modes are known. Chemically modified cantilevers or cantilever sensor systems for biomedical research benefit from simple yet reliable calibration methods, which can be performed in situ and which do not bear the risk of affecting the quality of the modified cantilever.[43, 85, 86]

Most of the current applications make use of the first flexural mode only. The higher flexural eigenmodes of microcantilever sensors however are currently an area of significant interest due to their greater sensitivity for example to mass, as demonstrated in the previous chapter.[21] They are also of interest in relation to dynamic AFM applications with small

tip oscillation amplitudes, where multiple eigenmodes are simultaneously excited,[8] or in high speed AFM setups where the excitation of higher modes may be undesirable.[87] Use of the higher eigenmodes allows one to combine quantitative materials characterisation with high resolution imaging.[22] For example, it is possible to collect an AFM image with the first mode providing topographical information and use the second mode to determine the elasticity of the surface.[25] It has been shown that AFM images of a Si(111)-(7×7) surface collected using the second and third eigenmodes show enhanced signal to noise ratio.[22–24]

Recently, a magnetic force microscope was reported where positioning of a magnetic tip at the node of the second eigenmode allowed characterisation of the vertical (with respect to the surface) force by the first eigenmode along with simultaneous detection of the parallel forces by the second mode.[88]

A pre-requirement for the exploitation of the higher modes, however, is knowledge of the corresponding spring constants. Manufacturer quoted values for the fundamental spring constant have huge ranges, largely due to uncertainties in cantilever thickness. As an example, the rectangular cantilever used in the previous chapter has a nominal spring constant of 0.03 N/m, but a quoted minimum of 0.01 N/m, one third of nominal value and a maximum spring constant of two and a half times (0.08 N/m) the nominal spring constant.[47] In almost any quantitative application it is therefore essential to first calibrate the spring constant of the probe to be used. Note that in the previous chapter the spring constants of the cantilevers were not explicitly determined. However, their dimensions and materials properties were assumed, from which the spring constant

could be calculated.

A comparison of standard calibration methods that are employed in connection with the first flexural mode was reported in ref.[48] and the application of two of these methods to the higher eigenmodes was recently reported.[49] Current calibration techniques all have certain difficulties and disadvantages, and none can calibrate the higher flexural modes easily.[49, 89]

4.2 Existing Schemes for the Calibration of the Flexural Spring Constants of Microcantilevers

A summary of different calibration methods is outlined below, all relate to the fundamental spring constant and only a few may be extended to the higher flexural modes.

4.2.1 Static Methods

Some methods measure the static bending of the cantilever due to masses placed upon it[90] or require pressing the cantilever into a surface.[48, 91, 92] The surface may be a reference cantilever of similar stiffness, in which case its spring constant will have had to be independently determined in some way.[91] Accuracies of ±10-30% have been reported for this method, which is heavily dependent on the calibration of the reference cantilever, which should have a similar static spring constant, k_s, to that which is to be calibrated. Alternatively the cantilever is pushed into a nanoindenter in order to produce a force curve from which the cantilever spring constant may be determined.[92] Accuracies of ±10% have been reported for cantilevers stiffer than 1 N/m, with increasing accuracy for stiffer

cantilevers.

The static spring constant may also be determined from a force curve simply by pushing the cantilever tip into a surface and monitoring its bending for a known force. The force and deflection of the cantilever must be known through an independent route. It is likely that the tip will be blunted in this process.

These methods pose a high risk of damage to the cantilever or to its tip and can only calibrate the static spring constant, but which can be related to the dynamic spring constant of the first flexural mode for ideal cantilevers.[44]

4.2.2 Theoretical Methods

Some methods use accurate measurements of the cantilever dimensions and assumptions of the material properties of the cantilever in finite element analysis simulations to calculate the spring constants of rectangular cantilevers.[93] The original method of ref.[93] has to be modified to correctly account for the bending of the triangular part of V-shaped cantilevers.[48]

If the dimensions (l, w, t as defined in table 0.3) and Young's modulus (E) of the cantilever are known with accuracy then the fundamental flexural spring constant can be simply determined using[91]

$$k_s = \frac{Et^3w}{4l^3} \tag{4.1}$$

for a rectangular cantilever. However, while it is easy to obtain the width and length by optical microscopy the thickness and Young's modulus are much less easy to quantify accurately. The thickness may be determined,

with some difficulty, using electron microscopy but Young's modulus has to be assumed to be equivalent to the bulk value for the material. Even if the thickness is known, it may vary along the length of the cantilever thus requiring the inclusion of a thickness model in equation (4.1). The accuracy of these methods is determined by the measurement of the thickness and the appropriateness of use of bulk values of Young's modulus for a microcantilever.

4.2.3 Dynamic Methods

Other methods exploit information garnered from the resonance frequencies to calibrate the spring constants. Dynamic methods pose a lesser chance of damage to the cantilever and tip than static methods, while being more accurate than the theoretical methods.

The thermal noise method calibrates the spring constant via the equipartition theorem, equation (2.4), but this requires calibration of the cantilever deflection and various correction factors for cantilever geometry must be taken into account.[78,94–96] The thermal noise method has been extended to include the second flexural mode but the absolute cantilever deflection must be known.[49] The measurement of cantilever deflection can be performed using laser Doppler vibrometry to eliminate the need to calibrate the photodiode sensitivity in optical detection methods.[97]

The Cleveland method[98] monitors the change in the resonance frequency of beams due to the addition of masses to the cantilever, but risks damage to the cantilever each time a mass is attached to it. Furthermore, the exact added mass must be known. Particles which are assumed to be spherical and with density similar to the bulk are used to calculate the

attached mass. The radius of each particle is measured by microscopy and it is this which introduces the largest source of uncertainty. The effect on the resonance frequency is equally observable through the removal of mass, as demonstrated in ref.[99] where mass was removed by focused ion beam milling, or by the addition of mass via a thin film, for example addition of a layer of gold.[100]

The Sader method[85, 101] calculates the spring constant based on knowledge of the cantilever's resonance frequency, Q-factor, plan view dimensions and information of how it interacts with a surrounding gas via the 'hydrodynamic' function. Once this function has been determined the method is one of the simplest. However, the hydrodynamic function must be determined experimentally over a reasonably large range of Reynolds numbers by variation of gas pressures, densities, or viscosities, which is not straightforward. Some vacuum equipment is ideally required to vary the pressure surrounding the cantilever. The Q-factors need to be determined from Lorentzian fits of the resonance peaks, care must be taken for particularly high Q's.[102] The Sader method is subject to uncertainties of up to 10-20%,[48, 103] possibly larger if the cantilever is shaped non-ideally.

Recently an interlaboratory test of cantilever calibration for AFM force spectroscopy compared the thermal noise and Sader methods.[104] The study included two types of V-shaped and a rectangular cantilever, all cantilevers were relatively soft (nominal k_s=0.01-0.03 N/m). The cantilevers were tested on a variety of AFM systems, the two methods generally showed good agreement. Ref.[49] found good agreement between the Sader and thermal noise methods for the first flexural mode but

large disagreements for the second flexural mode, in large part due to the assumption of an ideal (tipless) rectangular cantilever in the Sader method.

4.2.4 Comparison of Existing Techniques for Flexural Eigenmode Calibration

Tables 4.1 and 4.2 show a summary of some of the methods for the calibration of the fundamental flexural mode of microcantilevers. Some of the data is taken from ref.[48] where more details, particularly relating to the dimensional methods can be found.

Method	Summary/Requirements	Deflection?*	Uncertainty	Advantages	Disadvantages
Static					
Reference cantilever[91]	Monitor bending of cantilever in contact with one of known k_s.	Yes	10-30%	Simple principle	Need to calibrate reference cantilever. Potential for damage.
Nanoindenter[92]	Bend cantilever against nanoindenter.	Yes	8%	Relatively accurate	Stiff cantilevers (k_s >1 N/m) only. Potential for damage.
Theoretical					
Dimensional[48]	Measurement of dimensions, analytical equations.	No	11%	Non-destructive	Need t and E.
FEA[93]	Use dimensions, materials properties in simulation.	No	10%	Non-destructive	Assumes knowledge of cantilever properties, software requirement.

Table 4.1: *Summary of some of the notable static and theoretical methods for the calibration of the flexural modes of microcantilevers.*

**Denotes whether the scheme requires determination of cantilever (or nanoindenter) displacement.*

Method	Summary/Requirements	Deflection?*	Uncertainty	Advantages	Disadvantages
Dynamic					
Thermal noise[78, 94–96]	Collect resonance peak, use equipartition theorem.	Yes	5-20%	Non-destructive	Correction factors for geometry and area under resonance peak required.
Cleveland[98, 99]	Attach mass, monitor change of ω_n.	No	3-10%	Simple measurement	Uncertainty over the added mass and its position. Potential for damage.
Sader[85, 101]	Uses l, w along with Q-factor, ω_1 and hydrodynamic function.	No	Up to 10-20%[48, 103]	Simple to use	Hydrodynamic function must first be determined for each cantilever shape.

Table 4.2: *Summary of some of the notable dynamic methods for the calibration of the flexural modes of microcantilevers. *Denotes whether the scheme requires determination of cantilever displacement.*

4.2.5 Conclusions

There are a plethora of methods in existence to calibrate the spring constant of the fundamental flexural mode, all have their advantages and disadvantages. The vast majority are unsuitable for extension to the higher modes of oscillation. The higher eigenmodes are becoming an area of significant interest for the community. Some of the AFM manufacturers incorporate the ability to monitor the second flexural mode into their microscopes but without calibration only limited information is gained. The development of new methods of calibration, particularly those involving the ability to calibrate the higher modes, is therefore of interest.

4.3 Fluid Dynamics

A quantitative understanding of the fluid flow from a parallel plate microchannel and interactions with the cantilever is important to the calibration method described in this chapter along with the one that follows. Hence a short review of the most relevant areas of the field of fluid dynamics is given here.

The governing equation of fluid dynamics is the Navier-Stokes equation,[105]

$$\rho \frac{D\mathbf{v}}{Dt} = -\nabla p + \eta \nabla^2 \mathbf{v} + \rho g, \tag{4.2}$$

essentially it is Newton's second law for fluids and takes account of pressure gradients (∇p), fluid stress (through viscosity η) and gravitational acceleration (g).[105] The latter is often neglected and shall be in this document as its magnitude is small in comparison with the other terms

in equation (4.2). $\mathbf{v}$ is the velocity vector, $\frac{D\mathbf{v}}{Dt} = \frac{\partial \mathbf{v}}{\partial t} + \mathbf{v} \cdot \nabla$ is the total differential of $\mathbf{v}$ and ρ is the density of the fluid. Equation (4.2) can be solved analytically for only a limited number of special cases.[106] In practical situations one must either simplify the equation by identifying different regimes through dimensionless numbers, or solve the equation numerically by simulation.

The Reynolds number, Re, is used in fluid dynamics to give an indication of the stability of a fluid flow.[106] It is derived from the Navier-Stokes equations by taking the ratio of inertial and viscous forces,

$$Re = \frac{va}{\nu} \tag{4.3}$$

where v is a characteristic fluid velocity, a is a typical length scale of the system and ν is the kinematic viscosity of the fluid. The kinematic viscosity is related to the dynamic viscosity, η, by $\nu = \eta/\rho$. The Reynolds number can be used to indicate different regimes of fluid flow, for example low Reynolds numbers imply that viscosity is important. For $Re \gtrsim 10^4$ the flow becomes turbulent, this rule being the same on both macroscopic and microfluidic scales.[107]

The Knudsen number, $Kn = \lambda/a$, where λ is the molecular mean free path in a fluid can be used to judge whether macroscopic parameters are appropriate. The mean free path in a gas is given by $\lambda = \frac{k_B T}{\sqrt{2}\pi d^2 p}$ where d is the diameter of the fluid particles, T is the temperature, k_B is Boltzmann's constant, and p is the pressure. For Knudsen numbers of $Kn \lesssim 10^{-2}$ macroscopic concepts may be used.[108]

There are various flow regimes concerned with different approximations, in this document only Poiseuille flow will be discussed. Poiseuille

flow describes the flow between two plates (at $y = 0$, $y = h$) along the x-axis driven by a pressure gradient dp/dx. The speed of the fluid can be found to vary as

$$v = -\frac{1}{2\nu}\frac{dp}{dx}y(y-h) \tag{4.4}$$

across the channel.[109] The velocity profile of the flow is illustrated in figure 4.1. One important concept in fluid dynamics is the no-slip bound-

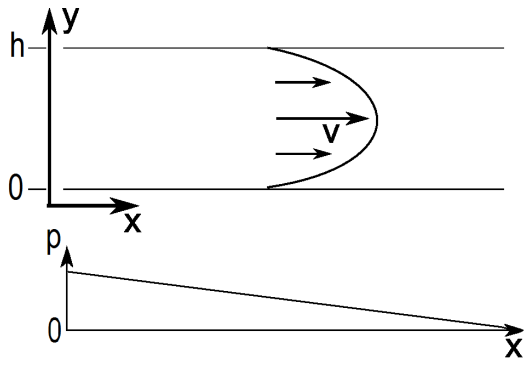

Figure 4.1: *Hyperbolic velocity profile of fluid flow between two parallel plates driven by a pressure gradient.*

ary condition, which states that the fluid velocity must match the velocity of a solid body at its surface. Note that equation (4.4) satisfies the no-slip condition at $y = 0$ and $y = h$. In an ideal channel of constant height the pressure drops linearly to zero over the channel length, driving the fluid flow at a steady velocity given by

$$v = \frac{h^2\Delta p}{8\eta L}, \tag{4.5}$$

where Δp is the pressure difference between that at the start and end of the channel.

4.4 Calibration of the Flexural Spring Constants; Theory and Simulation

In this and the following sections a new method for the calibration of the flexural spring constants of all modes of microcantilever beams is described.

Cantilever structures display a series of natural flexural vibration modes $u_n(x)$ with frequencies ω_n.[1, 62] Due to the stiffness of the structures an internal bending moment $M_n(x) = EI(x)u_n''(x)$ is associated with each mode n,[62] where E is Young's modulus, $I(x)$ is the area moment of inertia, and $u_n''(x)$ is the second derivative of the n^{th} flexural mode $u_n(x)$ with respect to x.

The method to determine the flexural spring constants is based on measuring changes in the flexural resonance frequencies, ω_n, of a cantilever by applying small forces parallel to the cantilever length as shown schematically in figure 4.2. The cantilever is shown bent near its maxi-

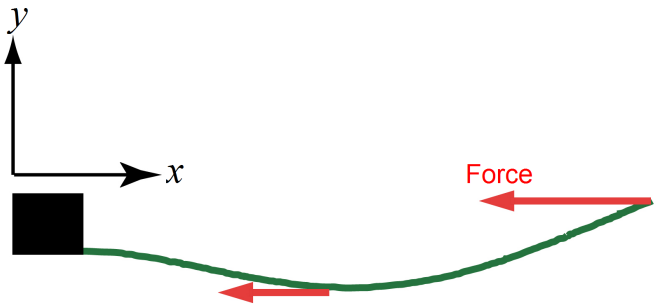

Figure 4.2: *Schematic side view of an oscillating cantilever with two example forces, denoted by the (red) arrows, acting parallel to the cantilever length.*

mum amplitude in the second flexural mode. It is clear from the figure that the applied forces will possess a component which acts to bend the

cantilever into a further bent shape. The applied force will have this effect throughout the cantilever's cycle of oscillation, with the exception of where the cantilever is perfectly straight. The forces will act to lower the resonance frequency of the cantilever.

The external forces applied along the x-direction of the cantilever create an additional moment in the n^{th} mode,

$$\Delta M_n(x) = \int_x^l \zeta_x(x')(u_n(x') - u_n(x))dx' + (u_n(l) - u_n(x))F_{end}, \tag{4.6}$$

when the cantilever is oscillating. $\zeta_x(x)$ is a force per unit length applied in the x-direction and F_{end} is the force applied to any face at the free end of the cantilever. If the modal shapes are normalised according to equation (2.17) the total energy in the n^{th} mode is given by[44]

$$U_n = \frac{1}{2}\int_0^l \frac{M_n^2(x)}{EI(x)}dx = \frac{1}{2}\omega_n^2. \tag{4.7}$$

Therefore, the additional bending moment $\Delta M_n(x)$ induces a frequency shift $\Delta(\omega_n^2)$

$$\Delta(\omega_n^2) \approx 2\int_0^l u_n''(x)\Delta M_n(x)dx \tag{4.8}$$

provided $\Delta M_n << M_n$ and hence $u_n(x)$ is not significantly changed by the external forces. The eigenmodes are normalised such that the energy of each mode calculated using $u_n(x)$ corresponds to the modal energy of the real cantilever such that the correct $\Delta(\omega_n^2)$ may be calculated. If the material's properties and sizes of the cantilever are known, then the normalisation can proceed via equation (2.17). However, some of the properties are not necessarily well known hence the present calibration method aims to elucidate the correct normalisation of the modeshapes such that the spring constants may be calculated via equation (2.22). For

point loads equation (2.22) can be re-written in a much simpler form,

$$k_n = \frac{\omega_n^2}{u_n^2(x)}. \tag{4.9}$$

The flexural spring constants at the position of the tip can be calculated by setting $u_n(x)$ to its value at the position of the tip.

The external forces are caused by a fluid flow from a microchannel, with the flow direction parallel to the long axis of the cantilever as displayed in figure 4.3.[43, 86]

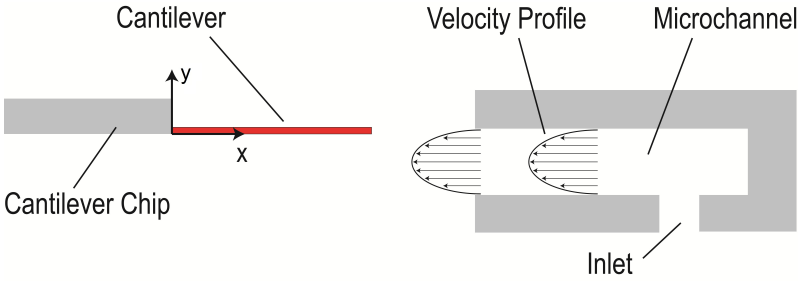

Figure 4.3: *Schematic of the experimental setup. A poiseuille flow profile is established in the microchannel which interacts with the cantilever.*

To provide information about the interaction of the flow from the channel with the cantilever, finite element method simulations were performed with the open-source, multi-physics software package of Elmer.[55] Meshes required in the simulations were created with Gmsh.[56] The mesh independence of the results was confirmed by further mesh refinement. The simulations were used to calculate the forces applied to the static cantilever by the fluid flow, based on which the resonance frequency shifts were predicted according to equation (4.8).

4.5 Calibration of the Flexural Spring Constants; Experimental Details

Experiments were performed with a commercial AFM Explorer system (ThermoMicroscopes, Sunnyvale, CA, USA). A homemade smooth parallel plate microchannel fixed on the sample stage of the AFM was positioned such that fluid flow from its exit interacted with the cantilever as illustrated in figure 4.3. Pressure differences, Δp, were applied to the microchannel to drive the flow, establishing stable Poiseuille velocity profiles.[43] Nitrogen gas was used as the working fluid due to its low cost, high purity and well known properties. In this work, a channel of height H=150 μm and length L=4.5 mm was used. The channel was mounted on micro-positioners (MDE262M, Elliott Scientific, UK) and aligned such that the cantilever was level with the top of the channel and with its free end 100 μm from the channel exit.

The maximum pressure applied to the channel in our experiments was $\approx$1.4 kPa causing a velocity of nitrogen in the channel mid-line of about 50 m/s.[86] The highest Reynolds number for our setup did not exceed 500. In combination with the Knudsen number in the channel, which is about 0.0005, this Reynolds number corresponds to the laminar regime of incompressible flow.[110]

To test the method several commercially available tipless rectangular silicon cantilevers (90-350 μm nominal length, 0.03-1.75 N/m nominal spring constant, Al backside coating, R-A to R-F, Mikromasch[47]) and two V-shaped silicon nitride cantilevers (V-D, SNL, Bruker: 205 μm nominal length, 0.06 N/m nominal spring constant, Au backside coating, and

V-B, Veeco: 196 μm nominal length, 0.12 N/m nominal spring constant, Au backside coating[76]) were investigated. All rectangular cantilevers had a nominal width of 35 $\pm$ 3 μm, cantilever V-B had a nominal leg width of 41 $\pm$ 5 μm and V-D had a nominal leg width of 20 $\pm$ 5 μm. The term 'nominal' refers to the guideline values as provided by the manufacturer.

The plan view dimensions, for use in conjunction with the Sader method, of all microcantilevers were determined with an Olympus optical microscope. In addition, electron microscope images were obtained for the V-shaped cantilevers to obtain accurate geometric data for their tip dimensions and position.

Power spectral densities of thermal noise spectra were recorded with an external interface with an accessible frequency range of $\approx$700 kHz (National Instruments, USB-6251) as a function of fluid velocity. Resonance frequency values, Q-factors, and peak areas for each mode were monitored during measurement with a homewritten LabVIEW^{TM} routine by fitting Lorentzian curves to the resonance peaks similar to the procedure described in ref.[78]. All resonance frequencies were monitored simultaneously. The resonant frequency values are based on the average of 50 individual spectra.

4.6 Calibration of the Flexural Spring Constants; Results

4.6.1 Cantilever Dimensions

The plan view dimensions of the tested cantilevers are reported in table 4.3. The base width of V-B was found to be 201.4 $\pm$ 2.3 μm and that of V-D was 203.5 $\pm$ 1.9 μm. The opening angle between the legs

Cantilever	l_{nom} (μm)	l_{exp} (μm)	w_{exp} (μm)
R-A	110 ± 5	95.5 ± 2.7	28.4 ± 0.4
R-B	90 ± 5	76.3 ± 2.3	28.9 ± 0.4
R-C	130 ± 5	114.7 ± 3.1	31.1 ± 0.4
R-D	300 ± 5	295.0 ± 3.6	31.2 ± 0.3
R-E	350 ± 5	339.5 ± 3.9	31.4 ± 0.3
R-F	250 ± 5	240.1 ± 3.5	30.3 ± 0.2
V-B	196 ± 5	187.4 ± 0.4	39.8 ± 0.4
V-D	205 ± 5	204.0 ± 2.1	25.5 ± 1.0

Table 4.3: *Dimensions of the cantilevers investigated, l_{nom} is the nominal length, l_{exp} and w_{exp} are the cantilever dimensions as determined by optical microscopy. Experimental uncertainties were derived from the standard deviation of at least three measurements.*

at the free end of the V-shaped cantilevers was therefore 56.5 °± 0.7 ° for V-B and 53.0 °± 0.6 ° for V-D. For V-B and V-D the length was taken perpendicular to the end of the chip, the leg width was taken parallel to the cantilever base.

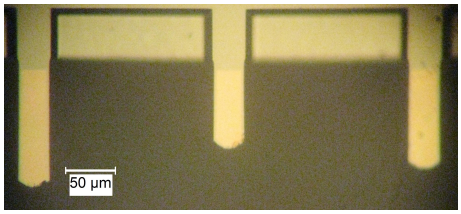

Figure 4.4: *Optical microscopy image of the plan view of cantilevers R-C, R-B and R-A (left to right of image).*

Significant discrepancies from the manufacturer's dimensions were found, particularly in relation to the width of all the rectangular can-

tilevers and the lengths of R-A, R-B and R-C. As can be seen in figure 4.4, all rectangular cantilevers had a reasonably rounded or picketed free end. The quoted cantilever lengths were taken to be at the extreme of the structure.

4.6.2 Forces Exerted by the Fluid Flow

Figure 4.5 shows the fluid flow around a rectangular cantilever from a simulation with Elmer. In this geometry the flow from the channel tends

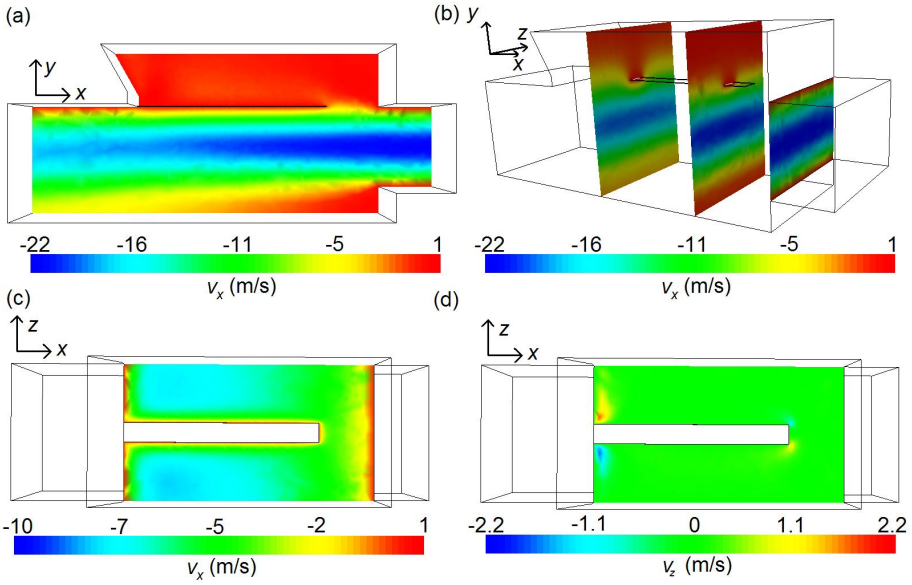

Figure 4.5: *Simulated course of the fluid flow around a rectangular cantilever which is level with the top of a microchannel and 100 µm from its exit. The fluid flow is from right to left in each subfigure and the colour scale represents the fluid speed. (a) Slice through the centre of the cantilever, speed along the cantilever long axis. (b) Slices perpendicular to the flow direction, speed along the cantilever long axis. (c) and (d) are plan views showing a slice at the same altitude as the cantilever with velocity in the x and z directions respectively.*

to stay beneath the cantilever as shown by figure 4.5(a), albeit with some flow around the sides of the cantilever in the vertical (y) direction,

figure 4.5(b). The speed of the flow in the y-direction is enhanced by the presence of the chip where the fluid essentially has to choose whether to flow over or under the chip. Figure 4.5(d) shows that the gas only moves appreciably in the z-direction at the start and end of the cantilever. It also confirms the validity of the volume of fluid simulated to either side of the cantilever. Note that the boundaries at low and high z in this figure (the sides of the domain) are subject to a no flux condition; the velocity parallel to the boundaries is unrestricted but no fluid may pass through them.

Fluidic force distributions for a range of flow velocities were determined with Elmer for all cantilevers studied. Figure 4.6(a) shows some of the forces per unit length exerted by the fluid flow along the cantilever length on cantilevers R-E and R-C at different fluid speeds as obtained from simulation. It was found that the force distributions for all rectan-

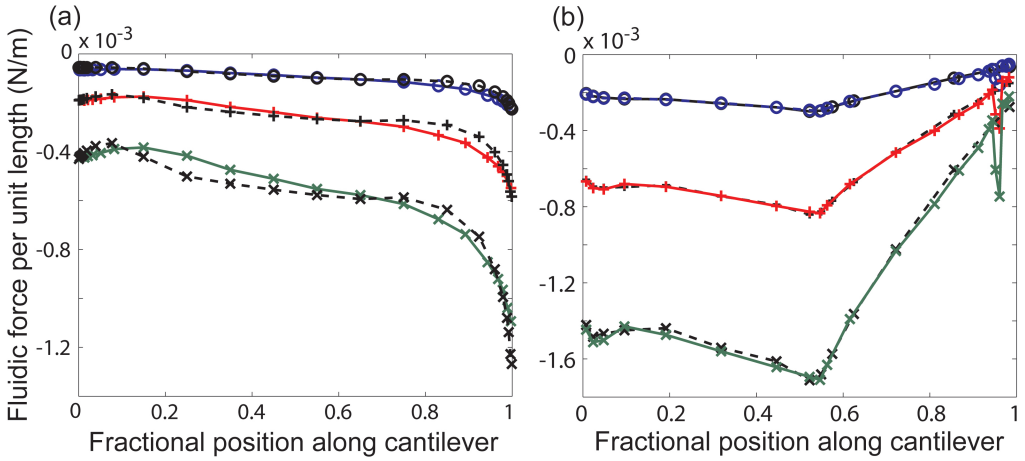

Figure 4.6: *Fluidic forces per unit length exerted by the flow from the microchannel depending on the fractional position along the cantilever length: (a) forces on cantilevers R-E (solid lines) and R-C (dashed lines) at fluid speeds of 6 (∘), 15 (+), and 30 m/s (×), and (b) tipped V-B (solid lines) and tipless V-B (dashed lines) at fluid speeds of 6 (∘), 15 (+), and 30 m/s (×).*

gular cantilevers were remarkably similar for fixed fluid speed values if normalised to the cantilever length and hence a single force distribution (that of R-E) was used in the calculations. Figure 4.6(b) displays the fluidic force for cantilever V-B with and without a tip. The influence of the tip is clearly visible as a sharp peak in the force at the tip position. There is only a very small deviation in the fluidic force on the rest of the cantilever.

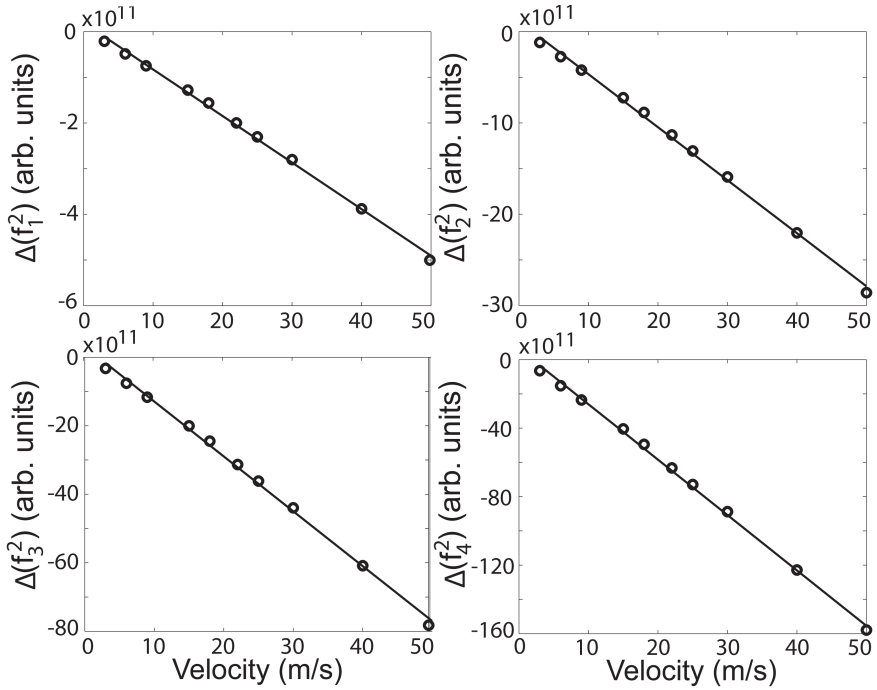

Figure 4.7: *Calculated frequency shifts (open circles) for the first four flexural modes of a rectangular cantilever. The predicted shifts are well described by a linear fit (solid lines).*

4.6.3 Frequency Shifts

Theoretical frequency shifts $\Delta(f_n^2) = \Delta(\omega_n^2)/4\pi^2$ as a function of fluid velocity were determined with homewritten MATLAB routines according to equation (4.8), using modal shapes $u_n(x)$ whose maximum deflection at

the free end was set to one. The simulated forces applied to the cantilever (from simulations in the previous section) were used to calculate a value for the frequency shift at each velocity simulated. Results are displayed in figure 4.7.

Figure 4.8 displays experimentally obtained power spectral densities of the resonance peaks at zero fluid velocity for cantilever R-E along with the resonance frequencies and the Q-factors. The Q-factors of all

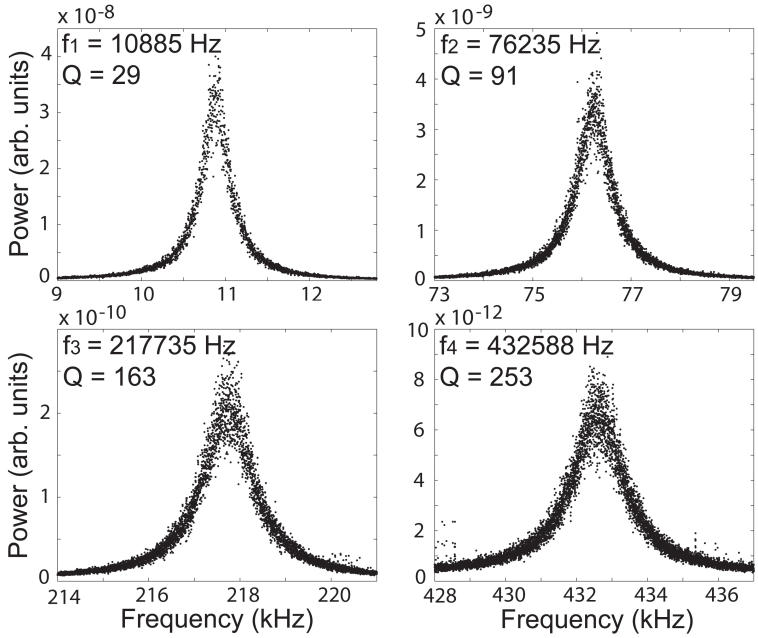

Figure 4.8: *Thermal noise power spectral densities of the first four flexural modes obtained for cantilever R-E.*

resonant peaks showed fluctuations below 5-10% for different fluid speeds. Q-factors can therefore be considered as constant and independent of fluid velocity.

Similar plots to those shown in figure 4.7 can be made with the experimental data. Figure 4.9 shows typical frequency shifts as a function of fluid velocity obtained experimentally for the first four modes of flexu-

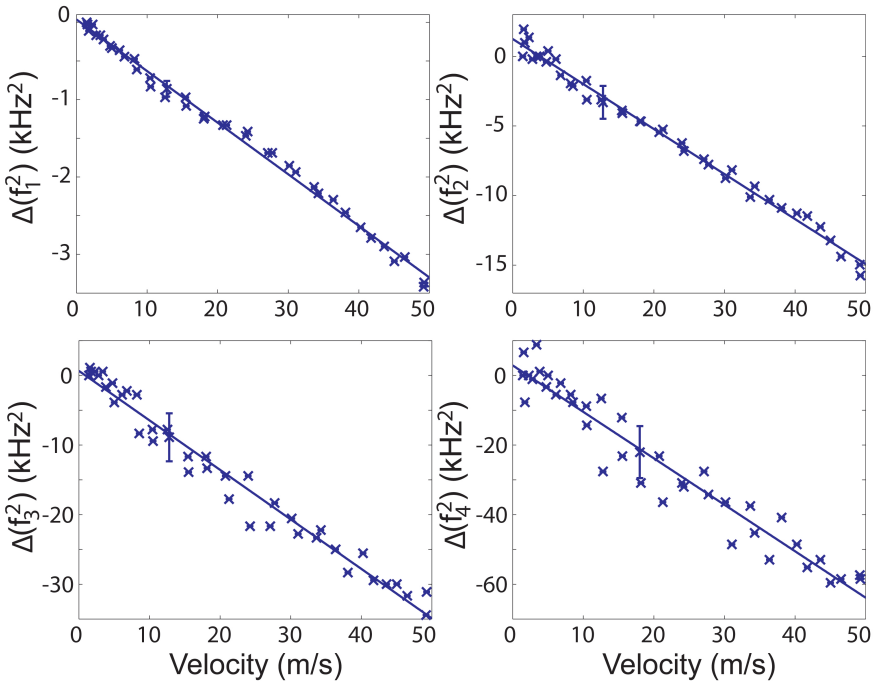

Figure 4.9: *Experimental data (×) and fit (solid line) of the frequency shifts as a function of fluid velocity for the first four flexural modes of cantilever R-E. Error bars are based on the experimentally determined standard deviation of 15 measurements of the resonant frequency values at a constant fluid speed. Only one error bar for each mode is shown for clarity.*

ral vibration of cantilever R-E. The frequency shift $\Delta(f_n^2)$ decreases with mode number n as expected. This behavior was observed for all cantilevers investigated.

The external moments $\Delta M_n(x)$ exerted by the fluidic forces are proportional to $u_n(x)$. This allows for the determination of the normalisation factor for $u_n(x)$ (via equation (4.8)) by fitting a single parameter such that the calculated frequency shifts match those determined experimentally. The resulting normalised eigenmode shapes then comply with equation (2.17). It is this normalisation which effectively accounts for non-ideality of the cantilever of interest.

To calculate the spring constants of a real cantilever the experimental and simulated frequency shifts are obtained for the real and ideal cantilevers, from which the amplitude of each of the eigenmodes may be calibrated. Subsequently the spring constants, k_n, can be determined by equation (4.9) for a single spring, or equation (2.22) for the general case of a distribution of springs, using the normalised modeshape and the resonance frequency of each eigenmode.

4.6.4 Spring Constants

Spring constants of rectangular cantilevers were determined using both the method described above and the method of Sader[85] for all accessible flexural modes of oscillation. Values for the Sader method were determined using the experimental dimensions shown in table 4.3 along with the online calibrator for rectangular cantilevers.[111] Results are summarized in tables 4.4 and 4.5. For some of the cantilevers presented here only the fundamental or first few modes were within the frequency range accessible with our equipment. The major source of uncertainty in our calibration comes from the fit of the experimental frequency shifts. Confidence bands based on one standard deviation were used in the calculation of the uncertainty. The resulting uncertainty in the spring constants is typically in the 5-10% range. Careful positioning of the cantilever eliminates the potential for related systematic errors in our calibration scheme.

Cantilever	k_1 (N/m)				k_2 (N/m)		
	Nominal	This work	Sader	δ_1 (%)	This work	Sader	δ_2 (%)
R-A	0.95	0.914(44)	1.02	-11.6	-	-	-
R-B	1.75	1.99(21)	2.08	-4.5	-	-	-
R-C	0.6	0.650(44)	0.653	-0.5	31.1(4.1)	32.2	-3.5
R-D	0.05	0.0644(39)	0.0611	5.1	2.79(11)	2.47	11.5
R-E	0.03	0.0428(20)	0.0398	7.0	2.10(6)	1.82	13.8
R-F	0.08	0.104(6)	0.0979	5.9	4.61(23)	3.96	14.1
V-B	0.12	0.117(6)	-	-	1.47(32)	-	-
V-D	0.06	0.0602(47)	-	-	1.25(4)	-	-

Table 4.4: *Spring constants for the first two modes of a variety of microcantilever sensors. The uncertainty in the last digits is given by the quantity in brackets.* δ_n *is the percentage difference between the spring constant derived by the method described in this work and that from the Sader method.*

4.7 Calibration of the Flexural Spring Constants; Discussion

Our results based on the simulations and the experiments indicate that forces and hence frequency shifts depend linearly on the fluid speed. This can be explained by the fact that the force experienced by the cantilevers is in our setup essentially a drag force exerted by the fluid, which according to Stokes' law increases linearly with speed.[105]

Cantilever	k_3 (N/m)			k_4 (N/m)		
	This work	Sader	δ_3 (%)	This work	Sader	δ_4 (%)
R-D	22.6(1.6)	14.5	35.6	88.5(13.7)	79.7	-8.4
R-E	17.1(6)	14.9	13.1	67.5(4.3)	63.8	5.5
R-F	37.3(3.8)	33.3	10.7	-	-	-
V-B	6.37(1.3)	-	-	18.3(3.7)	-	-
V-D	6.86(40)	-	-	17.3(1.4)	-	-

Table 4.5: *Spring constants of the third and fourth modes of a variety of microcantilever sensors. The uncertainty in the last digits is given by the quantity in brackets. δ_n is the percentage difference between the spring constant derived by the method described in this work and that from the Sader method.*

4.7.1 Influence of Cantilever Thickness

The thickness of a cantilever is crucial for its resulting stiffness,[78] but it is much more difficult to determine it accurately than the plan view area dimensions. Calibration methods which do not rely on the exact knowledge of the cantilever thickness are therefore desirable. A 25% deviation of the cantilever thickness from its nominal value results in a factor of two difference in its flexural spring constant since the latter scales with the third power of the thickness.[62]

Figure 4.10 shows the effect of using the fluidic forces calculated for a 1 μm thick cantilever in the calculation of the frequency shifts for a 1.25 μm thick cantilever along with the calculated shifts from simulations run with a cantilever thickness of 1.25 μm. The different gradients shown in the figure give the error associated with using the predicted frequency shifts from the 1 μm cantilever for a cantilever of differing thickness. Our

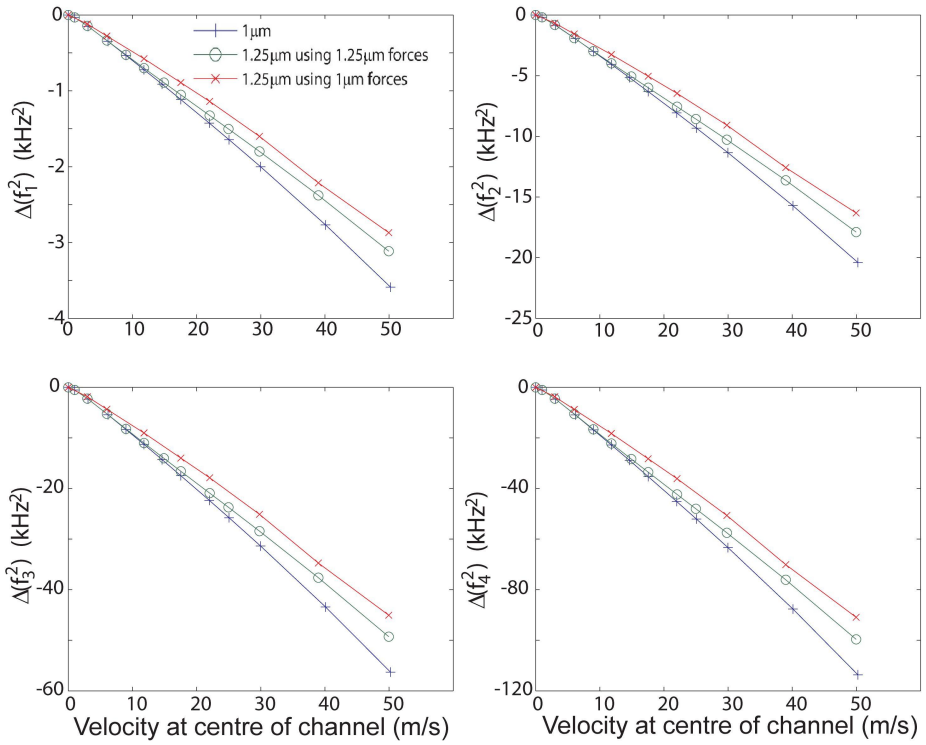

Figure 4.10: *The effect of using the 'wrong' cantilever thickness in the calculation of the frequency shifts for the first four flexural modes of a rectangular cantilever. The shifts for a 1 μm cantilever calculated using the simulated forces for a 1 μm cantilever have been added for reference and replicate the frequency shifts shown in figure 4.7. The frequency shifts have been scaled by assumed material properties for a silicon cantilever[59] such that the shifts are those expected for an ideal cantilever of type R-E.*

modeling indicates that with the method presented here a 25% change in the thickness of the cantilever leads to a deviation of the determined spring constant value of less than ≈6% compared to the correct value because of the small contribution of the cantilever side walls to the overall fluidic force. Therefore the exact cantilever thickness is much less crucial in obtaining accurate results here.

4.7.2 Cantilever Dimensions and Shape

All experimentally determined spring constants of the first flexural modes fall within the range given by the manufacturers, despite some of the dimensions of the cantilevers being outside the nominal range. The fundamental spring constants obtained for R-A, R-B, V-B and V-D are within experimental error of the manufacturer's nominal value. Generally, the fundamental spring constants calibrated using our method are in agreement with the values derived by the Sader method. No uncertainties are quoted for the Sader method but previous studies have found that an error of up to 10-20% is reasonable.[48, 103] For the higher modes (n >1) larger deviations are observed between the calibration methods. This is expected as approximations are made in the Sader method which mean that it becomes progressively less accurate as the mode number increases.[112, 113]

In other studies[48, 103] it has been found that the Sader method underestimates the spring constant due to a rounding-off of the free end or from a non-rectangular cross section of real cantilevers. Our results for R-D, R-E and R-F tend to support this, with the fundamental spring constants determined by our method being 5-7% higher than those determined by the Sader method. In addition, the Sader method requires that $l >> w >> t$, a condition that may not be totally satisfied by cantilevers R-A, R-B, and R-C which potentially explains why the Sader method appears to underestimate the spring constants for these cantilevers. The applicable lower limit of l/w is unclear, the minimum tested by Sader was $l/w = 3.3$, for which calibration by the Sader method showed reasonable agreement with other calibration methods.[85] It has also been

noted that the errors associated with the Sader method increase with decreasing l/w as well as for increasing mode number.[113] The deviation between the two methods was greatest for R-A which has $l/w \approx$3.1, however a smaller discrepancy was obtained for R-B despite its slightly lower l/w of 2.6. A recently published scheme[114] for the exctraction of the fundamental flexural spring constant from a thermal noise based method observed a similar disagreement with the Sader method for a cantilever with l/w=3.2. Very close agreement between the two methods is evident for cantilever R-C.

The deviations of the rectangular cantilevers from the ideal shape do not have a significant effect on our calibration procedure due to the small relative influence that it has on the fluidic force per unit length. All non-ideality in the cantilever dimension is effectively encoded in the modal shapes $u_n(x)$, the experimentally determined normalisation factors and the measured resonance frequencies of the cantilever.

Only one set of theoretical frequency shifts was required in case of rectangular cantilevers as the simulated forces and modeshapes could simply be normalised by the nominal cantilever length. The deviation in the spring constants in comparison with using the correct force distributions (see figure 4.6) was below 6% for all rectangular cantilevers studied. This can be seen qualitatively in figure 4.11 which displays the frequency shifts calculated for R-C using the force profiles from simulations of R-C and R-E. The difference in the gradients of the two traces gives the error in the spring constant of using the profile of R-E in the calculation of the spring constant of R-C.

The exact shape of the chip in the proximity of the fixed end of the

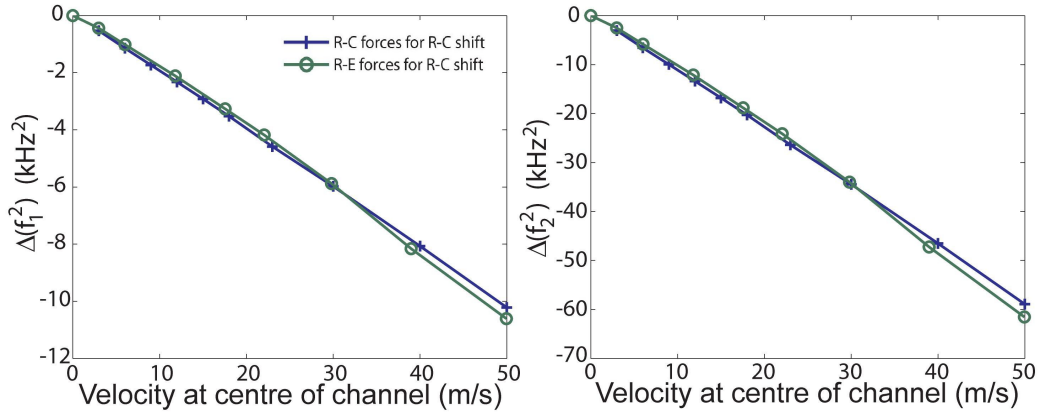

Figure 4.11: *Theoretical frequency shifts for the first two modes of cantilever R-C when using the simulated fluid force profile for R-C ('+') and for the scaled fluidic force profile from R-E ('∘'). The frequency shifts have been scaled by assumed material properties for a silicon cantilever[59] such that the shifts are those expected for an ideal cantilever R-C.*

cantilever (steep face versus slanted face) was found not to be crucial. There was no significant difference in the overall resulting fluidic force and hence frequency shifts. This can be explained by the fluid flowing mainly at the bottom side of the cantilever and the relatively small fluidic force at the fixed end due to the decreasing fluid speed with increasing distance from the channel exit (see figure 4.6).

4.7.3 Influence of a Tip

It has been reported that the higher modal shapes can be significantly affected by the tip mass if it amounts to several percent of the total cantilever mass.[89] For the tipped V-shaped cantilevers studied the mass of the tip contributed less than 0.9% to the total mass of V-D and less than 0.5% to the mass of V-B. The determination of the modal shapes as described in ref.[44] indicated that there is no significant influence on

the mode shapes compared to the same cantilevers without the tip, but it could be taken into account if required.

The simulations further demonstrated that the effect of the tip on the fluidic forces experienced by the cantilevers is small. Figure 4.6(b) shows the fluidic force per unit length for various speeds experienced by cantilever V-B with and without the tip. A pyramidal tip of around 3.5×3.5 μm^2 at the base and 4 μm in height based on electron microscopy images was included in some of the simulations. These dimension appear to be typical for this type of cantilever in view of the manufacturer's specifications. The presence of the tip has an influence on the fluidic forces but it is a small effect resulting in an increase of the magnitude of the frequency shifts of all modes of V-B of less than 3% and less than 1% in case of V-D. For other types of cantilevers and tips it might have a bigger influence. To minimize the contribution from the tip to the fluidic force the top of the cantilever could also be aligned with the bottom of the channel such that the drag force is mainly exerted over the tipless top side of the cantilever.

Note that with the normalised mode shapes and resonant frequencies known the spring constants for any force distribution and any tip position along the cantilever can be determined.[44] In particular any tip setback can easily be taken into account using equation (4.9).

4.7.4 Influence of a Colloidal Probe

In many force sensing applications, or in measurement of surface viscoelastic properties, a colloidal probe is attached to the cantilever or its tip. Most colloidal probes are spherical beads of $\approx$1 to 30 μm diameter

which are used to provide an easily described area of contact with a surface.[10] They can be useful in determining the viscoelastic properties of soft samples, for example biological cells, where use of a sharp tip could damage the sample.

As with the addition of a tip to the cantilever, the presence of a colloidal probe may modify the modal shapes of a cantilever due to its mass along with increasing the forces applied to the cantilever in the calibration method described here. Furthermore, colloidal probes are attached to the cantilever surface by use of some form of glue which has the potential to create a surface stress distribution adding to the cantilevers effective spring constant. The latter effect is expected to be negligibly small as the contact area between microsphere and cantilever should be sufficiently small.

A range of microsphere sizes and materials appear in the literature,[10] however this discussion will restrict itself to an example of a 5 μm diameter silicon microsphere similar to that used in ref.[115]. A microsphere of this dimension increases the mass of cantilever R-E by $\approx$0.6% meaning that it does not affect the modeshapes unduly.[89] However, it is easy to see that a microsphere of just double this size, 10 μm in diameter, amounts to around 4.8% of the mass of R-E and would probably have to be included in the determination of the modeshapes. A non-homogeneous mass distribution can be taken account of using the equations in section 2.5.

The fluidic forces applied to cantilever R-E with the 5 μm diameter colloidal probe attached were simulated. From the forces predicted frequency shifts were calculated based on modeshapes unaffected by the

mass of the colloidal probe. Figure 4.12 shows these frequency shifts along with those for cantilever R-E. The shifts for the cantilever with the

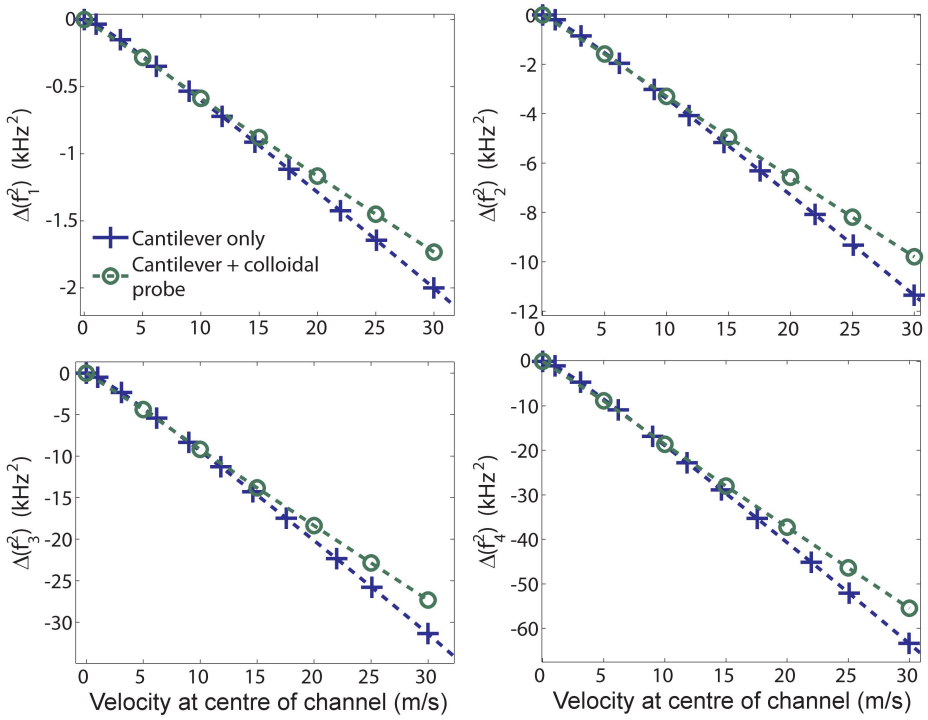

Figure 4.12: *Theoretical frequency shifts of the first four flexural modes for a 350 μm rectangular cantilever showing the effect due to the addition of a colloidal probe. Data for the cantilever with the colloidal probe shown by '∘', for comparison the cantilever without the probe is shown by '+'. Frequency shifts were calculated using assumed materials properties for silicon.[59]*

colloidal probe are actually smaller which seems counter-intuitive. The origin is that although there is a spike in force at the position of the microsphere, its presence affects the fluid flow sufficiently for the forces to be lower on the bottom surface of the cantilever in the vicinity of the probe. The error associated with using the simulated shifts for the cantilever without colloidal probe in the determination of the spring constants of the first four flexural modes compared with a cantilever with

this colloidal probe are in the range of 11 to 13%. Therefore for many colloidal probes their mass and effect on fluidic forces have to be accounted for if spring constants are to be determined accurately with this method. The treatment of the fluidic forces is straightforward, the effect of the probe is to cause a spike in force at its position (similar to that caused by the tip in figure 4.6) and to slightly lower the forces elsewhere on the bottom surface of the cantilever. Effects related to the mass of a colloidal probe can be incorporated into a non-homogeneous mass distribution in the determination of the modeshapes.

4.7.5 Cantilever Positioning

The positioning of the cantilever relative to the fluid flow is important, although we found that in the current setup it is rather insensitive to a deviation of several micrometres in the direction of the channel height and tens of micrometres in the distance from the exit.

In the position that we used in our experiments the fluid flow exerts a force parallel to the cantilever length but the cantilever does not distort the main flow from the channel significantly because it is placed in the outer regions of the fluid stream. In fact, the cantilever can be considered to be an extension of the channel with flow essentially on one side only.

Simulations were performed to quantify the sensitivity of the calibration scheme to an error in the positioning of the cantilever with respect to the exit of the channel. Figure 4.13 defines the terms h' and d used to describe the positioning of the cantilever relative to the microchannel exit. Figure 4.14 shows the simulated frequency shifts for cantilever R-E for a variety of distances, d, from the exit of the microchannel. Fig-

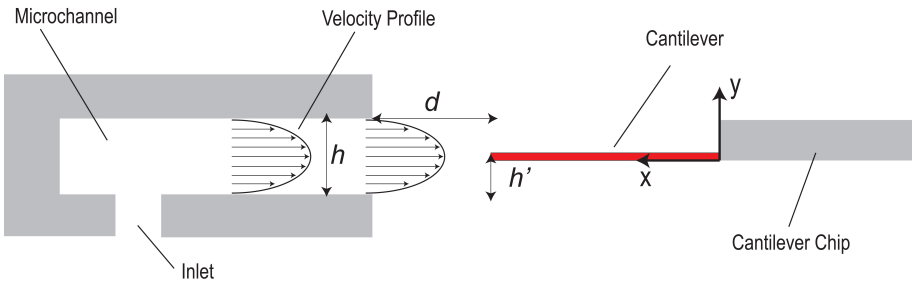

Figure 4.13: *Schematic of the experimental setup defining the symbols representing the distance and cantilever altitude relative to the exit of the microchannel.*

ure 4.14 shows that there is minimal difference in the frequency shifts for a wide range of d. Thus any error in positioning in this direction results in only a small deviation in the calculated spring constants. The difference between the shallowest and steepest gradient in each of the plots in figure 4.14 is less than 7%, for the comparison between 80 and 120 μm distances from the exit. The deviation in frequency shifts resulting from misalignment translates into an identical percentage error in the determined spring constant. As such the method is relatively insensitive to an error in positioning of tens of micrometres in the distance from the exit. Experimentally this distance was set using micropositioners with an accuracy of better than 10 μm, hence the experimental positioning should be sufficiently accurate to obtain representative spring constants.

The positioning of the cantilever relative to the channel height is also important and simulations have been run to quantify the associated potential errors. The predicted frequency shifts for a range of cantilever heights, h', are shown in figure 4.15. Again the gradient of each trace relative to that for the desired position (e.g. h'=150 μm) give an estimate for the error associated with inaccurate positioning of the cantilever. The percentage differences in the predicted spring constant of the first mode

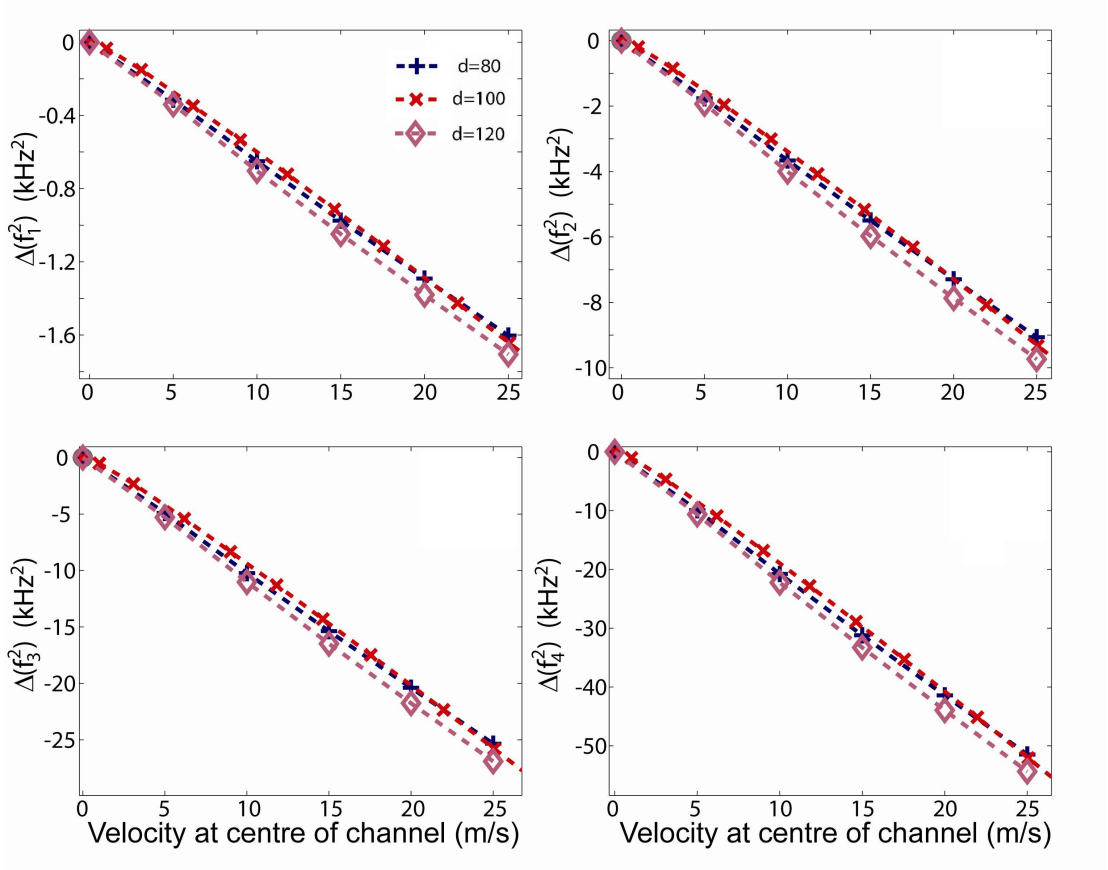

Figure 4.14: *Calculated frequency shifts for the first four flexural modes of rectangular cantilever R-E for different distances from the exit of the microchannel. The frequency shifts have been scaled by assumed material properties for a silicon cantilever[59] such that the shifts are those expected for an ideal cantilever.*

would vary by 12%, 2%, 13% and 22% for incorrect experimental alignment to the positions h'=145 μm, h'=148 μm, h'=152 μm and h'=155 μm respectively.

As one would expect, the frequency shifts increase if the cantilever is moved towards the centre of the channel due to the higher speeds and forces experienced there. The shifts also begin to show a non-linear relationship with respect to the speed at the centre of the channel. Such effects shall be discussed in more detail in section 4.8.2. As the cantilever

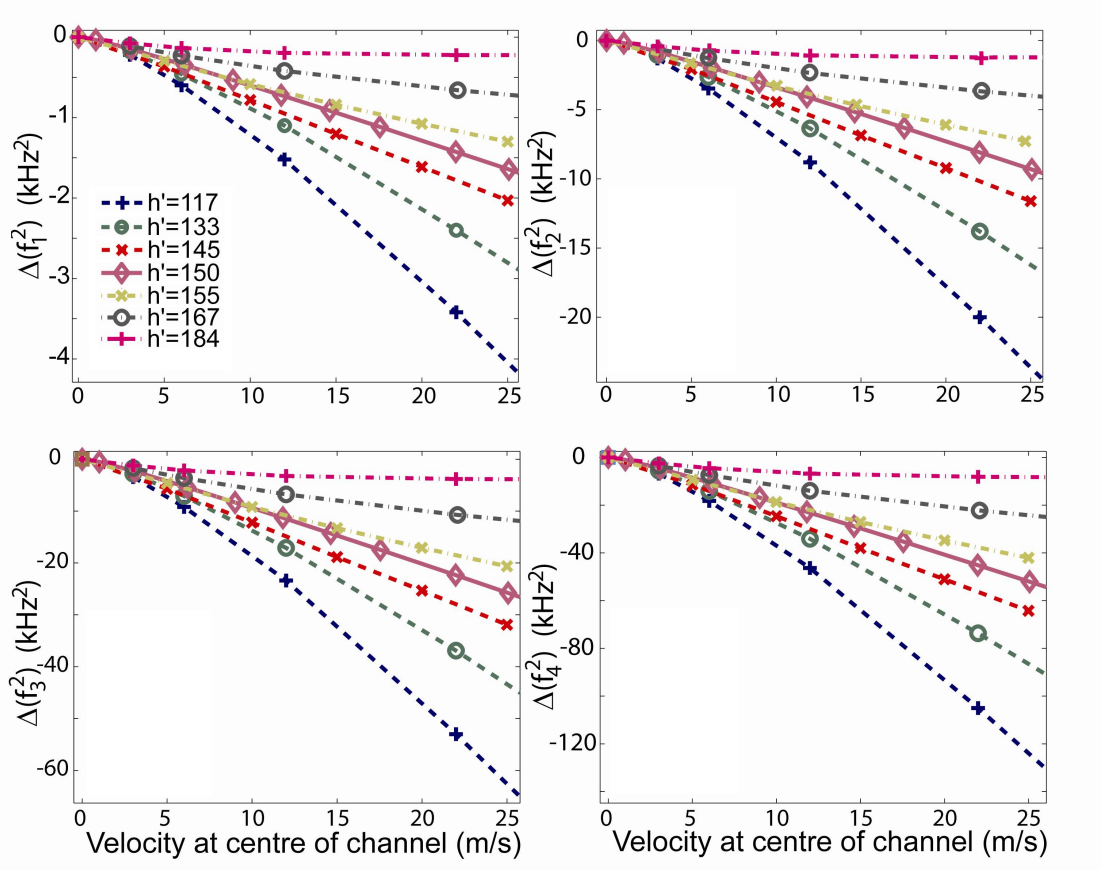

Figure 4.15: *Calculated frequency shifts for the first four flexural modes of rectangular cantilever R-E showing the effect of changing the relative height, h′. h′=150 μm represents the case where the cantilever is level with the top of the channel. The frequency shifts have been scaled by assumed material properties for a silicon cantilever[59] such that the shifts are those expected for an ideal cantilever.*

is moved higher than level with the top of the channel, then it moves into lower speed flows, experiences smaller forces and therefore smaller shifts are expected.

For the case where the cantilever is 34 μm above the top of the microchannel the frequency shifts are initially negative but level off and even increase with fluid speed. The flow from the microchannel is essentially a jet, the width of the jet increases with distance from the exit and

hence it can still affect the cantilever when it is a considerable distance above the exit. However, the jet narrows with increasing fluid velocity such that for higher velocities the main part of the flow no longer interacts with the cantilever. Fluid near the stream is entrained to move with it and some circulation is induced. It is this circulation which gives rise to a fluid flow in the opposite direction along the cantilever and causes an increase in resonance frequency for the higher speeds in the h'=184 μm position.

The relative angle between cantilever and channel also has the potential to play a role in determining the frequency shifts. In the present experimental setup it is impossible to quantitatively determine the relative angle. However, the flexural frequency shifts were observed to be largely unaffected by variation of the angle of up to at least $\pm 5\,^{\circ}$. The decrease in the force along the cantilever for a misaligned case can be considered to be due to a scaling of the aligned force by the cosine of the angle. Since this is close to one for a small angle, the reduction in the force along the x-direction is also sufficiently small to not affect the frequency shifts unduly. Anecdotal evidence from experimental experience suggests that the calibration of the V-shaped cantilevers were more sensitive to angular misalignment than rectangular cantilevers.

The bending moment calculation can also be executed for the torsional modes of oscillation. The predicted contribution to a torsional frequency shift due to the parallel forces is very small, hardly larger than random noise, due to the low amplitude of the modes. Experimentally, the frequency shifts of the torsional eigenmodes were found to depend critically upon the angle between cantilever and channel. Even a small

misalignment was found to enhance the frequency shift of the torsional modes for all cantilevers. It was found that torsional frequency shifts are linked to the static bending of the cantilever, which itself depends on the forces applied in the y-direction and hence upon the angle of misalignment. The lack of a torsional frequency shift when the cantilever is aligned parallel to a fluid flow could be used as an indication of the relative angle between cantilever and channel. The explanation for the link between static bending and torsional frequency shifts shall become clear during chapter 5.

The fluidic forces exerted normal to the cantilever length cause some static bending but do not change the oscillation frequencies if the bending is small enough and the cantilever behaves like an ideal beam.[60] The highest static bending observed occurred for R-E and was roughly 500 nm at the free end for the highest fluid speed of ≈50 m/s based on experiment. The theoretical calculation with the normal fluidic force distribution from the modeling gave a similar value.[44, 54]

4.8 Other Geometries

Since the cantilever chip is positioned on the AFM head, and the channel upon micropositioners on the AFM's sample stage then any relative position and orientation between cantilever and channel is easy to test. The case where $h' = h$, in the previous section, was found to be the easiest to accurately achieve in the current experimental context. It was also reasonably insensitive to experimental errors in the distance of the cantilever from the channel exit and in the height from the bottom of the channel.

A range of positions were investigated and some of the cases where the fluid flow was predominantly along the cantilevers length are presented here. A discussion of experiments where the fluid flow is predominantly perpendicular to the cantilever follows the conclusion of this chapter.

4.8.1 Channel Dimensions

Any channel height or length could be used provided that the fluid flow from its exit is steady and laminar. Channel heights tested ranged from 50 to 300 μm. From that range the motivation for using one channel over another is primarily one of experimental convenience. The accuracy of positioning the cantilever is the same for all channels hence the fractional error in positioning is smaller for deeper channels. However, by equation (4.5), a channel of greater height will produce higher flow speeds (for a given pressure) which are more likely to become turbulent. Of course, a lower pressure and/or a longer channel could be used but in the existing set up the channel length is inflexible and a pressure range as large as practical is desirable to reduce any errors relating to the pressure sensor. For these reasons a 150 μm channel was generally used.

All channels tested produced the same trends in the frequency shifts for the same relative cantilever/channel geometry. The flexural frequency shifts are still all negative but the quantitative behaviour depends upon the channel height.

4.8.2 Cantilever Positioned Near the Centre of the Channel

If the cantilever was placed at the middle of the channel height, i.e. in the middle of the parabolic fluid velocity profile ($h' = h/2$), a large variation

in the normalisation factors extracted for the different individual modes was observed. As a consequence, there was also a significant deviation from the spring constant values reported in tables 4.4 and 4.5.

The fluidic forces and frequency shifts increased as the cantilever was moved towards the centre of the channel. The profile of the fluid flow can be simulated, a slice through one such simulation for a V-shaped cantilever with $h' = h/2$ is shown in figure 4.16. The effect on the

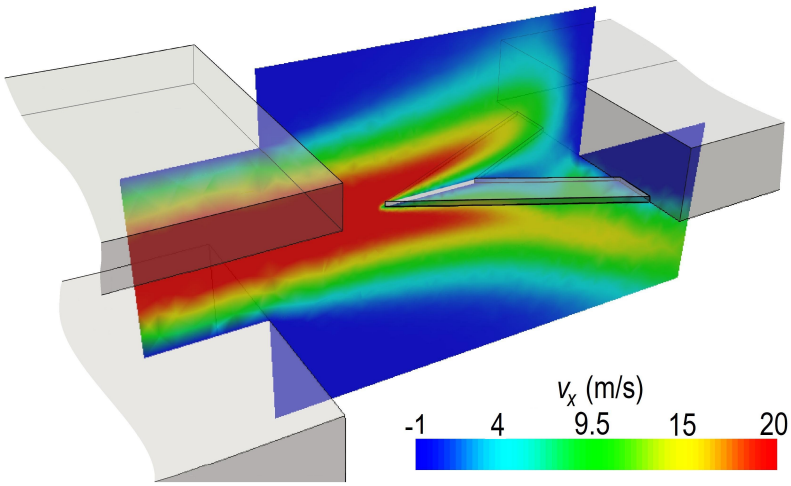

Figure 4.16: *Simulated fluidic flow around an ideal V-shaped cantilever positioned near the centre of the microchannel.*

fluidic forces can be seen in figure 4.17. The magnitude of the forces around the cantilever increases as the cantilever is moved towards the centre of the channel. Given that for $h' = h$ the majority of the flow is on one side of the cantilever it is perhaps surprising that larger forces in the y-direction, and therefore greater static bending, are predicted for cantilevers closer to the centre of the channel. The origin of this is the effect of the cantilever chip in changing the direction of the flow, particularly near to the fixed end. The chip plays an increasing role as h' is lowered towards and past $h/2$.

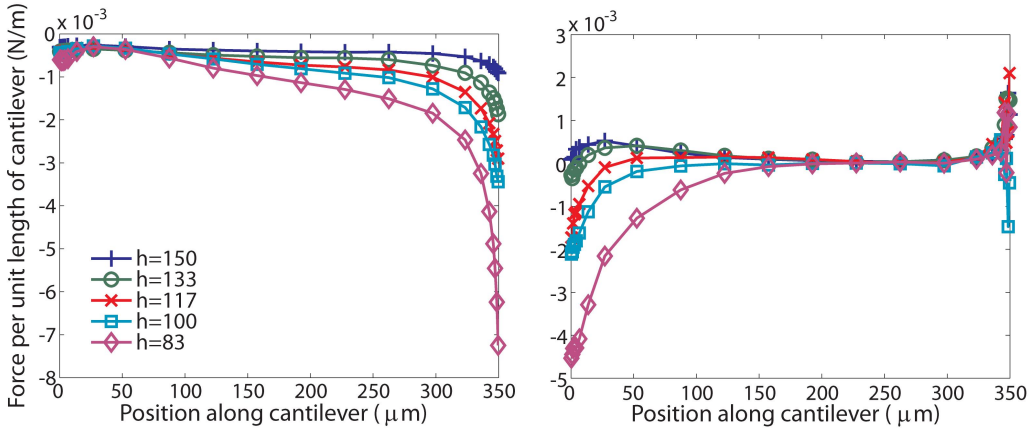

Figure 4.17: *Simulated fluidic forces in the (a) x- and (b) y-directions for a variety of h' for cantilever R-E. h' are given in micrometres and are relative to a 150 μm channel height. In all cases the velocity at the centre of the Poiseuille was 22 m/s.*

The deviation of the determined k_n (relative to those determined for $h' = h$ in tables 4.4 and 4.5) can be elucidated from figure 4.18. For the case where $h' = 83$ μm the cantilever is positioned close to the centre of the 150 μm high channel. Note that the reason for discussion of $h' = 83$ μm as opposed to the exact centre, $h' = 75$ μm, is experimental in origin and is related to the process by which h' is set experimentally. It can be observed in the figure that for the first eigenmode the experimentally obtained frequency shift is roughly two and a half times larger than that predicted from the simulated fluidic forces and the bending moment theory (equation (4.8)). The discrepancy between simulation and experiment is reduced for the second mode, largely eliminated for the third mode and eliminated for the fourth mode. In some cases it even appears that the experimentally obtained shifts for the third and fourth modes are less than predicted whilst the first and second are larger.

The deviation in the normalisation factors is likely to be an indication of a coupling of the flexural modes to the flow from the microchannel

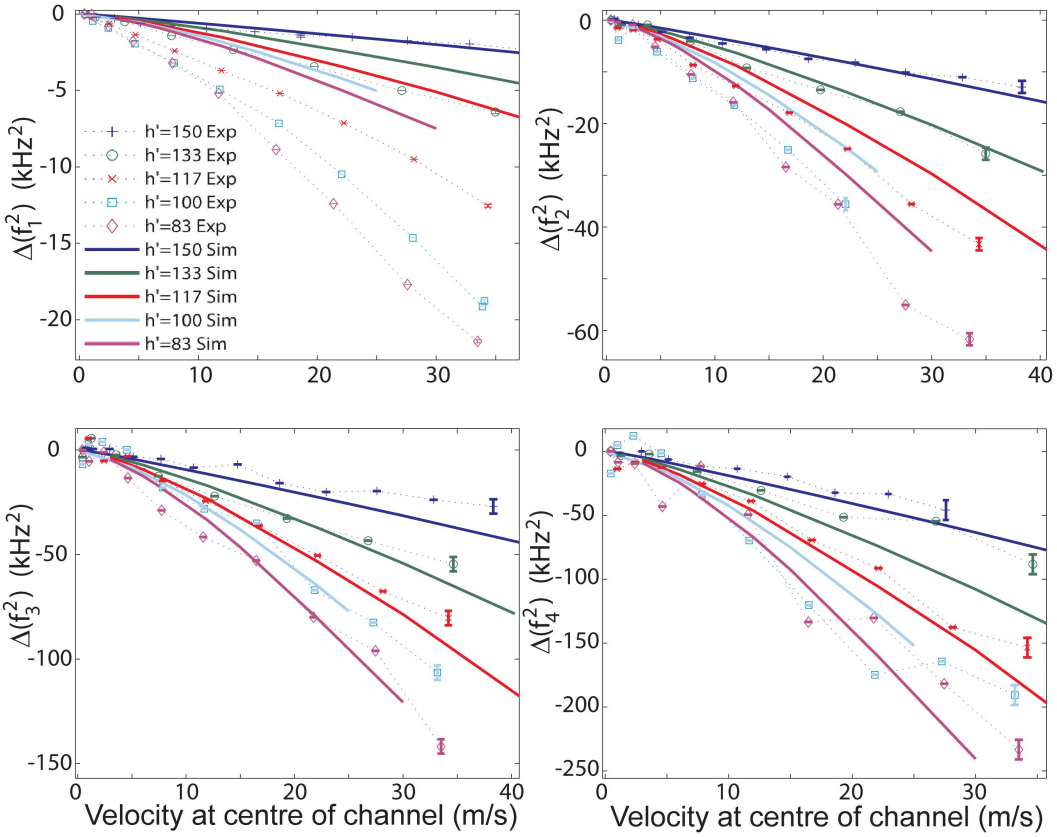

Figure 4.18: *Calculated and experimentally obtained frequency shifts for the first four flexural modes of rectangular cantilever R-E for a range of values of h′. The frequency shifts have been scaled by assumed material properties for a silicon cantilever[59] such that the shifts are those expected for an ideal cantilever.*

where the strength of the coupling depends on the mode. It appears that the calculations we performed with a static cantilever do not describe this situation adequately, and the steady-state approximation is no longer applicable. This is supported by studies of macroscopic flexible cantilevered plates positioned in the middle of a channel flow, see for example refs.[116, 117]. A small number of transient simulations were run in an attempt to replicate the effect but all were unsuccessful, which may be related to the fact that Elmer is not the software package of choice for describing the transition to turbulence.

4.8.3 Extension of the Lower Surface of the Microchannel

One simple variation of the setup shown in figure 4.13 is to have the bottom surface of the microchannel extending beneath the cantilever and the chip. Such a setup was tested and behaviour similar to that shown in the previous sections was observed. All frequency shifts were negative and their magnitude showed a roughly linear relationship with fluid speed. However, the forces perpendicular to the cantilever were enhanced resulting in a larger static bending of the cantilever for a given fluid speed. Assuming perfect alignment of the lower surface of the channel and the chip, a second microchannel up to several millimetres in length beneath the chip with the same height as the primary microchannel is created, see figure 4.19. Hence, there is a large 'impedance' to hinder the path of

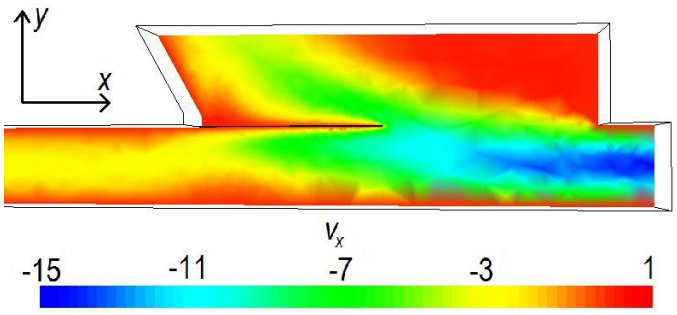

Figure 4.19: *Slice through a 3-D simulation showing the fluid speed in the x-direction (along the cantilever length). The surface making up the bottom of the microchannel extends beneath the cantilever and chip, a secondary microchannel is formed underneath the chip to the left side of the image.*

fluid through this secondary microchannel and a significant amount of the fluid from the primary microchannel must flow up around the cantilever and along the (near) vertical face of the cantilever chip, see figure 4.19. This upward flow imparts forces upon the cantilever causing a greater

bending than for the case where there is no wall beneath the cantilever. This explanation was experimentally reinforced by blocking off the secondary microchannel underneath the chip. The observed frequency shifts were similar to when the secondary microchannel was open.

One interesting property of this setup is that the frequency shifts were unaffected by changing the distance between the exit of the channel and the free end of the cantilever. Indeed, moving the free end of a 300 μm long rectangular cantilever from around 50 μm to 400 μm from the exit resulted in an increase of the magnitude of the frequency shift of the fundamental flexural mode of around 10%. Conversely, the frequency shift of the second mode dropped by around 5% and that of the third mode increased by less than 5%. The origin of this effect is probably linked to the effect described above: as the flow is encouraged away from the bottom wall around the cantilever higher speed fluid originating from the centre of the Poiseuille profile can interact with the cantilever. The speed of the flow drops off away from the microchannel exit, but as the cantilever is moved further away from the exit the position of maximum flow speed moves towards the free end of the cantilever. As forces on the free end of the cantilever have the greatest influence on the frequency shifts (see equation (4.6)), moving the position of maximum parallel fluid force towards the free end of the cantilever offsets the effect of the reduced fluid speed with distance from the microchannel exit.

4.8.4 Parallel Fluid Flow with the Cantilever as an Extension of the Channel

The initial work of this project was as an extension to the ideas detailed in refs.[43,86] where the lower surface of the cantilever chip formed the top of the microchannel and the fluid moved parallel to the cantilever length but from the fixed to the free end. The theory previously derived and applied for this setup was found to be inappropriate as it relied upon the fluid speed being constant underneath the cantilever. It also assumed that the Poiseuille profile continued underneath the cantilever as if it were an extension of the channel. However, simulations of the fluid flow showed that it flowed around the sides of the cantilever within a short distance from the exit. The effect is the same as depicted in figure 4.19, where the flow moves away from the wall beneath the cantilever.

For these tests the cantilever chip was positioned atop the microchannel to form its upper surface. Hence the chip was not mounted on the AFM head but on the sample stage. It was therefore difficult to position the system such that the cantilevers were in focus and modes higher than the second flexural were almost impossible to observe due to low signals.

Positive frequency shifts were observed, as might be expected if the effect is due to an additional bending moment associated with the parallel forces. In this case the forces are in the opposite direction along the cantilever to those described earlier in this chapter. Frequency shifts were gathered for the first two flexural resonance modes, with the third occasionally observable. Higher modes were not observed as routinely due to the fact that the chip was not mounted upon the AFM head and hence perfect alignment of the laser upon the cantilever was generally

unachievable.

Additionally, experimentally obtained frequency shifts were thought to depend quite sensitively upon the angle with which the chip was placed upon the microchannel, which was difficult to judge and entirely unrepeatable. The fluidic forces imparted on the cantilever were simulated and used to calculate predicted frequency shifts based on the bending moment calculation of equation (4.6). The calculated shifts for cantilevers parallel to the lower surface of the channel were found to be significantly smaller than those determined experimentally. However, the predicted frequency shifts showed large variations with the angle between cantilever and microchannel, adding weight to experimental experience.

Hence, the parallel flow arrangement with the cantilever as an extension of the channel was abandoned in favour of having the chip mounted on the AFM head and a self-contained channel positioned upon the AFM sample stage as described earlier in section 4.5.

4.9 Failed Theoretical Attempts to Explain the Observed Frequency Shifts

Historically speaking, in terms of a PhD study, the experimental part of the method always worked well, i.e. reasonably reproducible and measurable frequency shifts were observed for a range of geometries and cantilevers. There were many attempts to reproduce the observations in a theoretical manner with the assistance of the simulations. Some of the theories that were developed but ultimately discarded are discussed in this section. The majority were unsuitable due to predictions of fre-

quency shifts of insufficient magnitude.

Any object or body which experiences a force gradient will have its natural vibrations modified accordingly. The way that a force varies around the surface of an object can be described as an additional external spring, or distribution of springs acting upon it.[44] Related treatments can be found in many areas of physics, for example the chemical bonds between the carbon and oxygen atoms of a molecule of CO_2 amount to an electrical potential the gradient of which is the force with which the atoms are held in position. The bonds can then be viewed as a spring and the whole system as a simple harmonic oscillator with some characteristic mass and used to explain the molecule's responses in vibrational spectroscopy.

Various theoretical treatments were based on this philosophy and simulations were executed to determine the forces or static pressures acting on the cantilever in a certain position. The gradient at the cantilever surface then has to be determined. Two examples of the pressure gradients at the cantilever surface are shown in figure 4.20. MATLAB routines were written to determine the pressure and velocity along a given line profile and were used to record the variation of the pressure near to the cantilever surface. To obtain accurate information, and the largest gradients, very fine meshes were required at large computational cost. The mesh used for the data in figure 4.20 had around 359 000 points as opposed to around 8 200 in most of the simulations, it was therefore run on the computational cluster in St Andrews.[‖] The mesh was biased such that it was much finer around the surface of the cantilever which allows

[‖]Simulation run by Dr Herbert Fruchtl using files prepared by the author.

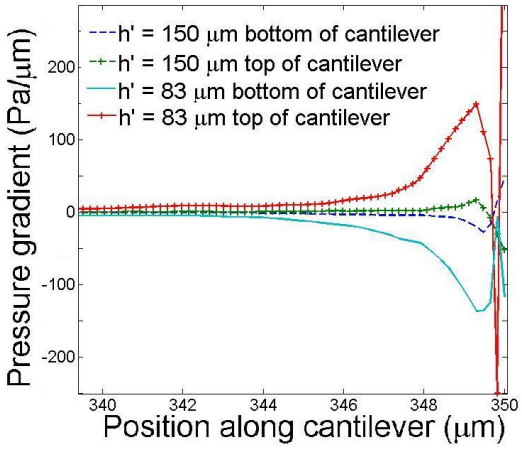

Figure 4.20: *Simulated pressure gradients on the top and bottom surfaces of a cantilever.*

the gradient in figure 4.20 to be calculated between the pressure at the cantilever surface and that 0.6 μm from the surface.

Figure 4.20 shows data for the geometry of $h = 150$ μm, with $h' = 150$ and 83 μm. The pressure gradient and therefore external spring distribution is zero over the majority of the cantilever and is only significant near the free end. If, when the cantilever moves, it experiences an increase in force then the pressure gradient is positive and the effect of the gradient will be to force the cantilever back towards its equilibrium position thus increasing its resonance frequency. The gradients from $x \approx 340$ μm to ≈ 349.7 μm in the figure all act to increase the resonance frequency, in contrast to the experimental observations. The predicted gradient changes sign very close to the cantilever free end and this gradient indicates a negative frequency shift. The two effects compete and the calculated frequency shifts cannot account for those obtained experimentally, generally being of the correct sign but having a magnitude of up to a few percent of the experimentally observed values.

Another method by which a pressure gradient was calculated was by running two simulations with the cantilever in slightly different positions and comparing the pressures experienced by the surfaces of the structure. To obtain the gradient the cantilever in the second simulation was moved up or down by 0.5-5 μm, rotated by an angle, or constructed in a bent shape. Again, no calculated gradient possessed sufficient magnitude to account for the experimentally observed frequency shifts.

A different set of treatments of the experimental shifts centred around the potential effects of the fluidic forces along the x-axis in compression of the cantilever. If the forces compressing a beam reach the Euler critical load, $EI\pi^2/l^2$, then the beam will buckle.[1] For cantilever R-E the critical load is 4.46×10^{-5} N applied to the free end which is much larger than the integral of the distributed forces applied to the cantilever, 3.5×10^{-7} N, calculated from the 50 m/s simulation where the cantilever is level with the top of a 150 μm channel. Therefore the cantilever beam is in no danger of buckling. The resonance frequency for a beam with a given load, F_{end} on the free end can be calculated using[1] $\omega_n = \frac{an^2\pi^2}{l^2}\sqrt{1-\frac{F_{end}l^2}{n^2EI\pi^2}}$ where $a^2 = EI/wt\rho_c$ which predicts a frequency shift in the fundamental mode of 0.09 kHz^2 if the entire force acting on the cantilever in the x-direction (3.5×10^{-7} N) were applied on the free end. Hence, it is clear that such an effect cannot account for the experimentally observed frequency shifts which were around 3.4 kHz^2 for this velocity.

4.10 Further Work

The origin of the extra frequency shift described in section 4.8.2 where $h' \approx h/2$ is still unknown. As alluded to, it is probably an artifact of

the higher fluid speeds that the cantilever is placed in potentially leading to turbulence. A full treatment of the fluid-structure interaction may be required. These two things expose the weaknesses in the modeling software, indeed turbulence along with coupled (fluid flow and structural mechanics) simulations with Elmer have proved inconclusive in the limited cases where reasonable results were achieved. A related possibility is that the cantilever begins flapping like a flag and the observed frequency shifts indicate a transition to turbulence. Whilst the flapping of flags or plates has been studied by many groups,[116, 117] very little work has been done on the initial stages of the transition to turbulence. It may be that monitoring of the resonance frequencies of a body give an indication of the processes occurring during such transitions.

For the successful calibration of the spring constants, the eigenmode shapes are normalised using experimental data. Such a process essentially amounts to calculating EI for any particular cantilever, and therefore opens the possibility of using the fluid flow method to determine Young's modulus or moment of inertia of microstructures.

In the calibration scheme described the average of the normalisation factors determined from all modes was used, an operation which assumes that the cantilever is of the expected shape, of consistent thickness, and homogeneous density and elastic modulus. If any of these conditions are not satisfied then the normalisation factors may vary from mode to mode and it may be possible to use them to determine how a particular property of the cantilever (e.g. thickness) varies along its length as different modes show greater sensitivities in different areas, in proportion to the magnitude of $u_n(x)''$.

The calibration could be performed in any fluid, in this work nitrogen gas was used due to convenience and cost considerations. Executing the calibration using a liquid could be of interest if the cantilever is going to be used in such environments.

4.11 Conclusions

The method described here allows for the simultaneous calibration of all flexural modes of microcantilever sensors. Spring constants can be determined with an uncertainty of 5-10% and are in agreement with the Sader method for the first flexural mode of rectangular cantilevers. The higher flexural modes in particular have been successfully calibrated. Due to the use of a fluid flow the approach does not pose any risk of damaging the cantilever or any tip via contact with a surface. It also does not require the accurate determination of cantilever thickness, nor does it require calibration of the cantilever deflection. The calibration can potentially be done in any fluid: liquid or gas and in low Q environments.

In principle any cantilever may be calibrated using the approach described, provided the fluidic forces per unit length and mode shapes $u_n(x)$ are known. The former can be simply found by CFD simulations of the static cantilever exposed to the fluid flow and the latter by the Ritz method.

5 Torsional Calibration of Microcantilevers

This chapter is partially based upon a patent application, ref.[118]. The patent submitted being in relation to the method described in this chapter.

5.1 Introduction

As described in sections 2.3.2 and 2.4.2 cantilevers may oscillate in a twisting, or torsional, manner. A method to calibrate the spring constants of these modes is described in this chapter. The terms torsional and lateral are often used interchangeably in the AFM literature as the application of a lateral force to a cantilever tip results in a lateral bending and the torque associated with application of the force on the tip acts to induce a torsional twisting of the cantilever.[51] Lateral forces on the tip may be applied in AFM scans as the tip is moved over the surface of interest. The static torsional spring constant, $k_{s,t}$, and static lateral spring constant $k_{s,l}$ are related to one another via[51]

$$k_{s,l} = \frac{k_{s,t}}{H^2}, \tag{5.1}$$

where H is the tip height. The lateral forces can be used in one of the many sub-fields of AFM, friction force microscopy (FFM).[119] In dynamic or tapping AFM applications the monitoring of a torsional eigenfrequency could be used to probe the variation of forces parallel to the surface.[88] The oscillation of the cantilever means that the end of the tip sweeps a trace across the sample. Frequency shifts of the torsional eigenmodes could also be used as independent sensors, in similar applications to those described in chapter 3.

Recent advances in AFM technology relating to hammerhead or T-shaped cantilevers where the plan view area is shaped like a capital 'T', fixed at the narrow end, with the tip displaced to one side at the free end. The availability of these types of cantilevers lends a greater relevance to the calibration of torsional modes. One use of these cantilevers is in the 'torsional tapping' method[20] where the tip offset gives a tapping effect to torsional oscillations. An advantage of such methods is that a cantilever of relatively low flexural spring constant can be used to reduce tip or sample damage while collecting the image with a torsional mode with a higher spring constant and larger Q-factor.

As with the use of the flexural modes, to obtain accurate quantitative information from torsional modes the associated spring constants must be known. Likewise, variations of cantilever cross section and material properties mean that individual cantilevers should be calibrated before use.

5.2 Existing Calibration Methods

There are a range of existing methods to calculate the torsional rigidity of microcantilevers, although there are fewer than for the flexural eigenmodes. The calibration methods may be divided into three categories: static, dynamic and theoretical. In the former the stationary bending of the cantilever is monitored. The static methods all require some physical contact with the cantilever or tip and therefore involve a high risk of damage.[51] At present, the majority of the torsional calibration methods are static in origin. Dynamic calibration methods monitor the cantilevers resonance frequency as a pathway to analysing the interaction of the can-

tilever with external influences or its response to masses attached to the cantilever. Finally, the general category of theoretical methods uses dimensions of the cantilever, and assumptions about its material properties and/or finite element simulations to determine the spring constant.

5.2.1 Static Methods

The bulk of current methods for the calibration of the lateral spring constant are based upon static methods. Generally they require calibration of the detection system for the lateral cantilever deflection and have a high risk of damaging the cantilever or tip. In some of these methods a colloidal probe is attached to the cantilever.[51]

A range of methods monitor the static twist of the cantilever produced as a result of a lateral force on a tip or colloidal probe. The lateral force can be applied by moving the tip sideways into a step on a calibration grid[120,121] or by scanning the cantilever up and down slopes of a known angle on a calibration sample.[122–125] Similar methods exist where the tip of the cantilever to be calibrated is brought into contact with another calibrated cantilever which is rotated through 90 degrees with respect to the first. Therefore a flexural deformation of the second cantilever causes a torque and hence a torsional twist of the first cantilever.[126] The flexural deformation of the reference cantilever is used to calculate the force applied to the tip, and therefore the bending moment causing the observed twist of the cantilever of interest, finally allowing calculation of $k_{s,t}$.

Other static methods apply loads to the cantilever surface. This can be done by pressing one side of the cantilever into a hard surface and

measuring the resulting cantilever twist,[127] particularly for hammerhead cantilevers.[128] These methods have the advantage that they do not require a model of the friction between the tip and the surface, unlike many of the above, however they still involve considerable risk of damage to the cantilever itself.

Methods to calibrate cantilevers by means of optics also exist. Whilst these methods do not risk damage to the cantilever they are sensitive to detector non-linearity.[129–131] Others rely on the tilting of a calibration surface, which should have the same reflectivity as the cantilever surface.[132–134]

5.2.2 Theoretical Methods

The torsional spring constants of a cantilever may be calculated theoretically. Analytical equations can be used along with knowledge of the cantilever dimensions and elastic properties via[93, 135]

$$k_{s,t} = \frac{wt^3G}{3l} \tag{5.2}$$

to calculate the static torsional spring constant of a rectangular cantilever. G is the shear modulus of the cantilever and l, w, and t are the dimensions of the cantilever as defined previously (see table 0.3). However, large errors (up to 30-50%) are introduced via assumptions regarding the elastic constants and in the measurement of the cantilever thickness. Analytical equations can only be used for simple geometries, for more complicated cantilever beams finite element simulations can be used to calculate the spring constants.[136]

5.2.3 Dynamic Methods

The torsional Cleveland method allows for the determination of torsional spring constants by the on-axis loading of masses to the cantilever surface.[135] The torsional resonance frequency is recorded as a function of applied mass. This method involves the possibility of causing damage to the cantilever as several masses have to be physically placed on the cantilever. The major source of error is in the determination of the mass of the (assumed) spherical masses via measurement of their radius. Errors may also be introduced by uncertainties in the positioning of the masses upon the cantilever. It is assumed that the cantilever is not bent by the addition of masses.

The torsional Sader method of Green et al.[135] determines the torsional spring constant of cantilevers via their interaction with a surrounding fluid. A 'hydrodynamic function' which describes how the cantilever resonance frequency depends upon the density and viscosity of the fluid surrounding the cantilever has to be determined. Once the hydrodynamic function is known for a cantilever of a certain shape then all similar cantilevers can be calibrated. Assumptions made in the derivation mean that the cantilever length should be much greater than its width and its thickness.

5.2.4 Comparison of Existing Techniques for Torsional Eigenmode Calibration

Tables 5.1 and 5.2 give a summary of some of the existing torsional calibration methods mentioned above. The tables are a modified and abridged version of table 4 of ref.[51], which provides further detail re-

garding each of the methods. In particular, attention is paid to the wide range of static methods.

5.2.5 Conclusions

It is notable that the accuracy of determination of the torsional spring constants is generally not as good as for the flexural modes. Many of the techniques with higher accuracy involve contact between the cantilever or its tip and a surface, at best blunting the tip at worst incurring more major damage. The methods which are non-destructive tend to have the disadvantage of higher uncertainties. New calibration schemes which have accuracies of better than 10-15% and are non-destructive are desirable.

Method	Summary	Deflection*	Error	Advantages	Disadvantages
Static					
Wedge methods[122–125]	Scan up/down slopes on calibration grid.	No	4-12%	Accuracy	Tip damage is inevitable.
Optical methods[129–134]	Reflect laser off a surface, or twist cantilever.	Yes	5-15%	Low risk of damage	Assumptions on reflectivity. Some involve contact.
Theoretical					
Dimensional[93]	Analytical equations	No	30-50%	Non-destructive	Need dimensions, uncertainty based on their measurement. Geometry approximations required.
Dimensional and FEA[136]	Modeling of real cantilever.	No	30-50%	Non-destructive. Easy to execute for complicated geometries.	Need dimensions, uncertainty based on their measurement. Software requirement.

Table 5.1: *Summary of some of the notable methods for the calibration of the torsional modes of microcantilevers. For a more complete list see ref.[51]. *Indicates whether the scheme requires determination of the cantilever deflection.*

Method	Summary	Deflection*	Error	Advantages	Disadvantages
Dynamic					
Torsional Cleveland[135]	Attach mass, monitor change of ω_{1t}.	No	≈25%	Simple measurement	Uncertainty over the added mass and its position. Potential for damage.
Torsional Sader[135]	Uses l, w along with Q-factor and ω_{1t} and hydrodynamic function.	No	Unreported	Simple to use	Hydrodynamic function must be determined over a range of fluid properties.

Table 5.2: *Summary of some of the notable dynamic methods for the calibration of the torsional modes of microcantilevers. For a more complete list see ref.[51]. *Indicates whether the scheme require determination of the cantilever deflection.*

5.3 Theoretical Model

The development of a new method for the calibration of the torsional spring constants of cantilever beams using a flow of fluid from a microchannel is described in the remainder of this chapter. External forces are applied to change the static cantilever shape, with no effect on the free torsional movement of the cantilever (see figure 5.1).

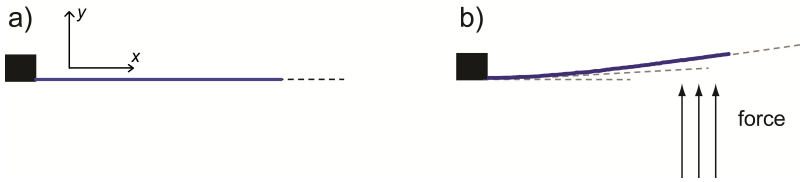

Figure 5.1: *Side view of a non-bent cantilever (a) and a cantilever bent due to applied forces (b). The dashed lines indicate the rotational axes around which the free torsion occurs. The axis changes along the cantilever if the cantilever is curved.*

For a cantilever which has been bent from its static shape there are two relevant effects which could change its resonance frequencies. One is related to the change of the shape of the cantilever which can be described mathematically as a change of the polar moment of inertia, I_p. This can be related to a change of the oscillating energy and resonance frequency. The second effect is thought to have its origin in the stresses induced within the cantilever as a response to its bending. The theoretical model which is built for prediction of the frequency shifts involves knowledge of the torsional modeshapes. It is assumed that these eigenmodes are negligibly affected by the bending and so those of a straight cantilever are used.

5.3.1 Effects Related to a Change of the Polar Moment of Inertia

Equation (2.13) is the differential equation governing the deflection angle of a cantilever beam undergoing torsional deformation about its major axis, which can be solved using the torsional modeshapes, $u_{nt}(x)$. The un-normalised torsional modal shapes are entirely determined by the geometry of the cantilever via the dependence of the shear modulus G, geometric function K, polar moment of inertia I_p and density ρ_c on x, but not by their absolute values. If the modeshape amplitude can be normalised such that it describes the modal energy of a real cantilever then its spring constants at a certain point, e.g. the free end at $x = l$, may be determined via the torsional analogue of equation (4.9),

$$k_{nt} = \frac{\omega_{nt}^2}{u_{nt}(l)^2}. \tag{5.3}$$

When the cantilever's equilibrium position deviates from the straight shape and is flexurally curved the polar moment of inertia changes since the rotational axes no longer coincide with the centre of the cantilever's cross section for all coordinates x along the cantilever length, as depicted by the dashed line in figure 5.1(b). As a consequence, the rotational frequency decreases. The decrease is determined by the polar moment $I_p(x)$ which itself depends upon the new equilibrium shape of the cantilever.

The torsional deflection modes $u_{nt}(x)$ however are almost unaffected if the flexural deflection of the cantilever is small (i.e. if the radius of curvature of the bent cantilever at each coordinate x is large compared to the length of the cantilever).

The change in the polar moment of inertia can be described mathematically using the parallel axis theorem to obtain the moment of inertia

of the bent beam as[137]

$$I_{p,bent}(x) = I_{p0}(x) + \Delta I_p(x) \tag{5.4}$$

where $I_{p0}(x)$ is the polar moment of inertia for the unbent cantilever and

$$\Delta I_p(x) = w(x)t(x)\Xi^2(x) \tag{5.5}$$

is the change in polar moment of inertia due to the bending. $\Xi(x)$ is the static deflection of the cantilever as a function of position along its length. The intrinsic torque of each mode can be expressed as $T_{nt}(x) = G(x)K(x)u'_{nt}(x)$ and can be used to calculate the maximum potential energy,

$$PE_{max} = \frac{1}{2}\int_0^l G(x)K(x)u'_{nt}(x)dx = \frac{1}{2}\omega_{nt}^2. \tag{5.6}$$

The maximum kinetic energy for an unbent cantilever can be calculated via

$$KE_{max} = \frac{1}{2}\omega_{nt0}^2\int_0^l \rho_c(x)I_{p0}(x)u_{nt}^2(x)dx = \frac{1}{2}\omega_{nt0}^2, \tag{5.7}$$

the latter equality being as a result of the eigenmode normalisation (see section 2.5). If a cantilever is then bent by an external force, the polar moment of inertia changes as described by equation (5.4) and the resonance frequency may change to ω_{nt}. However the oscillation energy of each mode remains constant, likewise the eigenmode shapes $u_{nt}(x)$ are unchanged if the deflection is small. Hence, the energy of a bent cantilever may be expressed as

$$KE_{max} = \frac{1}{2}\omega_{nt}^2\int_0^l \rho_c(x)(I_{p0}(x) + \Delta I_p(x))u_{nt}^2(x)dx \tag{5.8}$$

$$KE_{max} = \frac{1}{2}\omega_{nt}^2\int_0^l \rho_c(x)I_{p0}(x)u_{nt}^2(x)dx + \frac{1}{2}\omega_{nt}^2\int_0^l \rho_c(x)\Delta I_p(x)u_{nt}^2(x)dx \tag{5.9}$$

$$KE_{max} = \frac{1}{2}\omega_{nt}^2 + \frac{1}{2}\omega_{nt}^2\int_0^l \rho_c(x)\Delta I_p(x)u_{nt}^2(x)dx \tag{5.10}$$

Since the oscillation energy is unchanged in the bending, equations (5.7) and (5.10) may be equated and the frequency shift ($\Delta\omega_{nt}^2 = \omega_{nt}^2 - \omega_{nt0}^2$) obtained

$$\Delta\omega_{nt}^2 \approx \omega_{nt0}^2 \int_0^l \rho_c(x)\Delta I_p(x) u_{nt}^2(x) dx. \tag{5.11}$$

Strictly speaking the orientation of the axis of rotation also changes along the length of the cantilever, an effect that is not accounted for in equation (5.5) but can be included by the introduction of a rotational axis at x which is tangent to the bent shape, then replacing $\Xi(x)$ with a function which describes the difference between tangential axis and the vertical position of the cantilever at each x further along the cantilever towards its free end.

5.3.2 Effects Related to Bending Induced Stress

When a body is bent from one shape to another stresses and strains are introduced within the body to balance the forces used to bend it. In most applications the strain tensor u_{ik} can be expressed as[62]

$$u_{ik} = \frac{1}{2}\left(\frac{\partial u_i}{\partial x_k} + \frac{\partial u_k}{\partial x_i}\right), \tag{5.12}$$

which is usually considered appropriate for small deformations. x_i is one of the three principle components x, y, and z, u_i is the displacement vector, and the Einstein summation convention is applied. However, equation (5.12) is an approximation and the full strain tensor is defined as[62]

$$u_{ik} = \frac{1}{2}\left(\frac{\partial u_i}{\partial x_k} + \frac{\partial u_k}{\partial x_i} + \frac{\partial u_l}{\partial x_i}\frac{\partial u_l}{\partial x_k}\right). \tag{5.13}$$

The deformation followed by rotation of a thin rod is one case where the product term cannot be ignored,[62] indicating that the latter expression

should be used here.

Our theoretical description of cantilevers using strain related treatments is still under development. Hence no equation showing relationship between the bending induced strains and the frequency shifts is ventured here.

5.4 Experimental Setup

Experiments were performed with a commercial AFM Explorer system (ThermoMicroscopes, Sunnyvale, CA, USA). A homemade smooth parallel plate microchannel fixed on the sample stage of the AFM was positioned such that fluid flow from its exit interacted with the cantilever as illustrated in figure 5.2. Pressure differences, Δp, were applied to the

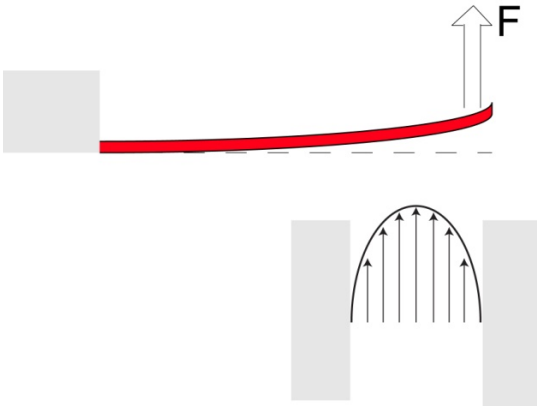

Figure 5.2: *Schematic side view of the microchannel with Poiseuille profile of the fluid and a cantilever which is bent due to forces exerted by the fluid.*

microchannel to drive the flow, establishing stable Poiseuille velocity profiles.[43] Nitrogen gas was used as the working fluid due to its low cost, high purity and well known properties. The microchannel used for all experiments was 100 μm high and 3.5 mm long.

The cantilever was placed above the microchannel such that fluid es-

caping from the exit of the microchannel hits (part of) the plan view area of the cantilever causing a deflection (see figure 5.2). The forces applied to the cantilever by the fluid flow cause a static flexural bending of the cantilever. The bending is sufficient to change the polar moment of inertia of the cantilever and create a stress distribution within it. Its torsional resonance frequencies, which are easily monitored, are altered. The forces experienced by the cantilever depend on the setup. The forces can be accurately determined for example via computational fluid dynamics simulation (section 5.5.2).

The maximum pressure applied to the channel in our experiments was ≈2.5 kPa causing a velocity of nitrogen in the channel mid-line of about 50 m/s.[86] The highest Reynolds number for our setup did not exceed 120. In combination with the Knudsen number in the channel, which is about 0.0005, this Reynolds number corresponds to the laminar regime of incompressible flow.[110] The smallest radius of curvature occurs at the fixed end for the highest applied force and was around 100 m in our experiment; the deflection at the free end was then around 6 μm.

To test the method several commercially available tipless rectangular silicon cantilevers (130-350 μm nominal length, 1 and 2 μm thickness, 0.03-0.6 N/m nominal spring constant, Al backside coating, R-C to R-F, Mikromasch[47] and 442 μm nominal length, 0.12 N/m nominal spring constant, FCL-5A, AppNano[138]) and a V-shaped silicon nitride cantilever (205 μm nominal length, 0.06 N/m nominal spring constant, Au backside coating, V-D, SNL, Bruker[76]) were investigated. All rectangular cantilevers from Mikromash had a nominal width of 35 $\pm$ 3 μm, the AppNano cantilever had a nominal width of 32 μm, and cantilever V-D

had a nominal leg width of 20 ± 5 μm.

The plan view dimensions of all microcantilevers were determined with an Olympus optical microscope for use in conjunction with the Sader method.

Power spectral densities of thermal noise spectra were recorded with an external interface with an accessible frequency range of ≈700 kHz (National Instruments, USB-6251) as a function of fluid velocity. Resonance frequency values, Q-factors, and peak areas for each mode were monitored during measurement with a homewritten LabVIEW^{TM} routine by fitting Lorentzian curves to the resonance peaks similar to the procedure described in ref.[78]. All resonance frequencies were monitored simultaneously. The resonant frequency values are based on the average of 50 individual spectra.

Two slightly different variations of the relative cantilever-channel geometry were used as follows.

5.4.1 Geometry g1

In this geometry the long axis of the cantilever was aligned with the channel width and positioned so as to coincide with the centre of the channel height, see figure 5.3(a). In all tests with this geometry the fixed end of the cantilever was chosen to correspond with the side of the microchannel and the whole of the cantilever plan view area was exposed to fluid flow.

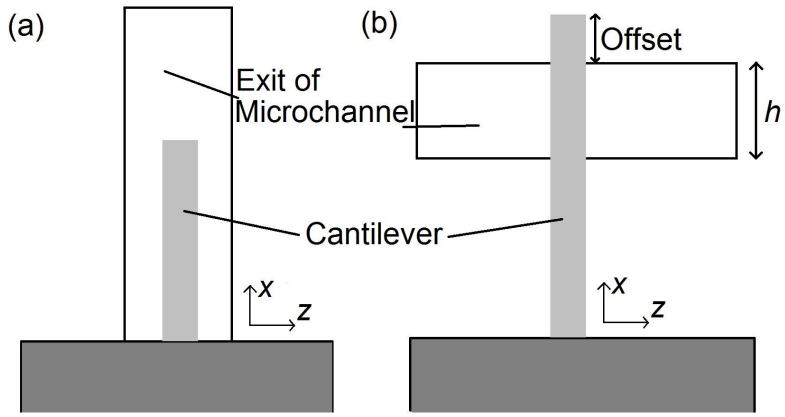

Figure 5.3: *Plan view of the cantilever and channel in the two variations of the perpendicular flow setup, geometry g1 (a) and geometry g2 (b). The flow of fluid from the microchannel exit is out of the plane of the page.*

5.4.2 Geometry g2

In geometry g2 the long axis of the cantilever coincides with the channel height, all of the cantilevers tested were longer than 100 μm (the channel height) and so only part of the cantilever was directly exposed to the flow from the channel. Figure 5.3(b) defines the geometry and the offset between the free end of the cantilever and edge of the channel. In most of the tests an offset of zero was used. In the following data an offset of zero should be assumed unless otherwise specified.

Due to less of the cantilever being hit by the flow than in geometry g1, a larger pressure range was available for a given range of deflections thereby reducing any errors associated with the pressure sensor. Also, it was easier to align the free end of the cantilever with the edge of the channel than to accurately position the cantilever in geometry g1. Therefore this setup was used in the majority of experiments.

5.5 Simulations

The path of fluid flow from the channel and around the cantilever was simulated using Elmer.[55] Meshes required in the simulations were created with Gmsh.[56] The mesh independence of the results was confirmed by further mesh refinement. The forces applied to the cantilever by the fluid were also calculated. From the forces the static bending of the cantilever can be calculated. With a suitable theoretical treatment, the cantilever deflection can be used to predict resonance frequency shifts. Note that the forces calculated for a static cantilever are sufficient. The relevant data and results are outlined here, further details of the simulations and meshes are given in appendix A.

5.5.1 Simulations for Geometry g1

Figure 5.4 shows a simulation of the flow pattern around a 350 μm long rectangular cantilever in geometry g1. As the width of the channel is

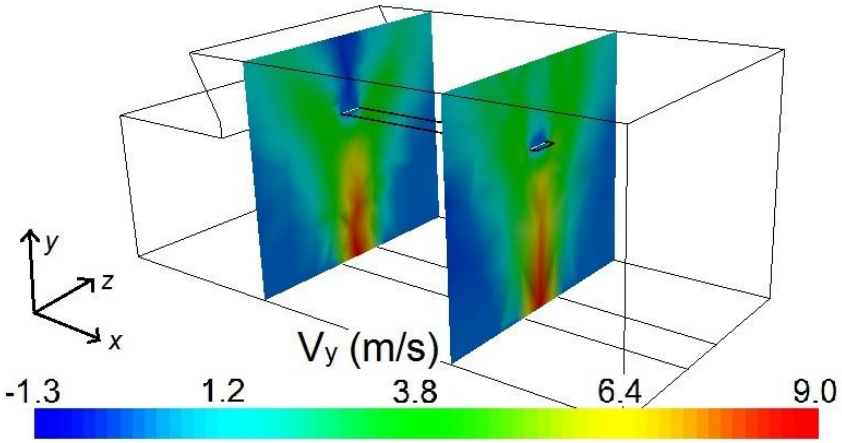

Figure 5.4: *Two-Dimensional slices through a three-dimensional simulation of the fluid flow around a rectangular cantilever in geometry g1.*

aligned with the cantilever's long axis, the whole of the cantilever is hit

by the flow. As shown in figure 5.4, the flow profile is similar over the majority of the cantilever. The presence of the chip has only a small effect since the end of the chip is aligned with the edge of the channel and thus does not occlude the exit. The free end has a slightly different profile as the fluid can flow around both the sides and the free end. For this reason the forces are slightly larger at the free end than at the fixed.

5.5.2 Simulations for Geometry g2

Figure 5.5 shows a simulation of the flow pattern around a 350 μm long rectangular cantilever for zero offset and altitude of 50 μm above the exit in geometry g2. The associated forces parallel and perpendicular to the cantilever are shown in figure 5.6. It is the forces, F_y in the y-direction

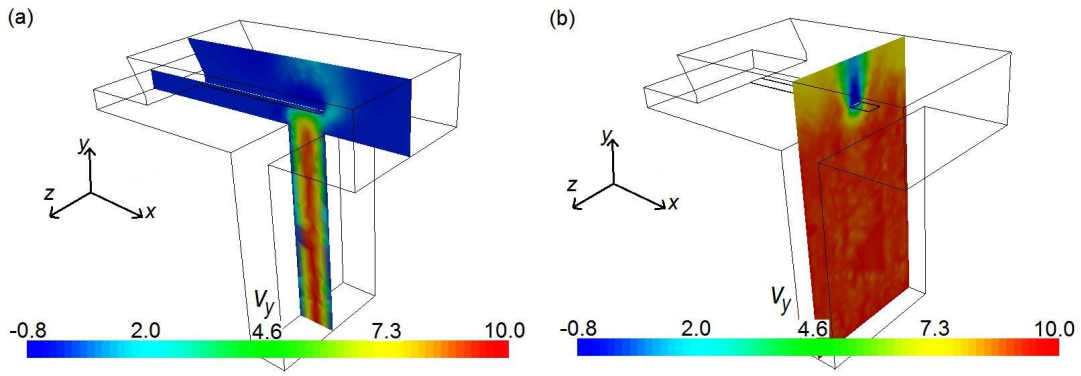

Figure 5.5: *Simulated fluid flow around a rectangular cantilever in geometry g2. Two-dimensional slices of the three-dimensional simulation are shown, slice along the x-axis (a) and slice across the cantilever (b).*

which act to bend the cantilever into its new shape. The frequency shifts induced by any flow along the cantilever length (via F_x and calculations similar to those of chapter 4) are negligible, particularly as the positive and negative forces F_x counteract each other as demonstrated pictorially in figure 5.6.

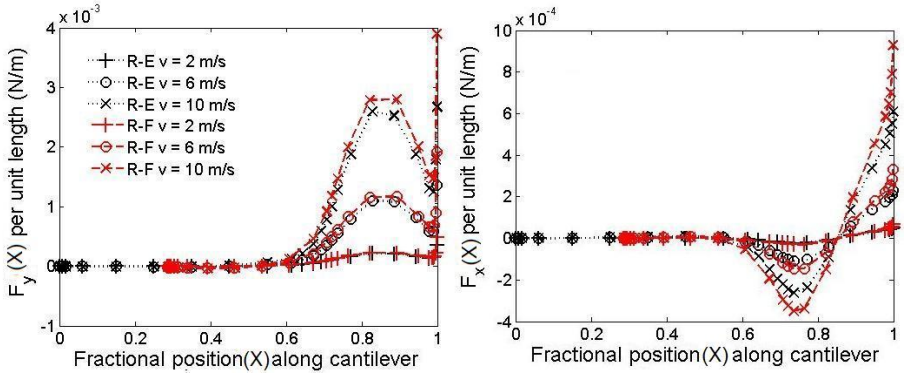

Figure 5.6: *Forces applied to the cantilever in the y and x directions in the perpendicular fluid flow setup as a function of position along the cantilever length. Traces for three speeds: 2 m/s ('+'), 6 m/s ('$\circ$'), 10 m/s ('$\times$') and two rectangular cantilevers: the 350 μm long R-E (black dots) and the 250 μm long R-F (red dashes).*

Note that the force profiles in figure 5.6 are shown for two rectangular cantilevers of different lengths. Since the forces are zero towards the fixed end of the cantilever, the force profile for the shorter cantilever (R-F) can simply be shifted such that it begins at $x \approx 0.3$, then the free ends of both cantilevers coincide. The profiles match one another and it seems that one force profile can be used for all rectangular cantilevers in this geometry.

The forces (figure 5.6(a)) from the simulations of fluid flow were used in suitable theoretical models (described in section 5.3.1) to predict the torsional frequency shifts (section 5.6). The forces may also be used in further simulations to calculate the expected deflection, along with the modeshape and resonance frequency of a bent cantilever. Simulations of a deflected cantilever show that the eigenmodes are unaffected for all of the deflections encountered. One modal shape of a bent cantilever is shown in figure 5.7. The simulated modeshape shown in figure 5.7 for

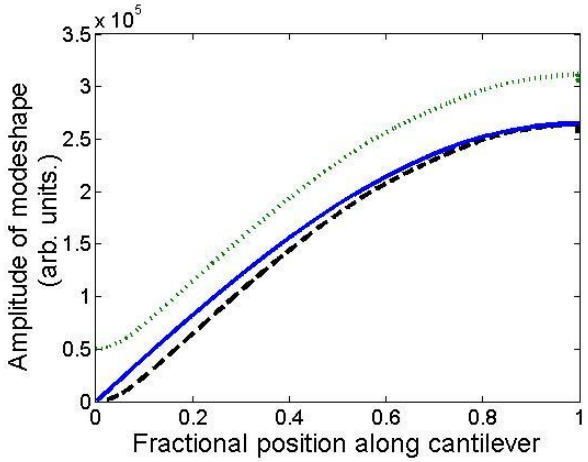

Figure 5.7: *Simulated modeshapes of the first torsional mode of a straight (dashed line) and a bent (dotted line) rectangular cantilever and the theoretical modeshape (solid line) from equation (2.15). The modeshape for the bent cantilever has been shifted up the y-axis for sake of clarity. It coincides with the modeshape of the simulated straight cantilever.*

the bent cantilever has a static deflection of around 6 μm at the free end. The figure also shows that the simulated modeshape differs slightly from the theoretical one around the fixed end of the cantilever. Figure 5.8 shows results of a simulation where the forces of figure 5.6 were used as boundary conditions to bend the cantilever into new static shapes, this was followed by eigenmode analysis to obtain the predicted mode shapes and resonance frequencies. The simulated bending is in line with that from theoretical calculations based on the forces. The predicted frequency shifts of the torsional eigenmodes as displayed in figure 5.8 show a variety of behaviours. For the 1 μm thick rectangular cantilever R-E the frequency of the first torsional mode decreases with bending, as expected for effects dominated by changes of the polar moment of inertia. However, the second and third modes show positive frequency shifts,

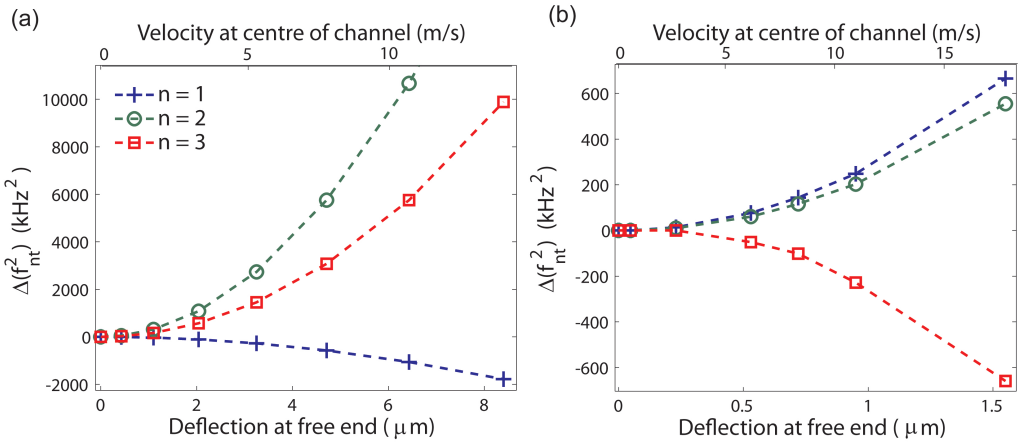

Figure 5.8: *Simulated bending and frequency shifts of the first three torsional modes of a 1 μm (a) and 2 μm (b) cantilevers R-E. The frequency shifts have been scaled by assumed material properties for an ideal silicon cantilever.[59]*

possibly due to the distribution of the bending-induced stress within the cantilever. A 2 μm thick cantilever R-E is predicted to show quite different behaviour, only the third torsional mode displays a negative frequency shift. In this case the positive frequency shifts of the first two torsional modes indicate that they may be dominated by stress-strain related effects.

The total stress distribution at any position in a structure is given by the von Mises stress.[139] Figure 5.9 shows the von Mises stress distribution throughout a bent cantilever. It is zero on the cantilever centre line (the neutral plane) and increases to the top and bottom surfaces of the cantilever. The stress is highest near the fixed end as this is the position where the bent cantilever has the greatest curvature.

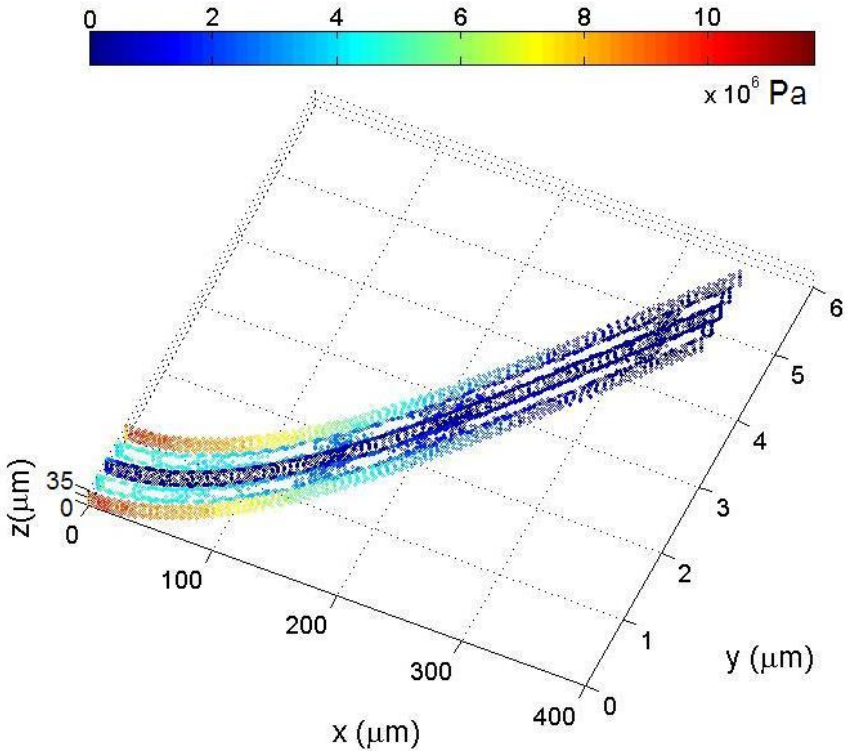

Figure 5.9: *von Mises stress, given by the colour scale, within a bent 1 µm thick cantilever R-E. Materials properties of a silicon cantilever have been assumed.[59]*

5.5.3 Simulation of a V-Shaped Cantilever in Geometry g2

The same process as for the rectangular cantilevers can be executed for the V-shaped cantilever to obtain its predicted frequency shifts from simulation. The fluidic forces were calculated and used to bend the cantilever and determine its eigenmodes and eigenfrequencies. Again, the modeshapes are unchanged by the deflection and the simulated frequency shifts are shown in figure 5.10. Positive frequency shifts, increasing in magnitude with fluid speed are predicted for all of the torsional modes.

The frequency shifts of the two flapping modes have also been included in figure 5.10. The predicted frequency shifts are positive and certainly of a measurable, significant magnitude.

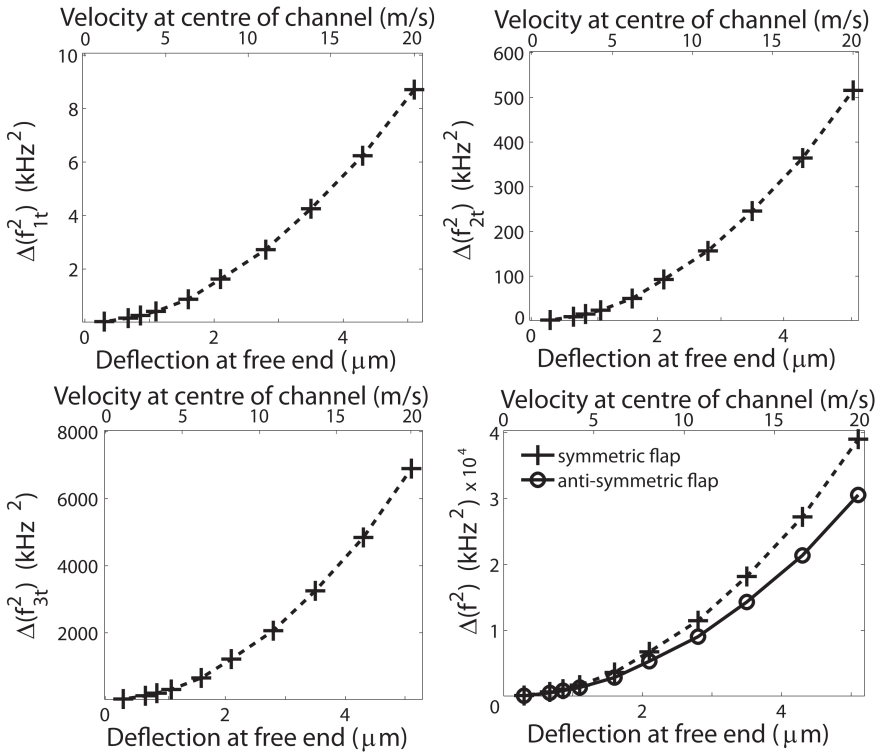

Figure 5.10: *Simulation of the frequency shifts of a V-shaped cantilever (V-D) bent by fluidic forces. Data shown relates to the first three torsional modes and the two flapping modes. The frequency shifts have been scaled by assumed material properties for an ideal silicon nitride cantilever.[59]*

5.5.4 Transient Simulations

The experimental setup, where a structure blocks part of a flow from a channel, is reminiscent of the classic fluid dynamical problem known as the von Kármán Vortex Street, as depicted in figure 5.11. The Reynolds number for this example is around 100, the critical value for the onset of the vortices being around 90. Vortices are shed from alternate sides of the structure (a 2-D projection of a cylinder) at this Reynolds number. For higher Re the vortices become more pronounced before becoming fully chaotic.

Transient simulations of our setup were executed with Elmer to asses

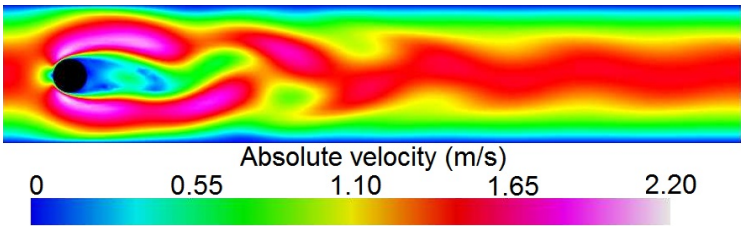

Figure 5.11: *Simulation showing von Kármán vortices evident in flow around a cylinder.*

whether transition to turbulence or structures similar to the von Kármán vortex street were important. The highest Reynolds number used experimentally was around 120, larger than that in the example in figure 5.11. However, simulations of the experimental setup at these Reynolds numbers did not provide any evidence of vortices or turbulence. Simulation of higher speeds (20 m/s or more) did occasionally show some turbulence, but not repeatedly so. It must be noted that turbulence and the transition to turbulence is considered to be one of the weaknesses of Elmer. Simulation with different software packages and fully coupled (dynamic fluid-structure interaction) calculations might provide more accurate information.

5.6 Experimental Results

Several cantilevers were tested using both geometry g1 and g2. Only the first torsional mode was accessible for all rectangular cantilevers due to limitations on the maximum sample frequency of the experimental setup. The first three torsional modes of a V-shaped cantilever were observed.

The plan view dimensions of the cantilevers were determined using optical microscopy, and were generally similar to those shown in table 4.3. Individual values are quoted below where quantification is required.

5.6.1 Geometry g1, Rectangular Cantilevers

Figure 5.12(a) shows the torsional resonance frequency spectrum of a 1 μm thick rectangular cantilever R-E. The frequency shift of the fundamental torsional mode of this cantilever in geometry g1 is shown in figure 5.13. The resonance frequency decreases as the cantilever is bent by increasing flow speed. The negative frequency shift is consistent with a change of the moment of inertia effect.

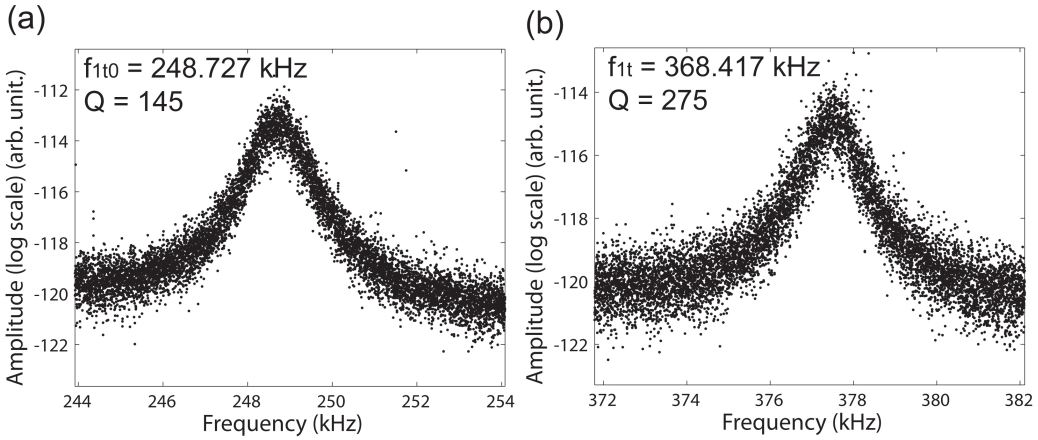

Figure 5.12: *Resonance frequency curves of the first torsional mode of two rectangular cantilevers. The curves are for the resonance with no flow of a cantilever which is 1 μm thick (a) and a 2 μm thick cantilever which has been bent by fluid flow (b). Both cantilevers are nominally 350 μm long and 35 μm wide.*

5.6.2 Geometry g2, Rectangular Cantilevers

Rectangular Cantilevers where the Frequency Shift is Predominantly due to Changes of the Moment of Inertia

Figure 5.14 shows the frequency shift of the first torsional resonance frequency for a rectangular cantilever (nominal length 350 μm, width 35 μm, thickness 1 μm; measured length 339 μm, width 31 μm) depending

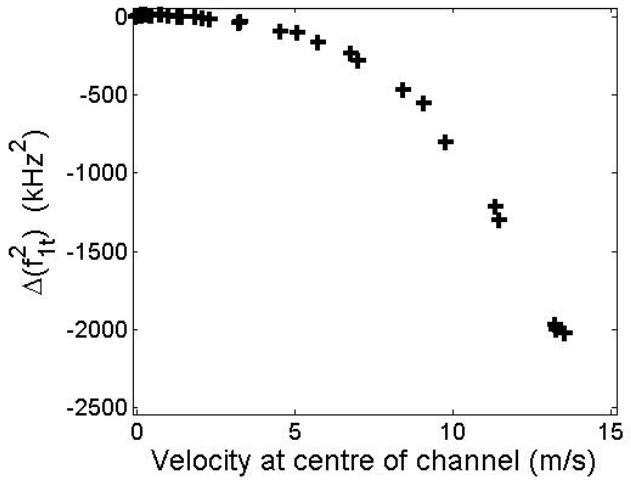

Figure 5.13: *Frequency shift of the first torsional mode of a rectangular cantilever (R-E: t=1 μm, w=35 μm and l=350 μm) in the perpendicular geometry g1. The resonance frequency spectrum at zero flow velocity for this cantilever is shown in figure 5.12(a).*

on the speed of the fluid escaping from a microchannel together with a fit of the shifts predicted by equation (5.11) using the simulated forces. The channel width was oriented parallel to the cantilever length and the cantilever was 50 μm above the channel exit (as depicted in figure 5.3(b)).

The flexural rigidity of the cantilever was determined independently beforehand to be 0.0434 ± 0.0020 N/m by the method described in chapter 4. The forces exerted by the fluid were determined by simulation. The experimental frequency shifts (displayed in figure 5.14) show the same trend and have similar magnitude to those predicted by the simulation, figure 5.8.

Assuming that the observed frequency shift is entirely the result of a change of the moment of inertia, a single parameter (B in equation (2.15)) was fitted such that the theoretical frequency shifts match those observed in the experiment. This corresponds to a normalization of the eigenmode

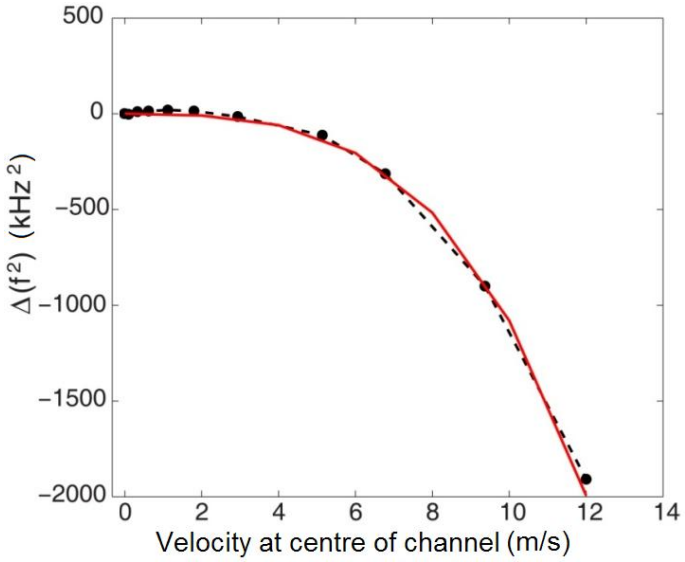

Figure 5.14: *Experimentally obtained torsional shifts $\Delta(f_1^2)$ (dashed line) and fitted calculated shifts (solid line) for rectangular cantilever R-E (1 μm thickness). The deflection of the free end of the cantilever is around 7 μm for the highest speed in the figure.*

function as in equation (2.17). With this normalized function, u_{nt}, the torsional spring constants k_{nt} for a torque applied at the free end of the cantilever are obtained from equation (5.3). This procedure resulted in a fundamental torsional spring constant of k_{1t}=2.2×10^{-9} Nm. The Sader method[111] gives for the same cantilever a value of k_{1t}=2.3×10^{-9} Nm (using l=339 μm, w=31 μm, f_{1t}=248.102 kHz, Q=160).

Variation in $\Delta(f_{1t}^2)$ with Offset **Figure 5.15 shows the effect of changing the offset of the free end of the cantilever relative to the edge of the microchannel. For an offset of -50 μm the free end of the cantilever coincides with the centre of the channel. The deflection reported in the figure is a normalised change of photodetector signal. This is related to the angle of the cantilever at the position of the laser spot (close to**

the free end) and is assumed to represent the static deflection of the cantilever. From figure 5.15 it is clear that the static deflection and frequency shift are closely linked as expected.

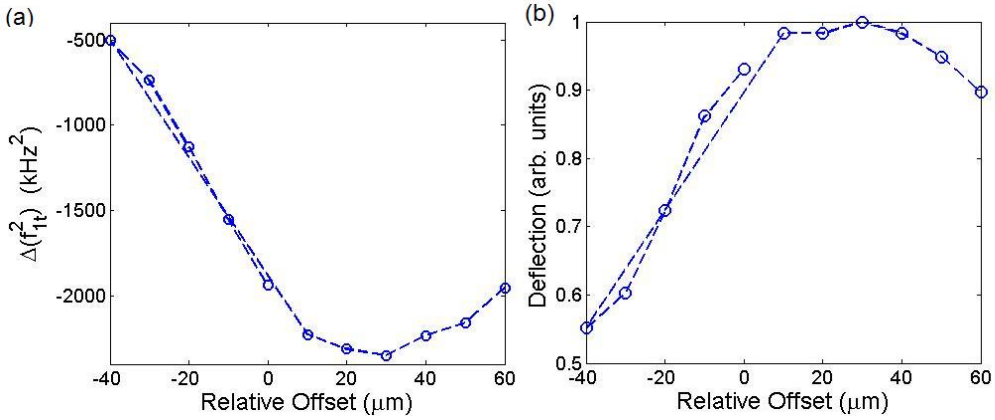

Figure 5.15: *Effect of changing the offset on the obtained frequency shifts (a) and deflection (b) of a nominally 1 μm thick rectangular cantilever R-E. The change of the deflection in (b) is around 2 μm at the cantilever free end.*

Rectangular Cantilevers where the Frequency Shift is Positive

Rectangular cantilevers with larger spring constants show positive frequency shifts which possibly relate to bending induced stresses and strains. Figure 5.12(b) shows the resonance frequency spectrum for a 2 μm thick cantilever R-E in a bent state. The spectrum remains symmetrical and the Q-factor was not altered significantly due to the bending. Figure 5.16(a) shows the frequency shifts for two cantilevers of 2 μm thickness. The only difference between R-E in this figure and that in figure 5.14 is that it has twice the thickness and therefore a factor of 8 greater spring constant. However, the frequency shifts show a different sign, as was predicted by the simulations of section 5.5.2. The magnitude of the static bending is reduced (relative to the 1 μm thick cantilever)

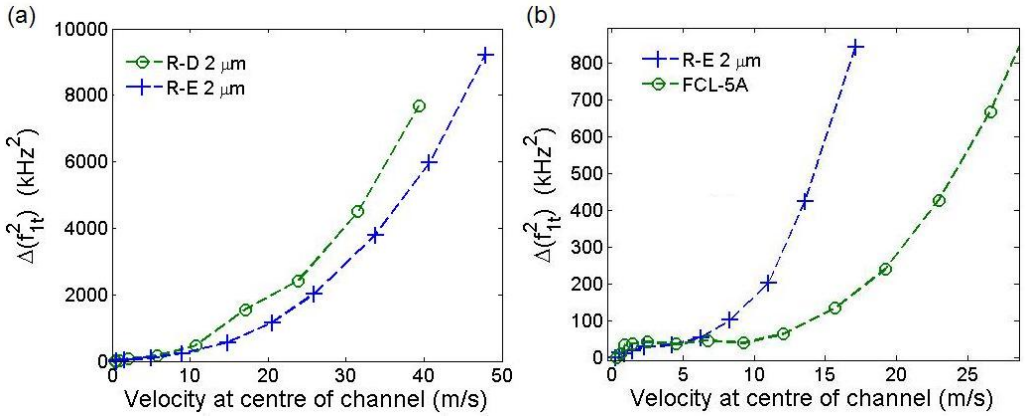

Figure 5.16: *Stress dominated frequency shifts as observed for nominally 2 μm thick cantilevers. The two traces for the shifts associated with 2 μm thick R-E are two different cantilevers and thus show different absolute frequency shifts. The resonance frequency spectrum corresponding to the largest frequency shift of cantilever R-E 2 μm in (b) is shown in figure 5.12(b).*

due to the larger spring constant, the maximum deflection of the 2 μm thick cantilever R-E in figure 5.16(a) was around 2 μm for the point at $\approx$45 m/s.

Figure 5.16(b) shows the frequency shifts for cantilever FCL-5A (nominally t=2 μm, w=32 μm, and l=440 μm) alongside a second 2 μm thick R-E. Both of these cantilevers show positive frequency shifts but the magnitude for R-E is around half that of the cantilever in figure 5.16(a). The cantilever FCL-5A shows a large range of velocities (2-10 m/s) where the shift does not change but the static deflection increases throughout. This points to two competing effects.

5.6.3 Geometry g2, V-shaped Cantilevers

Frequency shifts have been measured for the first three torsional eigenmodes of V-shaped cantilever V-D in geometry g2. Figure 5.17 shows

their resonance peaks. The frequency shifts of the first three torsional

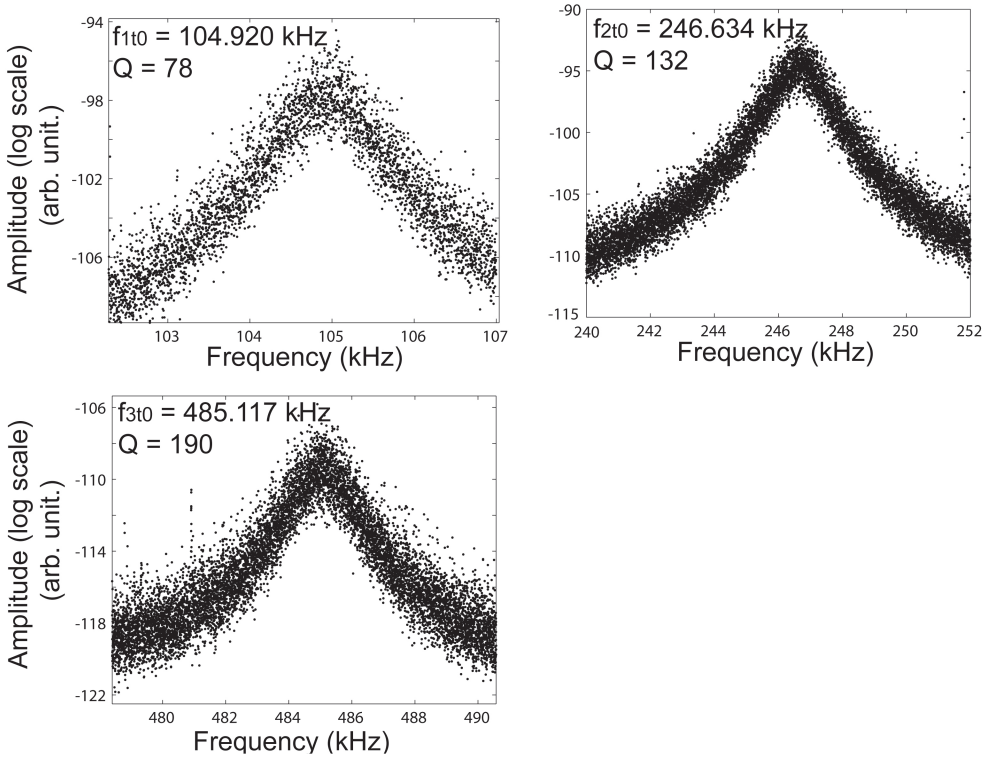

Figure 5.17: *The first three torsional resonance frequency spectra of cantilever V-D.*

modes are displayed in figure 5.18. The shifts here show a more complicated relationship with the static deflection and velocity than predicted by the simulations. The first torsional resonance frequency shift increased linearly with velocity. Meanwhile the second and third frequency shifts change sign through the velocity range.

5.7 Discussion

5.7.1 Geometry g1, Rectangular Cantilevers

The results for the 1 μm thick cantilever R-E tested in geometry g1 show that the frequency shifts are dominated by effects relating to a change of the moment of inertia. Nonetheless, the obtained $\Delta(f_{1t}^2)$ is likely to have

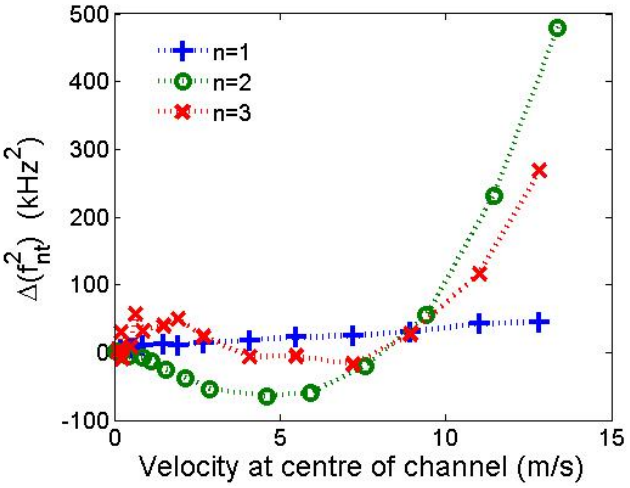

Figure 5.18: *Frequency shifts of the first three torsional modes of cantilever V-D.*

been affected by (as yet un-quantified) bending induced strain effects.

5.7.2 Geometry g2, Rectangular Cantilevers

The geometry g2 has been used over geometry g1 in the majority of the experimental work due to accurate positioning being easier to execute. Furthermore geometry g2 is preferred due to the availability of a wider pressure range on account of smaller cantilever surface area being exposed to the flow. Therefore the cantilever experiences lower forces and less deflection for a given fluid velocity.

Figure 5.7 confirms that the eigenmode shape of an unbent cantilever can be used in all calculations involving bent cantilevers. There is, however, a difference between the theoretical and simulated modeshape at the fixed end of the cantilever. Presumably this accounts for some of the difference between the fundamental torsional resonance frequency as determined analytically using equation (2.16), f_{1t}=189.001 kHz, and that from the FEA simulation, f_{1t}=234.543 kHz.

As a demonstration of the method the fundamental torsional spring

constant was calculated for a 1 μm thick cantilever R-E assuming that the frequency shift was purely due to moment of inertia effects. The resulting value for k_{1t} was remarkably close to that determined from the Sader method. There is likely to be a contribution to the shift from the unquantified effects which produce positive frequency shifts of some cantilevers which was not accounted for in the calculation of the spring constant. It is serendipitous that the values of k_{1t} from the two different methods exhibit such good agreement. It should be noted that the uncertainties associated with the torsional Sader method have not been reported, but it would be surprising if they were smaller than the 10-20% error quoted for the related flexural method. Likewise the experimental error in the value derived using the method described here is unlikely to be less than 10% at present. Through comparison of the simulated frequency shifts (figure 5.8(a)) and experimental shifts (figure 5.14) it is clear that the experimental positioning was accurate and that the simulated shifts are relevant. The trend of $\Delta(f_{1t}^2)$ with increasing velocity, along with the magnitude of the shifts, show that the simulated and experimental results are in reasonable agreement.

The bending forces applied to the cantilever are very similar for a range of altitudes above the exit of the microchannel of between 45 and 60 μm, figure 5.19. This means that the frequency shifts and any calibration scheme based on the method is insensitive to an inaccuracy in the positioning of the cantilever in this direction.

The sensitivity to error in positioning of the free end of the cantilever relative to the edge of the channel (the 'offset') is demonstrated in figure 5.15. The figure shows that the static bending and frequency shift

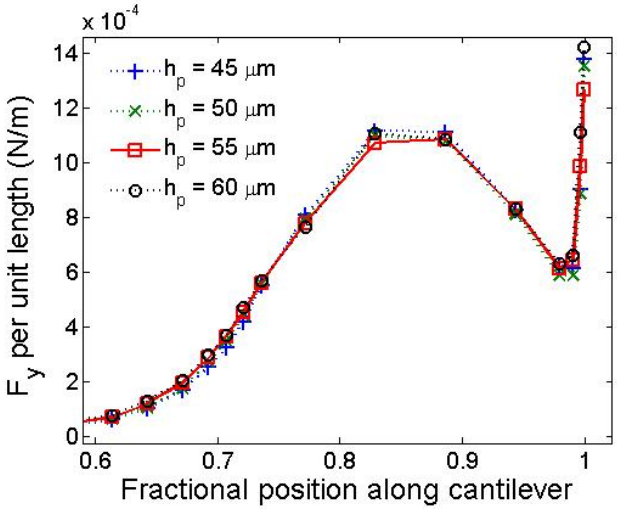

Figure 5.19: *Effect of error in height above channel in the simulation of the forces applied to the cantilever in geometry g2.*

are relatively insensitive around the relative offset of 30 μm in the figure. This offset should therefore be the one which is used in applications of the method. Figure 5.15 also confirms that the cantilever deflection and torsional resonance frequency are linked. As the deflection increases the magnitude of $\Delta(f_{1t}^2)$ does likewise.

The simulated and experimentally obtained frequency shifts for the 2 μm thick cantilevers show reasonable agreement. The simulations include the effect of the stress in bending, unlike the analytical calculations which, currently, only account for effects relating to changes of I_p (section 5.3.1). Frequency shifts associated with a ΔI_p can only be positive if a cantilever is initially bent and is deflected to an unbent shape. If such an operation were carried out experimentally then the rate of change of frequency shift with speed would decrease, i.e. the gradient of the curve in figure 5.16 (for example) would decrease with increasing fluid velocity, which has not been observed experimentally.

The positive frequency shifts can only be explained if there is a sec-

ond effect competing with ΔI_p. The simulations of the eigenmodes of the deflected cantilever with stress capture this effect. If a curved cantilever (therefore having no stress) is simulated then no positive shift is obtained, only a negative one due to the change in I_p relative to a straight cantilever. This points to the second effect being related to the stress created in bending a cantilever. As described in section 5.3.2 the effect cannot be linear as this would have no effect on the energy of the oscillations and therefore the cross term in equation (5.13) is required, which complicates matters. The requirement for higher order terms was confirmed by simulation with Comsol Multiphysics,[140] where the frequencies could be calculated with and without the higher order terms. The relationship of strain effects to the energy of oscillation and therefore the frequency shift has a strong dependence on the thickness of the cantilever. Though the thickness dependence is accentuated by the fact that the flexural spring constant of the thicker cantilevers is larger and therefore the static bending (and related I_p effect) is smaller.

The experimental setup is similar to the geometry typically used to demonstrate the von Kármán vortex street. It is therefore relevant to execute transient simulations of the experimental geometry to observe whether vortices, or turbulent areas, are expected to form. No such structures were observed for experimentally relevant flow speeds, though it is worth noting that the transition to turbulence is still an area where computational simulation poorly replicates the real-world behaviour. Experimentally, no evidence of turbulence in the flow around the cantilever was observed. Signatures of turbulence or vortex formation could include increases in the oscillation amplitude of the modes, loss of some of the

resonance peaks, or unstable static deflections. It seems reasonable to assume that vortex formation in the wake of the cantilever is insignificant for the geometries and flow velocities tested.

5.7.3 Geometry g2, V-Shaped Cantilevers

The simulated frequency shifts for the torsional modes of a V-shaped cantilever show a parabolic increase with fluid velocity (figure 5.10). While the experimental results (figure 5.18) also show a positive shift there appears more detail than in the simulated shifts. The experimental $\Delta(f_{1t}^2)$ appears linear with velocity while there is a small negative shift for the second and third torsional eigenmodes. The discrepancy could be related to the simulation of an ideal V-shaped cantilever and also, particularly in the case of $\Delta(f_{3t}^2)$, due to desorption of water from the surface of the cantilever as dry nitrogen from the channel replaces humid air around the cantilever.[21] It is reasonable to expect that the torsional frequency shifts of V-shaped cantilevers consist of the competing moment of inertia and stress related effects as observed for rectangular cantilevers.

This method could also provide a pathway for the calibration of the flapping modes of the legs of V-shaped cantilevers. Figure 5.10 predicts that the perpendicular flow-induced bending will induce measurable frequency shifts of the two flapping modes. Unfortunately they have not been measured experimentally as the resonance frequencies of these modes are too high for use with the current experimental setup.

5.7.4 Higher Torsional Modes

In a similar manner to the method described in chapter 4 for flexural modes, the calibration of the fundamental torsional eigenmode can be extended to all torsional eigenmodes. The shapes of the eigenmodes must be known, which is easy to determine for rectangular cantilevers and are shown in figure 2.6. Finite element simulation of the eigenfrequencies suggests that the static bending will induce measurable frequency shifts of the higher modes. Unfortunately, for all rectangular cantilevers tested, the second torsional mode was of a higher frequency than accessible using the current experimental setup.

Frequency shifts have been observed for second and third torsional modes of a V-shaped cantilever. However, the determination of the torsional eigenmode shapes for such cantilevers is not straightforward and most calculations involve approximations where the two legs are disconnected or where they are essentially joined along their length to form an effective rectangular cantilever.[61] Such treatments are acceptable in flexural deformations but may result in errors for the torsional modes. One can turn to FEA simulations, as in figure 2.9, which show that the torsional deflection might have to be described by functions not only of the position along the cantilever, but also across it. Without a simple, accurate model of the eigenmode shape the experimentally observed torsional frequency shifts cannot be used to calibrate the torsional spring constants of V-shaped cantilevers.

5.8 Further Work

The most important outstanding aspect of this work is in the quantification of the effect of bending induced strain within the microcantilevers. It seems that the effect causes a positive frequency shift and the importance of the effect increases with the cantilever spring constant. Non-linear, higher order mixed terms of the strain tensor appear to be required to adequately describe the experimental situation, confirmed by simulation with and without these terms with Elmer and Comsol Multiphysics.

The principle of the method has been shown in the calibration of the fundamental torsional spring constant of a rectangular cantilever. Given a cantilever with a lower spring constant where the higher modes can be measured experimentally then their spring constants may be determined using the method.

The spring constants of the torsional modes of V-shaped cantilevers have not been quantified in this document. The torsional eigenmode shapes must first be calculated, probably by simulation. Once the forces are quantified the spring constants can be calculated in the scheme described above. Frequency shifts of the flapping mode (section 2.4.3) of the legs of a V-shaped cantilever have not been observed experimentally, but are predicted to show measurable frequency shifts. Calibration of this mode might be interesting for sensor technologies, but probably not for AFM applications as this mode results in no movement of a tip placed in the conventional position.

The combination of the methods for calibrating both the flexural (as described in chapter 4) and torsional eigenmodes (this chapter) could be used concurrently to calibrate the spring constants of hammerhead (or

T-shaped) cantilevers, an application where both types of oscillation are used.

One final application of the technique could be in the determination of the shear modulus, G. If the geometry and in particular the thickness are accurately known, therefore K is calculable and the shear modulus could be determined with high accuracy for any resonator. The torsional rigidity, GK, for a rectangular cantilever can be obtained from:

$$GK = \frac{\omega_{nt}^2}{\int_0^l u'_{nt}(x)dx} \tag{5.14}$$

where $u'_{nt}(x)$ denotes the derivative of the normalised eigenmodeshape with respect to x. $u'_{nt}(x)$ can be normalised by comparison between the simulated shifts using not normalised modeshapes with the applied forces and the experimentally obtained frequency shifts. This could be of interest as the materials properties of very small structures can vary from that of the bulk,[37, 141–143] but methods to quantify the variation are limited.

5.9 Conclusions

A method with the potential to be used in the calibration of all of the torsional eigenmodes of microcantilevers has been described in this chapter. The method involves a static bending of the cantilever whilst monitoring its resonance frequencies. A flow of fluid bends the cantilever and therefore there is no risk of damage to tip, cantilever or any coating upon its surface. Two competing effects are the origin of changes of the torsional resonance frequencies. One relates to the change of the polar moment of inertia as a straight beam becomes curved. The second effect of relevance

to the frequency shifts is thought to be the bending induced stresses and strains and their influence on the oscillation energy of the beam.

Preliminary results have been shown, for a full understanding and quantitative calibration of the torsional spring constants of all cantilevers the effects causing the positive frequency shifts must be understood. Attempts to quantify the effect of the stress on the torsional resonance frequencies are ongoing. Once this effect is quantified then the method can be used to simultaneously calibrate the torsional spring constants of rectangular cantilevers.

6 Conclusions

The importance of the higher flexural modes of microcantilever sensors has been shown by the demonstration of their increased sensitivity to adsorbed mass. For the unmodified rectangular cantilever of chapter 3 the fourth flexural mode showed a sensitivity of almost twenty times that of the fundamental mode.[21] Such sensitivity increases allow larger cantilevers operated in higher modes to detect the ultrasmall forces which only smaller probes have previously sensed.[45] The sensitivity of any cantilever may be enhanced by operation in a higher flexural mode. The implementation of the higher modes in chapter 3 reinforces the findings of several other studies which point to the potential of the higher eigenmodes.[8, 22–25]

All of the existing calibration schemes (as outlined in section 4.2) were developed with the aim of the calibration of the fundamental flexural mode. Very few of the methods can be extended to the higher eigenmodes. Armed with the knowledge that the higher flexural modes can have enhanced sensitivities a method was developed with which to calibrate all flexural modes of microcantilever sensors. Chapter 4 describes the method. It is swift, as it can calibrate multiple flexural modes simultaneously, and involves no requirement for contact of the microcantilever or tip with a hard surface. Therefore it is ideal for AFM cantilevers with ultrasharp tips or for cantilevers which have been modified with a sensitive coating. The accuracy of the derived spring constant for any mode using this technique is comparable to that derived for the fundamental mode by many of the existing methods.

Every experimental technique has its disadvantages. In the method described for the calibration of the flexural eigenmodes the primary weaknesses are in the cantilever positioning and the need for the simulation of the forces for a given position. In mitigation, only the positioning of the cantilever relative to the channel height is of importance. The forces applied to the cantilever are insensitive to changes of several tens of micrometres in the distance from the exit of the channel. Likewise, the relative angle between cantilever and channel may vary through several degrees with little effect on the forces. However, for the simulated forces to be relevant to the experimental execution the position relative to the channel height must be set to within around five micrometres. Similarly the positioning of the cantilever relative to the channel exit is the most important action in executing the method for the calibration of the torsional spring constants. Again, changes of the angle of the cantilever and the distance from the microchannel exit are relatively unimportant.

It is envisaged that in any application of the calibration methods the apparatus could be engineered such that the positioning in the most critical direction is the most accurate. The other directions and the angles can be allowed larger tolerances. The microchannel must be rotated by 90° between the setups for torsional and flexural calibration. A single channel which may be mounted in either geometry would be easy to produce, though in this study two different channels were used.

The simultaneous calibration of both the flexural and torsional modes could be possible. An angle between cantilever and channel where the cantilever is bent sufficiently for torsional frequency shifts, but where the flow does not affect the flexural eigenmodes would be required. No

investigation into this possibility has been made but the required angle between cantilever and channel long axes may be in the 5-20° range. Lower angles favouring accuracy in the calibration of the flexural spring constants and higher favouring the torsional calibration. Simulations could be executed to determine the angle giving the best compromise. One application of particular interest for a combined flexural-torsional calibration is in the use of hammerhead, or T-shaped, cantilevers. These cantilevers have an off-axis tip, thus torsional modes contribute an enhanced proportion of the total tip movement (over cantilevers with on-axis tips).

Whilst this work has shown that the higher flexural modes can have a greater sensitivity to external influences no work has been completed to prove that the same is true for the higher torsional modes. These modes were not accessible with the existing experimental setup for any of the rectangular cantilevers tested. Cantilevers with lower torsional spring constants would have to be used to gain access to the higher modes.

While AFM images have been collected using the higher flexural eigenmodes of rectangular cantilevers[23–25] the spring constant of the higher mode was only inferred from that of the fundamental mode and the ratio of the resonance frequencies. Meanwhile, the spring constant of the second flexural mode has been calibrated using the Sader method and a modified thermal noise method.[49] However, no study exists where the spring constants of the higher flexural modes have been calibrated and then used for the collection of an AFM image. It would be interesting to calibrate all modes of a microcantilever and to compare the data obtained, for example plots of sample elasticity, from scanning a surface

using each of the different eigenmodes.

A Details of the Simulation Process

For the vast majority of simulations meshes were created using Gmsh.[56] The meshes were then imported and used in simulations in Elmer,[55] an open source multiphysics software package.

A.1 Gmsh

Gmsh version 2.4.2[56] was used for most meshes, which were refined and optimised using the netgen algorithm. Figures A.1 and A.2 show a mesh created in this manner and is typical of the majority of the executed simulations and the data presented throughout this document. Figure A.1(a) shows the surface mesh over the entire geometry, it is finer on the cantilever surface (as shown in the zoomed figure A.1(b)) and rougher on the larger boundaries.

Gmsh V2.6.0 was also used to customise areas of very fine mesh according to interests, V2.4.2 has bugs in this part of the program. The most important use of V2.6.0 was in the addition of a 'box' where a different characteristic mesh length could be requested, for example around the cantilever. The following show the additions to the geometry (.geo) file needed to create a finer mesh within the three-dimensional volume defined by XMin, XMax, YMin, YMax, and ZMin, ZMax:

```
cl1 = 0.000053;
Point(1) = {0, 50e-006, 0, cl1};
Point(2) = {0, 50e-006, 245e-6, cl1};
.
.
```

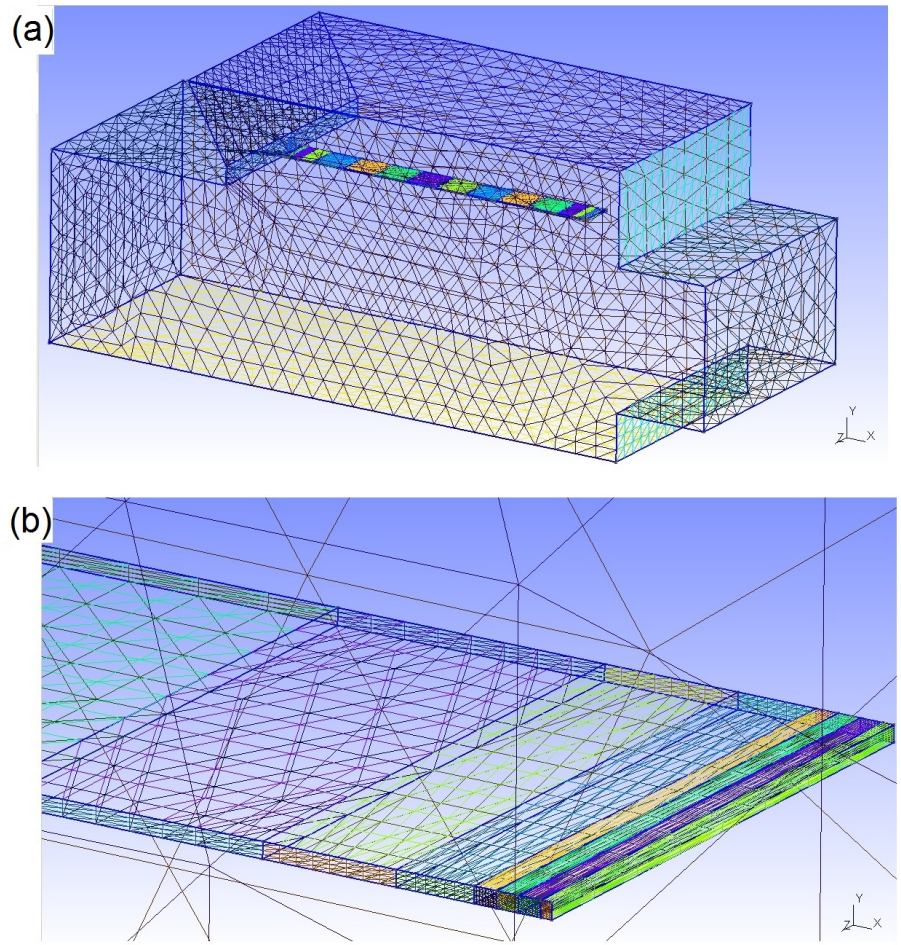

Figure A.1: *Image from Gmsh showing a typical surface mesh over the entire geometry of a fluid flow simulation (a) and zoomed into the cantilever free end (b).*

.

.

.

```
Field[1] = Box;

Field[1].VIn = 0.0000007;

Field[1].VOut = 0.000053;

Field[1].XMax = 0.00038;

Field[1].XMin = -5e-006;

Field[1].YMax = 5.80e-005;
```

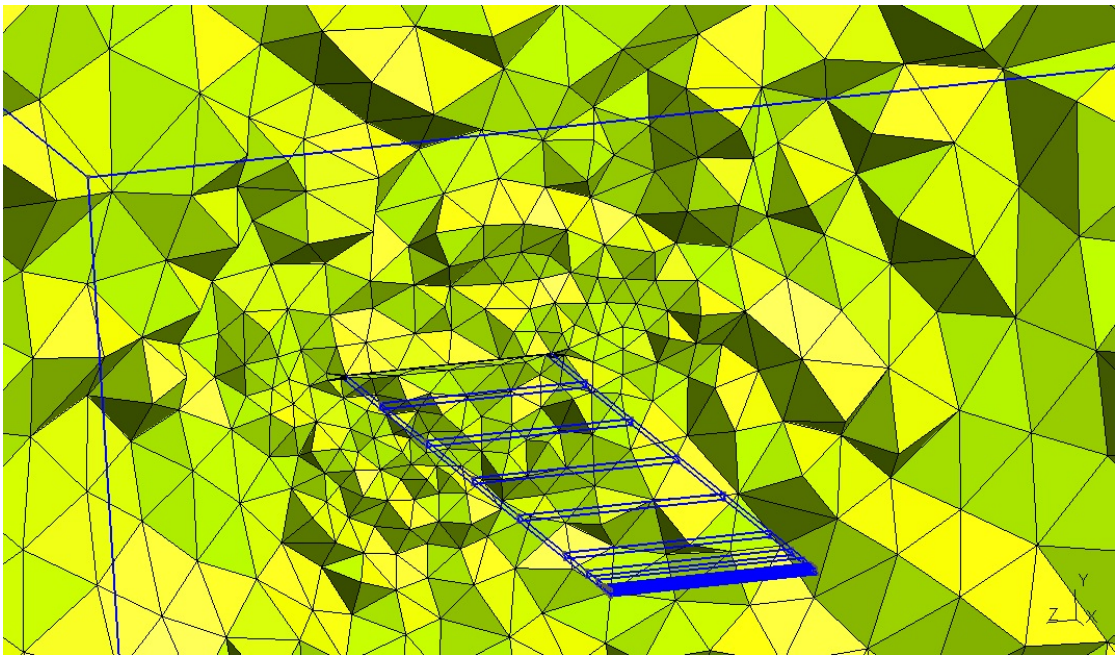

Figure A.2: *Image from Gmsh showing a slice through the 3-D mesh of figure A.1.*

```
Field[1].YMin = 4.30e-005;

Field[1].ZMax = 0.000147;

Field[1].ZMin = 0.000098;

Background Field = 1;
```

'cl' is a term describing the characteristic length and must match the quantity 'Field[1].VOut'. The characteristic length within the box is defined by 'Field[1].VIn'. The 'Field[1]' commands come at the end of the file. Comparison of figures A.2 and A.3 show the effect of using a box (with the commands above) to shorten the characteristic length of elements around the cantilever.

To obtain the variation of fluidic forces along the cantilever, it was divided into several sections, as can be seen in figure A.1. Elmer was used to calculate the force on each of the sections.

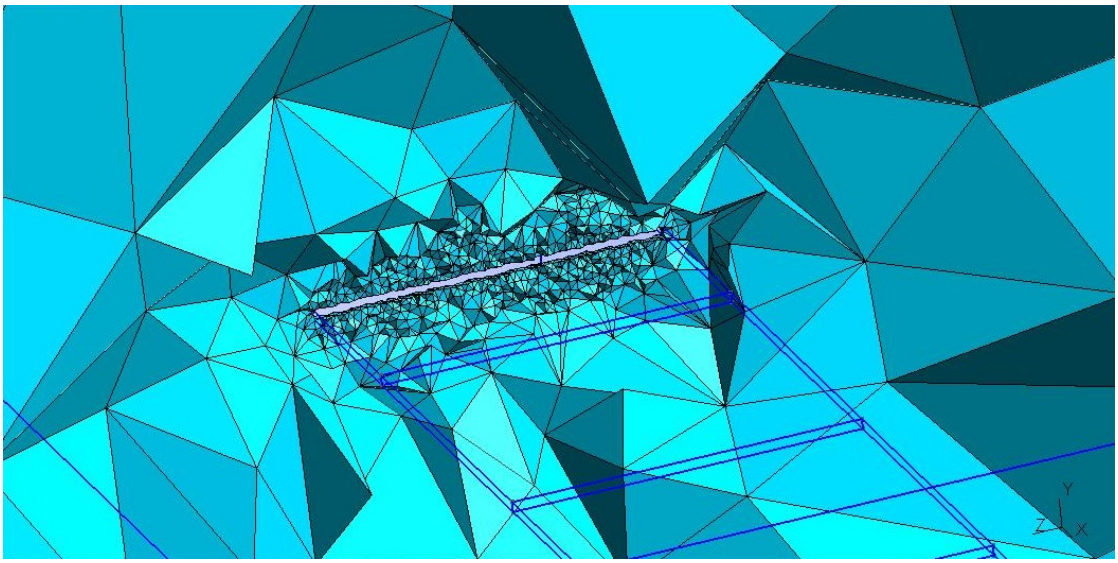

Figure A.3: *Image from Gmsh showing a 3-D mesh slice through one of the finer simulations, such as used in the production of data in figure 4.20. The 'box' field command has been used to refine the mesh in the vicinity of the cantilever.*

A.2 Elmer

The simulations themselves were executed using the multiphysics, open source FEA software package Elmer.[55] Version 7.0 in a variety of different revisions (rev.5790 to rev.5817) was used. The documentation for Elmer does not reflect the possibilities of the software, and is certainly not up to date. The following is a summary of some of the actions which can be made to achieve successful convergence of the simulations, followed by specifics relating to each type of simulation carried out and a brief description of test problems.

The meshes (saved in .msh format) produced by Gmsh were used in Elmer. Elmer uses the mesh file and a series of commands in the solver input file (.sif) to run the simulations. The sif file contains commands relating to each solver and each mesh along with materials properties and boundary conditions. In each solver section there are a variety of

parameters that can be altered to assist with convergence of the iterative process of the simulation:

- ***Nonlinear System Relaxation Factor*** **Set between zero and one. Lower values assist convergence of nonlinear problems but result in more iterations and therefore a longer simulation time to reach convergence. Higher values mean that the simulation requires fewer iterations, assuming it still converges. Providing convergence is achieved, the value of the nonlinear system relaxation factor ultimately has no bearing on the result.**

- ***Nonlinear System Newton After Iteration (or Tolerance)*** **The Newton solver is faster but less robust than the Picard iterations that the solver begins with. For all fluid flow simulations the Newton system was disabled by instructing it to run after a greater number of iterations than the maximum allowed and by setting the 'After Tolerance' field to zero.**

- ***Linear System Preconditioning*** **Set by replacing 'n' in 'ILUn' by a number. Higher 'n' give more advanced preconditioning and a greater likelihood of convergence, but exponentially increases the amount of memory required by the software. Typically n=2 was the highest available for fluid flow simulations, though up to n=5 was required and used to solve eigenvalue problems.**

- ***Linear System Preconditioning Recompute*** **Increased to a value of 15 (from the default of 1) for all simulations due to the small dimensions used in the simulations.**

- ***Linear System Convergence Tolerance*** **Decreased to by several orders of magnitude to around $\times 10^{-17}$ to assist with convergence, required due to the very small dimensions in the geometries used.**

Furthermore the linear and nonlinear maximum iterations may be increased to allow convergence to be reached as most of the above actions will tend to assist convergence but require more iterations. In the 'Simulation' section of the .sif file the 'Max Output Level' may be increased to 6 or 7 such that during the simulation the solver log prints more information, which can assist with diagnosis of problems.

A.2.1 Fluid Flow

Simulations relating to both the parallel flow of chapter 4 and perpendicular flow of chapter 5 have been executed. Most of the tricks described above were required to obtain reliable convergence for realistic fluid flow speeds. A short section of the microchannel was typically included in the geometry/mesh as it appeared to assist with convergence. The boundary condition at the start of the (simulated) channel inlet (at large x in figureA.1(a)) was subject to a 1-D flow in the x-direction with a Poiseuille profile given by the following excerpt from a sif file:

```
Boundary Condition 100
  Target Boundaries(1) = 100
  Name = "inlet"
  Velocity 3 = 0
  Velocity 1 = Variable Coordinate 2; Real MATC "2600000000*(tx-
  0.00005)*(tx+0.0001)"
  Velocity 2 = 0
```

```
End
```

where +0.00005 and -0.0001 are the y-coordinates of the top and bottom surfaces of the microchannel in this particular example. The sides of the simulated geometry, at large and small z in figure A.1(a), are halfway between the cantilever of interest and where the neighbouring cantilever would be on a real chip. These surfaces are subject to a no flux boundary condition: the velocity parallel to the boundary is unrestricted but the perpendicular velocity is zero. Simulations were conducted to prove the validity of this boundary condition.

The forces on a desired boundary are calculated and saved by adding two further solvers to the .sif file:

```
Solver 2
 Exec Solver = After All
 Equation = Fluidic Force
 Procedure = "FluidicForce" "ForceCompute"
 Calculate Viscous Force = True
End


Solver 3
 Exec Solver = After All
 Procedure = "SaveData" "SaveScalars"
 Filename = fluidicforceNWh150_75leveldx8d100v7.dat
 Save Variable 1 = FluidForce 1
End


Equation 1
```

```
  Name = "Equation 1"
  Active Solvers(3) = 1 2 3
End
```

along with adding a command relating to each boundary upon which the force should be calculated:

```
Boundary Condition 6
  Target Boundaries(1) = 6
  Name = "side wall fluid force"
  Velocity 3 = 0
  Velocity 1 = 0
  Velocity 2 = 0
 Calculate Fluidic Force = True
End
```

The forces are then output for each boundary in a text file, the name of which is given by the 'Filename' field.

One of the weaknesses of Elmer is in the simulation of the transition to turbulent flow, which was attempted largely unsuccessfully. For example OpenFOAM, another open source simulation program, would be expected to work better in such regimes.

A.2.2 Static Bending

To obtain realistic results when simulating static bending (or other structural mechanics) the mesh must be built using higher order elements. In Gmsh the following menus were accessed: Tools → Options → Mesh → General. The element order was then set at two. Essentially, higher or-

der elements are elements where there are additional nodes in the middle of the lines which connect the corners of the mesh tetrahedra.

A nominal force can be specified upon a boundary as a force per unit area. Forces from perpendicular fluid flow simulations can be transposed into a text file and are used to apply a force to the bottom boundary of the cantilever to bend it flexurally using the following commands for the boundary condition:

```
Boundary Condition 3
  Target Boundaries(1) = 7
  Name = "Force on bottom surface"
    Force 2 = Variable Coordinate 1
      Real
        include Fv10.txt
      End
End
```

The file 'Fv10.txt' contains 2000 rows and two columns. One column consists of the position along the x-direction of the cantilever, the second the force per unit area at that x value. The distance between x values should be less than the distance between nodes of the mesh on the cantilever surface.

A.2.3 Eigenmodes

As with the bending simulations, higher order elements were used in the meshes of the cantilever for eigenmode simulations. Note that the displacements of each of the modes are saved as different timesteps in the .ep file and the eigenfrequencies (in the form ω^2) are printed at the tail of

the solver log. It is relatively easy to couple a bending simulation with a calculation of the eigenmodes as the same mesh, that of the structure of interest, is used for both solvers. Eigenmode analysis was added to static bending simulations in section 5.5, for example for the calculation of the data in figure 5.8.

A.2.4 Coupling of Solvers

As mentioned above, different solvers can be coupled satisfactorily in Elmer if both solvers use the same mesh. However, if one wishes to simulate a fluid structure interaction problem, where a flow of fluid bends a structure (e.g. the cantilever) and then responds to the movement, then the Elmer/Gmsh setup encounters difficulties. The reason is that both the cantilever and fluid must be meshed separately but their meshes must match one another at the surface of the cantilever. This is possible, though problematical, with Gmsh. The stiffness of the cantilever determines how much it moves, but when it does, Elmer has to move the mesh of both the fluid and the structure. At this point non-physical results were observed with uncontrollable displacements and oscillations.

Alternative (commercial) packages such as Comsol Multiphysics should be able to deal with this sort of coupling in a more satisfactory manner.

A.3 Test Problems of Elmer

Each version of Elmer is tested on a range of around 30 simple utility examples to ensure agreement with previous versions and other programs. Furthermore the problem of Stokes flow around a sphere was executed in 3-D and for a variety of speeds. The forces on the sphere predicted by

Elmer agreed with those obtained from Stokes law to within ≈5% thus giving confidence to the simulated fluidic forces applied to the microcantilevers by the flow.

B Publications, Presentations, and this Thesis

B.1 Publication List

1. **J.D. Parkin and G. Hähner. Mass determination and sensitivity based on resonance frequency changes of the higher flexural modes of microcantilever sensors. *Review of Scientific Instruments*, 82:035108, 2011.**

2. **J.D. Parkin and G. Hähner. Determination of the spring constants of the higher flexural modes of microcantilever sensors. *Nanotechnology*, 24:065704, 2013.**

3. **J.D. Parkin and G. Hähner. Patent application GB1216529.6.**

B.2 Conferences

1. **July 2010, UK SPM meeting. Co-author of poster (presented by G. Hähner) entitled *Experimental Determination of the Dynamic Spring Constants of the Flexural Modes of Microcantilever Sensors.***

2. **July 2011, Asylum AFM forum. Talk entitled *Determination of the Spring Constants of the Higher Flexural and Torsional Modes of Microcantilever Sensors.***

3. **July 2011, UK SPM meeting. Poster entitled *Determination of the Spring Constants of the Higher Flexural and Torsional Modes of Microcantilever Sensors.* Recipient of prize for 2^{nd} best poster.**

4. **September 2012, European Microscopy Congress. Poster entitled**

Microcantilevers as ultrasensitive probes of mass and intermolecular interactions.

5. **October/November 2012, American Vacuum Society Annual Symposium. Presentation entitled *Experimental calibration of the higher flexural modes of microcantilever sensors.***

B.3 The Production of this Thesis

This thesis was written using various packages of open source software for which the author is grateful. It was written in LaTeXusing the TeXnicCentre[144] text editor (V1.0) and compiled with MiKTeX[145] V2.8. Referencing and bibliography management was via JabRef[146] V2.9.

References

[1] **S. Timoshenko, D.H. Young, and W. Weaver Jr. *Vibration Problems in Engineering*. John Wiley, New York, 4th edition, 1974.**

[2] **F.J. Giessibl. Advances in atomic force microscopy. *Reviews of Modern Physics*, 75:949–983, 2003.**

[3] **Y. Seo and W. Jhe. Atomic force microscopy and spectroscopy. *Reports on Progress in Physics*, 71:016101, 2008.**

[4] **G. Binnig, C. Gerber, E. Stoll, T.R. Albrecht, and C.F. Quate. Atomic resolution with atomic force microscope. *Europhysics Letters*, 3:1281–1286, 1987.**

[5] **J.A. Kubby and J.J. Boland. Scanning tunneling microscopy of semiconductor surfaces. *Surface Science Reports*, 26:61–204, 1996.**

[6] **M. Janko, A. Zink, A. M. Gigle, W.M. Heckl, and R.W. Stark. Nanostructure and mechanics of mummified type 1 collagen from the 5300-year-old Tyrolean Iceman. *Proceedings of the Royal Society B - Biological Sciences*, 277:2301–2309, 2010.**

[7] **G. Binnig, C.F. Quate, and C. Gerber. Atomic force microscope. *Physical Review Letters*, 56:930–933, 1986.**

[8] **R. Garcia and E.T. Herruzo. The emergence of multifrequency force microscopy. *Nature Nanotechnology*, 7:217–226, 2012.**

[9] **S.J. Organ, J.K. Hobbs, and M.J. Miles. Reorganization and melt of polyethylene single crystals: complementary TEM, DSC, and real-time AFM studies. *Macromolecules*, 37:4562–4572, 2004.**

[10] **H.J. Butt, B. Cappella, and M. Kappl. Force measurements with the atomic force microscope: Technique, interpretation and applications. *Surface Science Reports*, 59:1–152, 2005.**

[11] **J.K. Hobbs, N. Mullin, C.H.M. Weber, O.E. Farrance, and C. Vasilev. "Watching" processes in soft matter with SPM. *Materials Today*, 7:26–33, 2009.**

[12] **F. Braet and E. Wisse. AFM imaging of fenestrated liver sinusoidal endothelial cells. *Micron*, 43:1252–1258, 2012.**

[13] **B. Drake, C.B. Prater, A.L. Weisenhorn, S.A.C. Gould, T.R. Albrecht, C.F. Quate, D.S. Cannell, H.G. Hansma, and P.K. Hansma. Imaging crystals, polymers, and processes in water with the atomic force microscope. *Science*, 243:1586–1589, 1989.**

[14] **J.K. Hobbs, O.E. Farrance, and L. Kailas. How atomic force microscopy has contributed to our understanding of polymer crystallisation. *Polymer*, 50:4281–4292, 2009.**

[15] **A.D.L. Humphris, M.J. Miles, and J.K. Hobbs. A mechanical microscope: High-speed atomic force microscopy. *Applied Physics Letters*, 86:034106, 2005.**

[16] L.M. Picco, L. Bozec, A. Ulcinas, D.J. Engledew, M. Antognozzi, M.A. Horton, and M.J. Miles. Breaking the speed limit with atomic force microscopy. *Nanotechnology*, 18:044030, 2007.

[17] J.P. Howard-Knight and J.K. Hobbs. Video rate atomic force microscopy using low stiffness, low resonant frequency cantilevers. *Applied Physics Letters*, 93:104101, 2008.

[18] S.E. Cross, Y.-S. Jin, J. Rao, and J.K. Gimzewski. Nanomechanical analysis of cells from cancer patients. *Nature Nanotechnology*, 2:780–783, 2007.

[19] N. Mullin and J.K. Hobbs. Torsional resonance atomic force microscopy in water. *Applied Physics Letters*, 92:053103, 2008.

[20] N. Mullin, C. Vasilev, J.D. Tucker, C.N. Hunter, C.H.M. Weber, and J.K. Hobbs. "Torsional tapping" atomic force micriscopy using T-shaped cantilevers. *Applied Physics Letters*, 94:173109, 2009.

[21] J.D. Parkin and G. Hähner. Mass determination and sensitivity based on resonance frequency changes of the higher flexural modes of cantilever sensors. *Review of Scientific Instruments*, 82:035108, 2011.

[22] Y. Sugimoto, S. Innami, M. Abe, O. Custance, and S. Morita. Dynamic force spectroscopy using cantilever higher flexural modes. *Applied Physics Letters*, 91:093120, 2007.

[23] S. Kawai, S. Kitamura, D. Kobayashi, S. Meguro, and H. Kawakatsu. An ultrasmall amplitude operation of dynamic force microscopy with second flexural mode. *Applied Physics Letters*, 86:193107, 2005.

[24] S. Kawai and H. Kawakatsu. Atomically resolved dynamic force microscopy operating at 4.7 MHz. *Applied Physics Letters*, 88:133103, 2006.

[25] Y. Naitoh, Z.M. Ma, Y.J. Li, M. Kageshima, and Y. Sugawara. Simultaneous observation of surface topography and elasticity at atomic scale by multifrequency frequency modulation atomic force Microscopy. *Journal of Vacuum Science & Technology B*, 28:1210–1214, 2010.

[26] R. Garcia and R. Perez. Dynamic atomic force microscopy methods. *Surface Science Reports*, 47:197–301, 2002.

[27] W.A. Ducker, T.J. Senden, and R.M. Pashley. Direct measurements of colloidal forces using an atomic force microscope. *Nature*, 353:239–241, 1991.

[28] H.J. Butt. Measuring electrostatic, van der Waals, and Hydration forces in electrolyte solutions with an atomic force microscope. *Biophysical Journal*, 60:1438–1444, 1991.

[29] N.H. Thomson, M. Fritz, M. Radmacher, J.P. Cleveland, C.F. Schmidt, and P.K. Hansma. Protein tracking and detection of protein motion using atomic force microscopy. *Biophysical Journal*, 70:2421–2431, 1996.

[30] S.E. Cross, Y.-S. Jin, J. Tondre, R. Wong, J.Y. Rao, and J.K. Gimzewski. AFM-Based analysis of human metastatic cancer cells. *Nanotechnology*, 19:384003, 2008.

[31] M. Radmacher, M. Fritz, C.M. Kacher, J.P. Cleveland, and P.K. Hansma. Measuring the viscoelastic properties of human platelets with the atomic force microscope. *Biophysical Journal*, 70:556–567, 1996.

[32] R.E. Mahaffy, S. Park, E. Gerde, J. Käs, and C.K. Shih. Quantitative analysis of the viscoelastic properties of thin regions of fibroblasts using atomic force microscopy. *Biophysical Journal*, 86:1777–1793, 2004.

[33] A. Boisen, S. Dohn, S.S. Keller, S. Schmid, and M. Tenje. Cantilever-like micromechanical sensors. *Reports on Progress in Physics*, 74:036101, 2011.

[34] L.A. Pinnaduwage, D.L. Hedden, A. Gehl, V.I. Boiadijev, J.E. Hawk, R.H. Farahi, T. Thundat, E.J. Houser, S. Stepnowski, R.A. McGill, L. Deel, and R.T. Lareau. A sensitive, handheld vapor sensor based on microcantilevers. *Review of Scientific Instruments*, 75:4554–4557, 2004.

[35] K. Kang, A. Sachan, M. Nilsen-Hamilton, and P. Shrotriya. Aptamer Functionalized Microcantilever Sensors for Cocaine Detection. *Langmuir*, 27:14696–14702, 2011.

[36] K.E. Petersen and C.R. Guarnieri. Young's modulus measurements of thin-films using micromechanics. *Journal of Applied Physics*, 50:6761–6766, 1979.

[37] L. Qiao and X.J. Zheng. Effect of surface stress on the stiffness of micro/nanocantilevers: nanowire elastic modulus measured by nano-scale tensile and vibrational techniques. *Journal of Applied Physics*, 113:013508, 2013.

[38] M.K. Baller, H.P. Lang, J. Fritz, Ch. Gerber, J.K. Gimzewski, U. Drechsler, H. Rothuizen, M. Despont, P. Vettiger, F.M. Battiston, J.P. Ramseyer, P. Fornaro, E. Meyer, and H.-J. Güntherodt. A cantilever array-based artificial nose. *Ultramicroscopy*, 82:1–9, 2000.

[39] B.N. Johnson and R. Mutharasan. Biosensing using dynamic-mode cantilever sensors: A review. *Biosensors and Bioelectronics*, 32:1–18, 2012.

[40] N. McLoughlin, S.L. Lee, and G. Hähner. Simultaneous determination of density and viscosity of liquids based on resonance curves of uncalibrated microcantilevers. *Applied Physics Letters*, 89:184106, 2006.

[41] N. McLoughlin, S.L. Lee, and G. Hähner. Temperature dependence of viscosity and density of viscous liquids determined from thermal noise spectra of uncalibrated atomic force microscope cantilevers. *Lab on a Chip*, 7:1057–1061, 2007.

[42] M. Hennemeyer, S. Burghardt, and R.W. Stark. Cantilever micro-rheometer for the characterisation of sugar solutions. *Sensors*, 8:10–22, 2008.

[43] G.V. Lubarsky and G. Hähner. Calibration of the normal spring constant of microcantilevers in a parallel fluid flow. *Review of Scientific Instruments*, 78:095102, 2007.

[44] G. Hähner. Dynamic spring constants for higher flexural modes of cantilever plates with applications to atomic force microscopy. *Ultramicroscopy*, 110:801, 2010.

[45] K. Lakshmoji, K. Prabakar, A. Kumar, J. Brijitta, J. Jayapandian, B.V.R. Tata, A.K. Tyagi, and C.S. Sundar. Microcantilever-based mass sensors: working at higher modes against reducing the dimensions. *Micro and Nano Letters*, 7:613–616, 2012.

[46] G.M. Whitesides. The origins and the future of microfluidics. *Nature*, 442:368–373, 2006.

[47] http://www.spmtips.com/afm-tip-hq-csc38-tipless-al-bs, December 2012.

[48] C.A. Clifford and M.P. Seah. The determination of atomic force microscope cantilever spring constants via dimensional methods for nanomechanical analysis. *Nanotechnology*, 16:1666–1680, 2005.

[49] J.R. Lozano, D. Kiracofe, J. Melcher, R. Garcia, and A. Raman. Calibration of higer eigenmode spring constants of atomic force microscope cantilevers. *Nanotechnology*, 21:465502, 2010.

[50] M.L.B. Palacio and B. Bhushan. Normal and lateral force calibration techniques for AFM cantilevers. *Critical Reviews in Solid State and Materials Sciences*, 35:73–104, 2010.

[51] M. Munz. Force calibration in lateral force microscopy: a review of the experimental methods. *Journal of Physics D: Applied Physics*, 43:063001, 2010.

[52] S.T. Thornton and J.B. Marion. *Classical Dynamics of Particles and Systems*. Cengage Learing, 5th edition, 2003.

[53] J.E. Sader, I. Larson, P. Mulvaney, and L.R. White. Method for the calibration of atomic force microscope cantilevers. *Review of Scientific Instruments*, 66:3789–3798, 1995.

[54] G. Hähner. Normal spring constants of cantilever plates for different load distributions and static deflection with applications to atomic force microscopy. *Journal of Applied Physics*, 104:084902, 2008.

[55] Elmer. http://www.csc.fi/english/pages/elmer, January 2013.

[56] C. Geuzaine and J.-F. Remacle. Gmsh: a three-dimensional finite element mesh generator with built-in pre- and post-processing facilities. *International Journal for Numerical Methods in Engineering*, 79:1309–1331, 2009.

[57] J. Tamayo, V. Pini, P. Kosaka, N.F. Martinez, O. Ahumada, and M. Calleja. Imaging the surface stress and vibration modes of a microcantilever by laser beam deflection microcscopy. *Nanotechnology*, 23:315501, 2012.

[58] C.P. Green and J.E. Sader. Torsional frequency response of cantilever beams immersed in viscous fluids with applications to the atomic force microscope. *Journal of Applied Physics*, 92:6262–6274, 2002.

[59] D.R. Lide, editor. *CRC Handbook of Chemistry and Physics*, volume 86. CRC press, Boca Raton, 2003.

[60] R. Courant and D. Hilbert. *Methodender Mathematischen Physik I.* Springer-Verlag, Heidelberg, 1968.

[61] J.L. Hazel and V.V. Tsukruk. Spring constants of composite ceramic/gold cantilevers for scanning probe microscopy. *Thin Solid Films*, 339:249–257, 1999.

[62] L.D. Landau and E.M. Lifshitz. *Theory of Elasticity (Course of Theoretical Physics, Volume 7).* Elsevier, 3rd edition, 1986.

[63] P.S. Waggoner and H.G. Craighead. Micro- and nanomechanical sensors for environmental, chemical, and biological detection. *Lab on a Chip*, 7:1238–1255, 2007.

[64] M. Spletzer, A. Raman, and R. Reifenberger. Elastometric sensing using higher flexural eigenmodes of microcantilevers. *Applied Physics Letters*, 91:184103, 2007.

[65] Y.T. Yang, C. Callegari, X.L. Feng, K.L. Ekinci, and M.L. Roukes. Zeptogram-scale nanomechanical mass sensing. *Nano Letters*, 6:583–586, 2006.

[66] M. Li, H.X. Tang, and M.L. Roukes. Ultra-sensitive NEMS-based cantilevers for sensing, scanned probe and very high-frequency applications. *Nature Nanotechnology*, 2:114–120, 2007.

[67] B. Ilic, S. Krylov, M. Kondratovic, and H.G. Craighead. Selective vibrational detachment of microspheres using optically excited in-plane motion of nanomechanical beams. *Nano Letters*, 7:2171–2177, 2007.

[68] D. Ramos, M. Calleja, J. Mertens, A. Zaballos, and J. Tamayo. Measurement of the mass and rigidity of adsorbates on a microcantilever sensor. *Sensors*, 7:1834–1845, 2007.

[69] A.K. Naik, M.S. Hanay, W.K. Hiebert, X.L. Feng, and M.L. Roukes. Towards single-molecule nanomechanical mass spectrometry. *Nature Nanotechnology*, 4:445–450, 2009.

[70] S. Dohn, R. Sandberg, W. Svendsen, and A. Boisen. Enhanced functionality of cantilever based mass sensors using higher modes. *Applied Physics Letters*, 86:233501, 2005.

[71] S. Dohn, S. Schmid, F. Amiot, and A. Boisen. Position and mass determination of multiple particles using cantilever based mass sensors. *Applied Physics Letters*, 97:044103, 2010.

[72] E.A. Wachter and T. Thundat. Micromechanical sensors for chemical and physical measurements. *Review of Scientific Instruments*, 66:3662–3667, 1995.

[73] I.U. Vakarelski, S.A. Edwards, R.R. Dagastine, D.Y.C. Chan, G.W. Stevens, and F. Grieser. Atomic force microscopy: Loading position dependence of cantilever spring constants and detector sensitivity. *Review of Scientific Instruments*, 78:116102, 2007.

[74] U. Srinivasan, M.R. Houston, R.T. Howe, and R. Maboudian. Alkytrichlorosilane-based self-assembled monolayer films for stiction reduction in silicon micromachines. *Journal of Microelectromechanical Systems*, 7:252–260, 1998.

[75] R. Maboudian, W.R. Ashurst, and C. Carraro. Self-assembled monolayers as anti-stiction coatings for MEMS: characteristics and recent developments. *Sensors and Actuators*, 82:219–223, 2000.

[76] http://www.brukerafmprobes.com/Product.aspx?ProductID=3693, January 2013.

[77] G.Y. Chen, T. Thundat, E.A. Wachter, and R.J. Warmack. Adsorption-induced surface stress and its effects on resonance frequency of microcantilevers. *Journal of Applied Physics*, 77:3618–3622, 1995.

[78] J.L. Hutter and J. Bechhoefer. Calibration of atomic-force microscope tips. *Review of Scientific Instruments*, 64:1868–1873, 1993.

[79] K.L. Ekinci, Y.T. Yang, and M.L. Roukes. Ultimate limits to inertial mass sensing based upon nanoelectromechanical systems. *Journal of Applied Physics*, 95:2682–2689, 2004.

[80] S. Dohn, W. Svendsen, A. Boisen, and O. Hansen. Mass and position determination of attached particles on cantilever based mass sensors. *Review of Scientific Instruments*, 78:103303, 2007.

[81] D.B. Asay and S.H. Kim. Evolution of the adsorbed water layer structure on silicon oxide at room temperature. *The Journal of Physical Chemistry B*, 109:16760–16763, 2005.

[82] D.B. Asay and S.H. Kim. Effects of adsorbed water layer structure on adhesion force of silicon oxide nanoasperity contact in humid ambient. *The Journal of Chemical Physics*, 124:174712, 2006.

[83] M. Wang, K.M. Liechti, Q. Wang, and J.M. White. Self-assembled silane monolayers: fabrication with nanoscale uniformity. *Langmuir*, 21:1848–1857, 2005.

[84] J.D. Parkin and G. Hähner. Determination of the spring constants of the higher flexural modes of microcantilever sensors. *Nanotechnology*, 24:065704, 2013.

[85] J.E. Sader, J.W.M. Chon, and P. Mulvaney. Calibration of rectangular atomic force microscope cantilevers. *Review of Scientific Instruments*, 70:3967–3969, 1999.

[86] G.V. Lubarsky and G. Hähner. Hydrodynamic methods for calibrating the normal spring constant of microcantilevers. *Nanotechnology*, 19:325707, 2008.

[87] O.D. Payton, L. Picco, M.J. Miles, M.E. Horner, and A.R. Champneys. Improving the signal-to-noise ratio of high-speed contact mode atomic force micriscopy. *Review of Scientific Instruments*, 83:083710, 2012.

[88] T. Mühl, J. Körner, S. Philippi, C. F. Reich, A. Leohardt, and B. Büchner. Magnetic force microscopy sensors providing in-plane and perpendicular sensitivity. *Applied Physics Letters*, 101:112401, 2012.

[89] D. Kiracofe and A. Raman. On eigenmodes, stiffness, and sensitivity of atomic force microscope cantilevers in air versus liquids. *Journal of Applied Physics*, 107:033506, 2010.

[90] T.J. Senden and W.A. Ducker. Experimental determination of spring constants in atomic force microscopy. *Langmuir*, 10:1003–1004, 1994.

[91] C.T. Gibson, G.S. Watson, and S. Myhra. Determination of the spring constants of probes for force microscopy/spectroscopy. *Nanotechnology*, 7:259–262, 1996.

[92] J.D. Holbery, V.L. Eden, M. Sarikaya, and R.M. Fisher. Experimental determination of scanning probe microscope cantilever spring constants utilizing a nanoindentation apparatus. *Review of Scientific Instruments*, 71:3769–3776, 2000.

[93] J.M. Neumeister and W.A. Ducker. Lateral, normal, and longitudinal spring constants of atomic force microscopes. *Review of Scientific Instruments*, 65:2527–2531, 1994.

[94] H.J. Butt and M. Jaschke. Calculation of thermal noise in atomic force microscopy. *Nanotechnology*, 6:1–7, 1995.

[95] R.W. Stark, T. Drobek, and W.M. Heckl. Thermomechanical noise of a free V-shaped cantilever for atomic-force microscopy. *Ultramicroscopy*, 86:207–215, 2001.

[96] M. Boudaoud, Y. Haddab, Y. Le Gorrec, and P. Lutz. Study of thermal and acoustic noise interferences in low stiffness atomic force microscope cantilevers and characterization of their dynamic properties. *Review of Scientific Instruments*, 83:013704, 2012.

[97] R.S. Gates and J.R. Pratt. Accurate and precise calibration of AFM cantilever spring constants using laser Doppler vibrometry. *Nanotechnology*, 23:375702, 2012.

[98] J.P. Cleveland, S. Manne, D. Bocek, and P.K. Hansma. A nondestructive method for determining the spring constant of cantilevers for scanning force microscopy. *Review of Scientific Instruments*, 64:403–405, 1993.

[99] A.D. Slattery, J.S. Quinton, and C.T. Gibson. Atomic force microscope cantilever calibration using a focussed ion beam. *Nanotechnology*, 23:285705, 2012.

[100] C.T. Gibson, B.L. Weeks, J.R.I. Lee, C. Abell, and T. Rayment. A nondestructive technique for determining the spring constant of atomic force microscope cantilevers. *Review of Scientific Instruments*, 72:2340, 2001.

[101] J.E. Sader, J.A. Sanelli, B.D. Adamson, J.P. Monty, X. Wei, S.A. Crawford, J.R. Friend, I. Marusic, P. Mulvaney, and E.J. Bieske. Spring constant calibration of atomic force microscope cantilevers of arbitrary shape. *Review of Scientific Instruments*, 83:103705, 2012.

[102] J.E. Sader, J. Sanelli, B.D. Hughes, J.P. Monty, and E.J. Bieske. Distortion in the thermal noise spectrum and quality factor of nanomechanical devices due to finite frequency resolution with applications to the atomic force microscope. *Review of Scientific Instruments*, 82:095104, 2011.

[103] M.-S. Kim, J.-H. Choi, J.-H. Kim, and Y.-K. Park. Accurate determination of spring constant of atomic force microscope cantilevers and comparison with other methods. *Measurement*, 43:520–526, 2010.

[104] J. te Riet, A.J. Katan, C. Rankl, S.W. Stahl, A.M. van Buul, I.Y. Phang, A. Gomez-Casado, P. Schön, J.W. Gerritsen, A. Cambi, A.E. Rowan, G.J. Vancso, P. Jonkheijm, J. Huskens, T.H. Oosterkamp, H. Gaub, P. Hinterdorfer, C.G. Figdor, and S. Speller. Interlaboratory round robin on cantilever calibration for AFM force spectroscopy. *Ultramicroscopy*, 111:1659–1669, 2011.

[105] L.D. Landau and E.M. Lifshitz. *Fluid Mechanics (Course of Theoretical Physics, Volume 6)*. Elsevier, 1986.

[106] R.W. Johnson, editor. *The Handbook of Fluid Dynamics*. CRC Press and Springer-Verlag, 1998.

[107] C. Rands, B.W. Webb, and D. Maynes. Characterisation of transition to turbulence in microchannels. *International Journal of Heat and Mass Transfer*, 49:2924–2930, 2006.

[108] M. Böhle, D. Etling, U. Müller, K.R.S. Sreenivasan, U. Riedel, and J. Warnatz. *Prandtl's Essentials of Fluid Mechanics*. Springer-Verlag, 2nd edition, 2004.

[109] F.M. White. *Fluid Mechanics*. WCB McGraw-Hill, 4th edition, 1999.

[110] G. Hestroni, A. Mosyak, E. Pogrebnyak, and L.P. Yarin. Fluid flow in microchannels. *International Journal of Heat and Mass Transfer*, 48:1982–1998, 2005.

[111] Online spring constant calibrator J.E. Sader. http://www.ampc.ms.unimelb.edu.au/afm/calibration.html, January 2013.

[112] J.E. Sader. Frequency response of cantilever beams immersed in viscous fluids with applications to the atomic force microscope. *Journal of Applied Physics*, 84:64–76, 1998.

[113] J.W.M. Chon, P. Mulvaney, and J.E. Sader. Experimental validation of theoretical models for the frequency response of atomic force microscope cantilever beams immersed in fluids. *Journal of Applied Physics*, 87:3978–3988, 2000.

[114] C. Rawlings and C. Durkan. Calibration of the spring constant of cantilevers of arbitrary shape using the phase signal in an atomic force microscope. *Nanotechnology*, 23:485708, 2012.

[115] L. Meagher, G. Maurdev, and M.L. Gee. Interaction forces between a bare silica surface and an alpha-alumina surface bearing adsorbed polyelectrolyte and surfactant. *Langmuir*, 18:26492657, 2002.

[116] T.S. Balint and A.D. Lucey. Instability of a cantilevered flexible plate in viscous channel flow. *Journal of Fluids and Structures*, 20:893–912, 2005.

[117] R.M. Howell, A.D. Lucey, P.W. Carpenter, and M.W. Pitman. Interaction between a cantilevered-free flexible plate and ideal flow. *Journal of Fluids and Structures*, 25:544–566, 2009.

[118] J. D. Parkin and G. Hähner. A method to determine the torsional stiffness of cantilevered structures, patent pending, No. GB1216529.6.

[119] V.V. Tsukruk and V.N. Bliznyuk. Adhesive and friction forces between chemically modified silicon and silicon nitride surfaces. *Langmuir*, 14:446–455, 1998.

[120] R.J. Cannara, M. Eglin, and R.W. Carpick. Lateral force calibration in atomic force microscopy: a new lateral force calibration method and general guidelines for optimization. *Review of Scientific Instruments*, 77:053701, 2006.

[121] D. Choi, W. Hwang, and E. Yoon. Improved lateral force calibration based on the angle conversion factor in atomic force microscopy. *Journal of Microscopy - Oxford*, 228:190–199, 2007.

[122] D.F. Ogletree, R.W. Carpick, and M. Salmeron. Calibration of frictional forces in atomic force microscopy. *Review of Scientific Instruments*, 67:3298–3306, 1996.

[123] M. Varenberg, I. Etsion, and G. Halperin. An improved wedge calibration method for lateral force in atomic force microscopy. *Review of Scientific Instruments*, 74:3362–3367, 2003.

[124] X. Ling, H.J. Butt, and M. Kappl. Quantitative measurement of friction between single microspheres by friction force microscopy. *Langmuir*, 23:8392–8399, 2007.

[125] D.B. Asay and S.H. Kim. Direct force balance method for atomic force microscopy lateral force calibration. *Review of Scientific Instruments*, 77:043903, 2006.

[126] S. Ecke, R. Raiteri, E. Bonaccurso, C. Reiner, H.J. Deiseroth, and H.J. Butt. Measuring normal and friction forces acting on individual fine particles. *Review of Scientific Instruments*, 72:4164–4170, 2001.

[127] M.G. Reitsma. Lateral force microscope calibration using a modified atomic force microscope cantilever. *Review of Scientific Instruments*, 78:106102, 2007.

[128] M.G. Reitsma, R.S. Gates, L.H. Friedman, and R.F. Cook. Prototype cantilevers for quantitative lateral force microscopy. *Review of Scientific Instruments*, 82:093706, 2011.

[129] R.G. Cain, M.G. Reitsma, S. Biggs, and N.W. Page. Quantitative comparison of three calibration techniques for the lateral force microscope. *Review of Scientific Instruments*, 72:3304–3312, 2001.

[130] E. Liu, B. Blanpain, and J.P. Celis. Calibration procedures for frictional measurements with a lateral force microscope. *Wear*, 192:141–150, 1996.

[131] E. Tocha, J. Song, H. Schönherr, and G.J. Vancso. Calibration of friction force signals in atomic force microscopy in liquid media. *Langmuir*, 23:7078–7082, 2007.

[132] A. Feiler, P. Attard, and I. Larson. Calibration of the torsional spring constant and the lateral photodiode response of frictional force microscopes. *Review of Scientific Instruments*, 71:2746–2750, 2000.

[133] G. Bogdanovic, A. Meurk, and M.W. Rutland. Tip friction - torsional spring constant determination. *Colloids and Surfaces B - Biointerfaces*, 19:397–405, 2000.

[134] H. Xie, J. Vitard, S. Haliyo, and S. Regnier. Calibration of lateral force measurements in atomic force microscopy with a piezoresistive force sensor. *Review of Scientific Instruments*, 79:033708, 2008.

[135] C.P. Green, H. Lioe, J.P. Cleveland, R. Proksch, P. Mulvaney, and J.E. Sader. Normal and torsional spring constants of atomic force microscope cantilevers. *Review of Scientific Instruments*, 75:1988–1996, 2004.

[136] J.L. Hazel and V.V. Tsukruk. Friction force microscopy measurements: Normal and torsional spring constants for V-shaped cantilevers. *Journal of Tribology - Transactions of the ASME*, 120:814–819, 1998.

[137] H.D. Young, R.A. Freedman, and A.L. Ford. *University Physics with Modern Physics*. Addison Wesley, 11^{th} edition, 2004.

[138] http://www.appnano.com/products/silicon/fcl/fcl, January 2013.

[139] Y.C. Fung. *Foundations of solid mechanics*. Prentice-Hall Inc., 1965.

[140] http://www.uk.comsol.com/, January 2013.

[141] J. Lagowski, H.C. Gatos, and E.S. Sproles Jr. Surface stress and the normal mode of vibration of thin crystals: GaAs. *Applied Physics Letters*, 26:493–495, 1975.

[142] M.E. Gurtin, X. Markenscoff, and R.N. Thurston. Effect of surface stress on the natural frequency of thin crystals. *Applied Physics Letters*, 29:529–530, 1976.

[143] **R.E. Miller and V.B. Shenoy. Size-dependent elastic properties of nanosized structural elements. *Nanotechnology*, 11:139–147, 2000.**

[144] **http://www.texniccenter.org/, January 2013.**

[145] **http://miktex.org/, January 2013.**

[146] **JabRef Development Team. http://jabref.sf.net, January 2013.**